ENERGIZATION AND TRANSPORT OF IONS OF IONOSPHERIC ORIGIN IN THE TERRESTRIAL MAGNETOSPHERE

NASA Goddard Space Flight Center

Contract No. NAG5-1554

SwRI Project No. 15-4258

Final Report

30 April 1995

Prepared by

J.H. Waite, Jr.

Final report for NASA grant NAG5-1554

This serves as a final report for grant NAG5-1554 entitled Energization and Transport of Ions of Ionospheric Origin in the Terrestrial Magnetosphere. The work has been predominantly focused on ion outflows identified in two data sets: 1) Prognoz 7 and 2) Dynamics Explorer.

The Prognoz analysis has been carried out in conjunction with Dr. Oleg Vaisberg of IKI. The study analyzed ion densities, temperatures, and flow velocities in the magnetotail. The work performed under this contract consisted of developing a program to load the raw data, compute the background subtraction of a strong sun pulse, and use the net counts to calculate the low order moments of the distribution function. The study confirms the results of ISEE that the the cusp is a major source of plasmasheet plasma and goes beyond this to discuss the use of ion velocities as a way to examine the motions of the magnetotail. The initial work will be reported in Advances in Space research and is included in abstract form as Appendix A. In addition, Appendix A also contains a draft of a paper by Delcourt et al. which will be submitted to Geophysical Research Letters in June.

The work on the DE/Retarding Ion Mass Spectrometer data set represents the bulk of the effort. The work carried out under this grant is separated into two categories: 1) classification of low-energy ion flows from high-latitudes, and 2) studies of the polar wind. The work on classification of ion flows has consisted mainly of support work on studies that begin before my departure from NASA Marshall Space Flight Center. The major publications that have resulted from this work are: 1) the determination of plasma fluxes from the cleft ion fountain Pollack et al. [1990] and the recent thorough analysis and characterization of DE/RIMS high-latitude ion outflows by Giles et al. [1995]. These reprints are included as Appendix B of this report.

The polar wind is indeed a component of the low energy ion outflow at high latitude. However, the extensive theoretical work on this subject puts it in a category all to itself. The analysis of the polar wind by the RIMS group in the late 1980's culminated in the work of Chandler et al. [1991] (see Appendix C). This work reports the flux variability as a function of season, magnetic activity, etc. and was partially supported by this grant. In addition, much effort has been expended under this grant to complete a follow on study of the thermal structure of the polar wind. Extensive display tools and analysis software have been developed and used in an attempt to carry out this thermal analysis. However, the difficulties of performing multi-parameter, non-linear least squares fits has so far proved to be insurmountable. Therefore, the present work (see notes in Appendix C on work still in progress) uses a constrained fit scheme that combines the ion densities and flow velocities derived from Chandler et al. [1991] and a spacecraft potential derived from an empirical relation to the total ion density (utilizing the complete RIMS data set) to determine the remaining fit parameter, the ion temperature, via a least squares fit to the RIMS data. Reports of this work are anticipated in the near future.

References

Chandler, M.O., J.H. Waite, Jr., and T.E. Moore, Observation of Polar Ion Outflows, *J. Geophys. Res.*, **96**, (A2), 1421-1428, 1991.

Delcourt, D.C., J.A. Sauvaud, O.L. Vaisberg, L.A. Avanov, J.L. Burch, and J.H. Waite, Jr., Signatures of Impulsive Convection in the Magnetospheric Lobes, *Geophys. Res. Lett.*, June, 1995.

Giles, B.L., C.R. Chappell, T.E. Moore, R.H. Comfort, and J.H. Waite, Jr., Statistical survey of pitch angle distributions in core (0-50 eV) ions from Dynamics Explorer 1: Outflow in the auroral zone, polar cap, and cusp, *JGR*, **99**, A9, 17,483-17,501, 1994.

Pollack, C.J., M.O. Chandler, T.E. Moore, J.H. Waite, Jr., C.R. Chappell, and D.A. Gurnett, A Survey of Upwelling Ion Event Characteristics, *JGR*, **95**, A11, 18,969-18,980, 1990.

Vaisberg, O.L., L.A. Avanov, J.L. Burch, and J.H. Waite, Jr., "Measurements of Plasma in the Magnetospheric Tail Lobes, Abstract, 1995.

Appendix A

Vaisberg Abstract
Delcourt et al. reprint

MEASUREMENTS OF PLASMA IN THE MAGNETOSPHERIC TAIL LOBES

O.L. Vaisberg, and L.A. Avanov
Space Research Institute
84/32 Profsojuznaja St.
117810 Moscow GSP, Russia

J.L. Burch and J.H. Waite, Jr.
Southwest Research Institute
6220 Culebra Road
San Antonio, TX 78238-5166

ABSTRACT

The plasma spectrometer SKS on the Prognoz 8 satellite was able to measure the very dilute plasma in the tail lobe at distances 15-20 Earth radii about 50% of the time. The energy of the ions, being in the range of several hundred electron volts, decreases as the satellite moves from the high-latitude magnetopause to the plasma sheet. The velocity spread of the ions is narrow in the direction of motion, corresponding to a temperature of several eV. The temperature in the transverse direction is 2 to 3 times higher. Comparison with magnetospheric convection models suggests that these ions originate at low altitudes in the region near the cusp and are separated in the magnetospheric velocity spectrometer. Observed velocity variations along the spacecraft trajectory suggest the existence of a characteristic velocity profile and a characteristic temporal/spatial scale. Comparison of simultaneous E/q measurements with mass-selective detector measurements of protons and the alpha particles suggests that lobe plasma at these distances consists primarily of oxygen ions. The average ion flux density is about 3×10^5 cm^{-2} s^{-1}, giving estimated total flux over the lobe about 10^{25} s^{-1}, comparable to cusp/cleft source.

SIGNATURES OF IMPULSIVE CONVECTION IN THE MAGNETOSPHERIC LOBES

D. C. Delcourt[1], J. A. Sauvaud[2], O. L. Vaisberg[3], L. A. Avanov[3], J. L. Burch[4], and J. H. Waite, Jr.[4]

Abstract. We examine the injections of tailward flowing O^+ ions measured by the PROGNOZ-8 spacecraft in the magnetospheric lobes using three-dimensional single-particle codes. The repeated energy-time injection patterns observed are unexpectedly well correlated with *AE* variations during a time interval of about 7 hours. Such a correlation leads us to consider the effects of transient intensification of the large-scale magnetospheric plasma convection. Using a simple model of time-varying electric field, we show that the source of the ions lies near the dayside cusp. This source extends over a narrow (a few degrees) latitudinal interval in the vicinity of the last closed field line, likely involving ions expelled into the magnetosphere after being transversely accelerated. We demonstrate that, downstream of the ejection site, impulsive convection leads to prominent structuring of the tailward streaming particles with abrupt energy variations on small length scales. We stress that the changes in large-scale plasma convection are linked to processes internal to the magnetosphere occurring during substorms. The agreement between the numerical results and the data provides further evidences that there exists a close relationship between the *AE* magnitude and the convection electric field.

[1] CETP/CNRS, Saint-Maur des Fossés, France
[2] CESR/CNRS, Toulouse, France
[3] IKI, Moscow, Russia
[4] SwRI, San Antonio, Texas

1. Introduction

On August 27 1981, the PROGNOZ-8 spacecraft traveling inbound in the magnetospheric lobe (northern hemisphere) recorded several injections of ions with energies in the 200-eV to 1-keV range and propagating in the antisolar direction. In a previous study, *Vaisberg et al.* [1995] identified these tailward flowing ions as cold ion beams mainly consisting of ionospheric O^+ and suggested they originate from the cusp region. The bottom panel of Plate 1 shows the energy-time spectrogram recorded during this pass. In this panel, it can be seen that the PROGNOZ-8 spacecraft enters into the magnetosphere at approximately 06:30 UT as identified by the intense flux of energetic tailward flowing particles in the plasma mantle adjoining the magnetopause [*Rosenbauer et al.*, 1975]. Subsequently, as the spacecraft travels through the lobes in the vicinity of the midnight meridian plane, repeated structures are noticeable which are well separated in time and nearly shaped as inverted Vs. These structures occur from ~12.00 UT ($Z \sim 18\ R_E$) until ~23.00 UT ($Z \sim 8\ R_E$). The spacecraft then encounters the plasma sheet and ultimately the radiation belts.

It is of interest to note that the occurrence pattern of the ion injection structures and the simultaneous *AE* variations shown in the top panel of Plate 1 are quite similar in shape. As a matter of fact, a cross-correlation analysis between the *AE* magnitude and the energy of the maximum O^+ flux in the spectra reveals a correlation coefficient of ~0.7 between 13:00 and 19:00 UT with a time lag smaller than ~10 minutes (the *AE* change preceeding the energy change). This correlation suggests that the injection structures are linked to global changes in the magnetosphere and intimately related to substorm processes. As these *AE* variations are indicators of substorms which lead to temporary intensification of the large-scale magnetospheric plasma convection, the purpose of this paper is to revisit more quantitatively the results of *Vaisberg et al.* [1995] using three-dimensional calculations of single-particle trajectories in presence of a time-varying electric field.

2. Origin of Tailward Flowing O^+

In view of the good agreement between the *AE* variations and the observed injection pattern, we start with the assumption that the cross-tail potential drop can be directly related to

the *AE* magnitude. Such an assumption clearly is oversimplified. In particular, large changes in the *AE* magnitude provide evidences of modifications in the magnetospheric current system, and the above assumption does not explicitely take into account the induced electric field which should result from concurrent dynamical reconfiguration of the magnetosphere. Still, we will see from the simulation results that, in first approximation, the above assumption is not unreasonable in the magnetospheric lobes and that it leads to injection signatures which are consistent with those observed. As illustrated in the two upper panels of Figure 1, we focused on the 10:00 to 19:00 UT sequence of the PROGNOZ-8 pass and modeled the cross-tail potential drop (Φ) in a nearly linear manner with the *AE* magnitude, imposing threshold values of 40 kV for $AE \leq 200$ nT and 200 kV for $AE \geq 1000$ nT. The variations thus obtained are in qualitative agreement with previous detailed analysis of the relationship between the magnetospheric electric field and the current in the ionosphere [e.g., *Kamide and Baumjohann*, 1985; *Richmond et al.*, 1990; *G. Lu*, private communication, 1995]. Also, the resulting three-hour averaged potential drops (heavy dashed line in the top panel of Figure 1) are comparable to those derived using the *Maynard and Chen* [1975] equation and appropriate values of the *Kp* parameter, viz., $Kp = 3^+$ from 9:00 to 12:00 UT, $Kp = 5^+$ from 12:00 to 18:00 UT, and $Kp = 4^+$ from 18:00 to 21:00 UT [*Coffey*, 1981].

In order to perform single-particle analysis of the energy-time spectrogram in Plate 1, we sorted out the energy of the maximum O^+ flux during each 4-minute scan of one of the PROGNOZ-8 spectrometers. Note that the three spectrometers onboard PROGNOZ-8 were looking within ~ +/-7.5° from the Sun direction (i.e., close to the magnetic field direction). The energy profile is very similar for all three instruments and is illustrated in the third panel from top in Figure 1 (heavy solid line). The repeated inverted-V like structures mentioned above are clearly apparent in this panel, and their modulation according to the *AE* magnitude is readily noticeable by comparison with the second panel from top. To identify the origin of these tailward flowing ions, we performed numerical trajectory calculations backward in time from the spacecraft location in the *Tsyganenko* [1987] model (referred to as T-87 hereinafter). Each sample of the observed distribution was assigned a test O^+ with corresponding energy, assuming the particle to be nearly aligned with the magnetic field (i.e., nearly zero magnetic

moment) in the guiding center reference frame. Under such conditions, the particle pitch angle in the Earth's reference frame is essentially due to the local instantaneous **E×B** drift velocity. These pitch angles were found to be comprised between 5° and 15° at the spacecraft altitude (fourth panel from top in Figure 1), that is, in a range consistent with the direction of view of the PROGNOZ-8 detectors (*Vaisberg et al.* [1995]). As for the location, it must be stressed that the spacecraft encounter with the magnetopause at ~6:30 UT occurs somewhat lower in Z height than the position obtained in the T-87 model (see open square in the left panel of Figure 2). This difference is of importance when tracking the origin of the tailward flowing particles as it can lead to unrealistic mapping into the ionosphere. In the numerical calculations, we adjusted the model magnetopause and the observed one by heightening the spacecraft position by about 1.5 R_E in Z height (see left panel of Figure 2), that is in practice, by retarding the spacecraft orbit by about 3.8 hours.

The results of these calculations are shown in Plate 2 which shows the computed O^+ trajectories (color-coded according to their arrival time at the spacecraft) until the first mirror point encountered during backward tracing. These mirror points were all found below 1 R_E altitude. Also, the three lower panels of Figure 1 present the magnetic local time (MLT), the invariant latitude (ILAT) and the time of flight of the particles at mirror point. It can be seen in these panels that most of the ions originate from a narrow region in the ionosphere, both in MLT (between ~10 00 and ~11 00 hours) and in ILAT (between ~70° and ~80°). Here, it should be pointed out that the numerical results are fairly sensitive to the particle pitch angle at the satellite position as well as to the model adopted for the time-varying electric field. Trial and error computations showed that only particles nearly aligned with the magnetic field and drifting in an electric field nearly proportional to the AE magnitude originate from the topside ionosphere during the time interval under consideration. Other combinations gave unrealistic sources of O^+ located well above the ionosphere or even in the outer magnetosphere.

On the other hand, the vertical bars in the third panel from top reveal initial energies for these O^+ between ~100 eV and several hundreds of eV. These results clearly corroborate the suggestion made by *Vaisberg et al.* [1995] that these ions originate from the cusp region. In particular, the T-87 model used in these calculations ($Kp = 4,4^+$) places the last field line which

is closed in the dayside sector near 75° ILAT, and it can be seen that the ions detected by PROGNOZ-8 originate from within a few degrees on either side of this last closed field line. Significant wave activity is known to occur in this region of the high-latitude ionosphere [e.g., *Lundin*, 1988] and from the present results (i.e., characteristic energy of the order of a few hundreds of eV and pitch angle of 90° below 1 R_E altitude), ion conics locally produced via transverse heating are likely to be the source of the observed tailward flowing O^+.

3. Impulsive Magnetospheric Convection

An interesting feature of the PROGNOZ-8 data is the sharp inverted V-like structuring of the ion energy (third panel from top in Figure 1). In particular, clear interruptions are noticeable between two successive structures which cannot be interpreted simply from geomagnetic mass spectrometer [*Lockwood et al.*, 1985] effects in steady state. Indeed, ExB drift in presence of a constant dawn-to-dusk potential drop leads to spatial dispersion of particles with different energies (or masses) but in a continuous manner. This clearly is incompatible with the dispersion pattern observed. To account for the abrupt variations portrayed in Figure 1, one must consider temporal effects within the geomagnetic mass spectrometer. To do so, we performed numerical trajectory calculations forward in time from a given source in the topside ionosphere, adopting a time-varying potential drop as shown in the top panel of Figure 1. In view of the two bottom panels of Figure 1, the source in the ionosphere was taken to extend over 1° ILAT on either side of the last closed field line at 11.00 MLT. Test O^+ were launched from this line source at distinct times (by steps of 10-minutes) throughout the 10:00-19:00 UT interval.

Examples of the trajectories achieved are given in Figure 2. In this figure, one of the O^+ (solid line) is initialized at 76° ILAT while the other (dashed line) is launched 10 minutes later from a higher invariant latitude (77° ILAT). As a general comment, it can be seen in the upper right panel of Figure 2 that, in both cases, a significant energy gain (from 300 eV up to ~600 eV) is obtained after about 10-minute time of flight as the particles travel through a region of enhanced field line curvature. As can be seen by comparison with the center right panel, this energy gain essentially occurs in the parallel direction as a result of curvature drift through the

convection electric field equipotentials [e.g., *Cladis*, 1986]. It is also apparent that phasing between the particle orbits and the time-varying convection electric field (lower right panel of Figure 2) leads to substantial variations in the net particle path. Most notably, the O^+ launched from a higher ILAT (dashed line) which should intercept the spacecraft at a later time and a lower Z height in the magnetospheric lobe, is actually recorded at a position similar to that of the O^+ originating from a lower ILAT (solid line). This phasing effect combined with the above curvature-related acceleration can provide the mechanism for the well-separated inverted V-like structures in Figure 1.

This can be appreciated in Figure 3 which shows the energy variations obtained along the satellite pass assuming either a constant (100 kV) dawn to dusk potential drop (top panel) or a time-varying one (second panel from top). For simplicity, a 300-eV initial energy was considered in both cases. In the steady-state case (top panel), a continuous pattern is obtained, exhibiting a monotonous energy decrease from ~700 eV at 10.30 UT down to ~450 eV at 15:30 UT. These variations result from enhanced field line curvature in the outer cusp region, and thus larger energization for particles launched from lower ILATs. As mentioned above, this pattern is incompatible with that observed (light lines) even though the average energy is fairly well reproduced. In contrast, in the second panel from top, narrow O^+ structures with increasing and decreasing energies are noticeable from ~13:00 to ~18:00 UT, which resemble those observed. In particular, the energy modulation follows quite well the *AE* variation. This agreement is essentially qualitative as the amplitude of the energy change is substantially smaller than that observed. This latter effect may be due to the mono-energetic character of the model source considered. As for the time interval before ~13:00 UT, the computed pattern sharply differs from the observations. However, we note that this period of time corresponds to a fairly weaker magnetic activity ($Kp = 3^+$) which may lead to distinct characteristics of the outflow [e.g., *Yau et al.*, 1986].

Returning to the afternoon sequence, it must be stressed that the good agreement was obtained by shifting the numerical results by ~15 minutes toward earlier times or, equivalently, by considering that the injections respond to variations in the convection rate (*AE* magnitude) with a time delay of the order of 15 minutes. Within the limits of the model, this estimate is

compatible with that obtained by direct comparison of the energy spectra and the *AE* variation profile (see introduction). This time delay is significantly smaller than the time of flight of the particles from the ionosphere to the spacecraft (of the order of 40 minutes; see Figure 2), but it is comparable to the time required for an O^+ to travel over the distance between the spacecraft and the region of enhanced field line curvature where energy can be gained. In other words, what the numerical model suggests is that the structured injections observed do not result from a temporal modulation of the O^+ source in the cusp region (which would take too long to propagate down to PROGNOZ-8) but from the time-varying electric field acting upon the particles during their magnetospheric transport. This mechanism which operates in the magnetospheric lobes is reminiscent of that discussed by *Mauk* [1986] in the near-Earth plasma sheet whereby phasing between a surging electric field and the particle longitudinal motion leads to repeated injection patterns.

Finally it should be pointed out that, due to the strong variability of the particle drift paths with time (as illustrated at left in Figure 2), temporary flux dropouts are obtained in Figure 3 which are consistent with those featured in the data. These flux dropouts call for a limited extension of the source region in the ionosphere. Indeed, it can be seen in the second panel from bottom in Figure 3 that each injection involves ions originating from lower ILATs owing to the intensifying magnetospheric convection. In contrast, after each injection, the upper latitudinal limit set on the source region (which extends from 71° ILAT up to 79° ILAT) prohibits particle transport from higher ILATs to the spacecraft. Note moreover in the bottom panel of Figure 3 that the model O^+ have pitch angles in the range of the PROGNOZ-8 instrument (i.e., within ~15° from the magnetic field direction).

4. Summary

The intent of this paper was to provide quantitative insights into the tailward injections of O^+ ions reported by *Vaisberg et al.* [1995] using numerical trajectory calculations. The clear correlation we found between the observed injections and the magnetic activity (as viewed from the *AE* variation) suggests to consider the effect of sudden enhancements in the magnetospheric convection rate. The interpretation framework developed in this study clearly

is a simplified description of particle transport during such events. Nevertheless, there are clear indications that impulsive convection is at work and is responsible for the observed injections, namely: (1) numerical simulations of this effect place the source of the tailward propagating ions in the vicinity of the dayside cusp, i.e., in a region known to be an active source of O^+, and (2) steady-state plasma convection cannot lead to a dispersion pattern compatible with the observations. In contrast, the repeated injection structures as well as the flux dropouts between them are well reproduced if one considers large electric field variations on short time scales. These variations lead to distinct energy gains during transport from the ionosphere as well as intricated drift paths which occasionally intercept the spacecraft. It may be that part of this electric field intensification is of inductive nature though the present study lumps it with the large-scale convection. These results clearly exemplify the role of substorm expansion related electric fields in the magnetospheric lobes.

References

Cladis, J. B., Parallel acceleration and transport of ions from polar ionosphere to plasma sheet, *Geophys. Res. Lett., 13*, 893, 1986.

Coffey, H. E., Geomagnetic and solar data, *J. Geophys. Res., 86*, 11,470, 1981.

Kamide, Y., and W. Baumjohann, Estimation of electric fields and currents from international magnetospheric study magnetometer data for the CDAW 6 intervals: Implications for substorm dynamics, *J. Geophys. Res., 90*, 1305, 1985.

Lockwood, M., T. E. Moore, J. H. Waite, Jr., C. R. Chappell, J. L. Horwitz, and R. A. Heelis, The geomagnetic mass spectrometer - Mass and energy dispersions of ionospheric ion flows into the magnetosphere, *Nature, 316*, 612, 1985.

Lundin, R., On the magnetospheric boundary layer and solar wind energy transfer into the magnetosphere, *Space Sci. Rev., 48*, 263, 1988.

Mauk, B. H., Quantitative modeling of the "convection surge" mechanism of ion acceleration, *J. Geophys. Res., 91*, 13,423, 1986.

Maynard, N. C., and A. J. Chen, Isolated cold plasma regions: Observations and their relation to possible production mechanisms, *J. Geophys. Res., 80*, 1009, 1975.

Richmond, A. D., Y. Kamide, S.-I. Akasofu, D. Alcaydé, M. Blanc, O. de la Beaujardière, D. S. Evans, J. C. Foster, E. Friis-Christensen, J. M. Holt, R. J. Pellinen, C. Senior, and A. N. Zaitzev, Global measures of ionospheric electrodynamic activity inferred from combined incoherent scatter radar and ground magnetometer observations, *J. Geophys. Res., 95*, 1061, 1990.

Rosenbauer, H., H. Grunwaldt, M. D. Montgomery, G. Paschmann, and N. Sckopke, Helios-2 plasma observations in the distant polar magnetosphere: The plasma mantle, *J. Geophys., Res., 80*, 2723, 1975.

Tsyganenko, N. A., Global quantitative models of the geomagnetic field in the cislunar magnetosphere for different disturbance levels, *Planet. Space Sci., 37*, 1347, 1987.

Vaisberg, O. L., L. A. Avanov, J. L. Burch, and J. H. Waite, Jr., Measurements of plasma in the magnetospheric tail lobes, *Adv. Space Res.*, in press, 1995.

Yau, A. W., E. G. Shelley, and W. K. Peterson, Accelerated auroral and polar-cap ions: Outflow at DE-1 altitudes, in *Ion Acceleration in the Magnetosphere and Ionosphere, Geophys. Monogr. Ser.*, vol. 38, edited by T. Chang, AGU, Washington, D. C., 1986.

Plate Captions

Plate 1. (Top) *AE* index versus time. (Bottom) Color-coded energy-time spectrogram recorded by the PROGNOZ-8 spacecraft on August 27 1981. This spectrogram relate to particles propagating tailward with pitch angles smaller than 15°.

Plate 2. Model O^+ trajectories in the noon-midnight meridian plane. These trajectories are color-coded according to the arrival time at the PROGNOZ 8 location (heavy solid line).

Plate 1

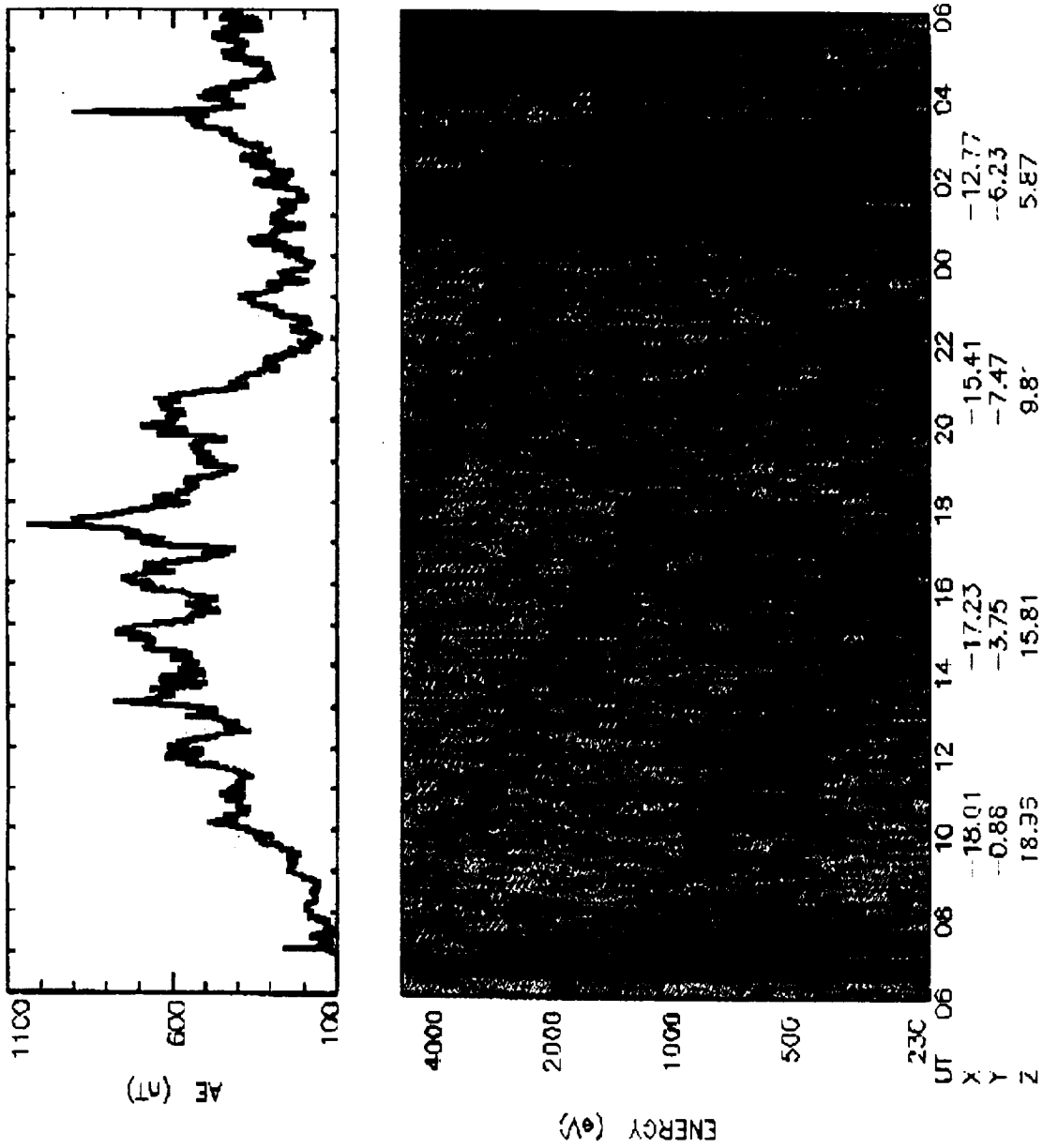

Pièce 2

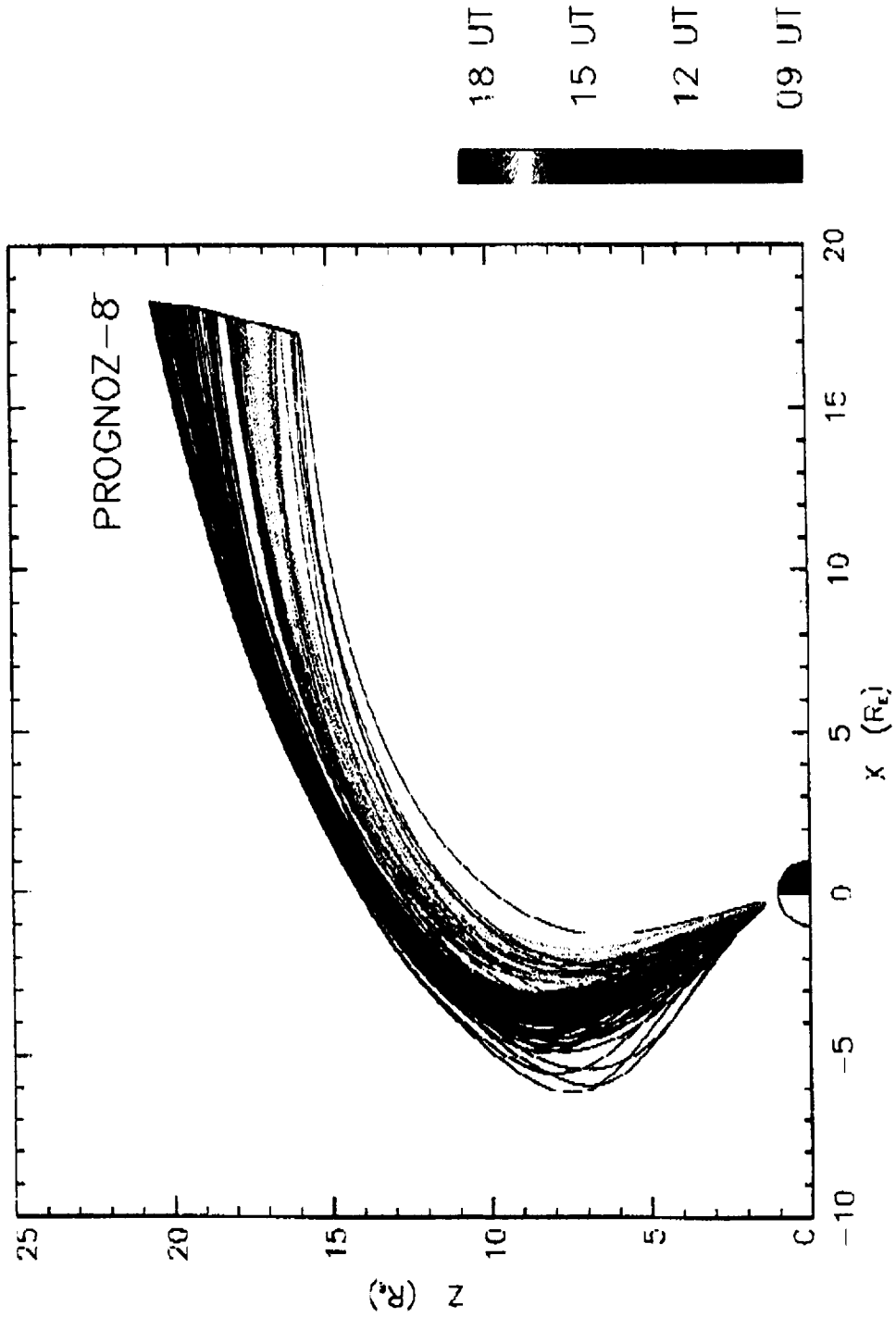
18 UT
15 UT
12 UT
09 UT
PROGNOZ-8
Z (R_E)
X (R_E)
25
20
15
10
5
0
-10
-5
0
5
10
15
20

Figure 1

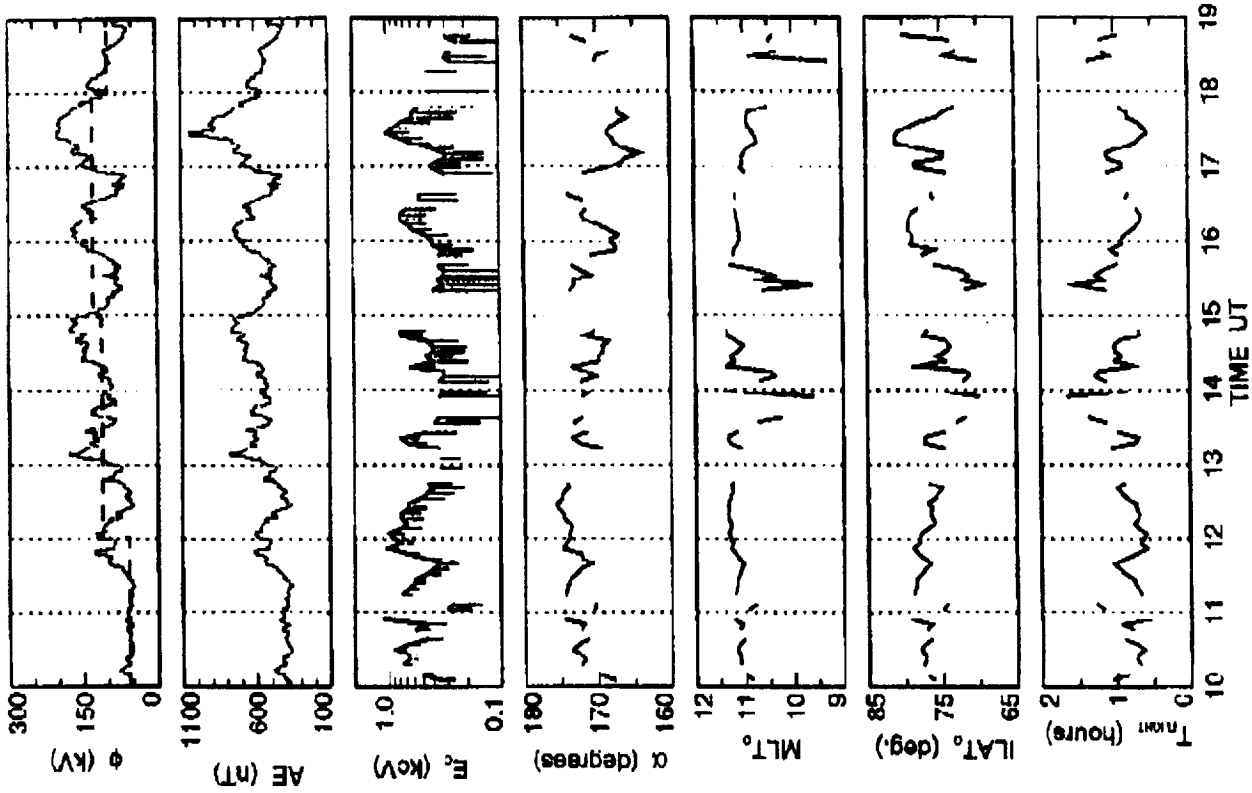
300
150
0
φ (kV)
1100
600
100
AE (nT)
1.0
0.1
E_c (keV)
180
170
160
α (degrees)
12
11
10
9
MLT_o
85
75
65
ILAT_o (deg.)
2
1
0
T_main (hours)
10
11
12
13
14
15
16
17
18
19
TIME UT

Figure 2

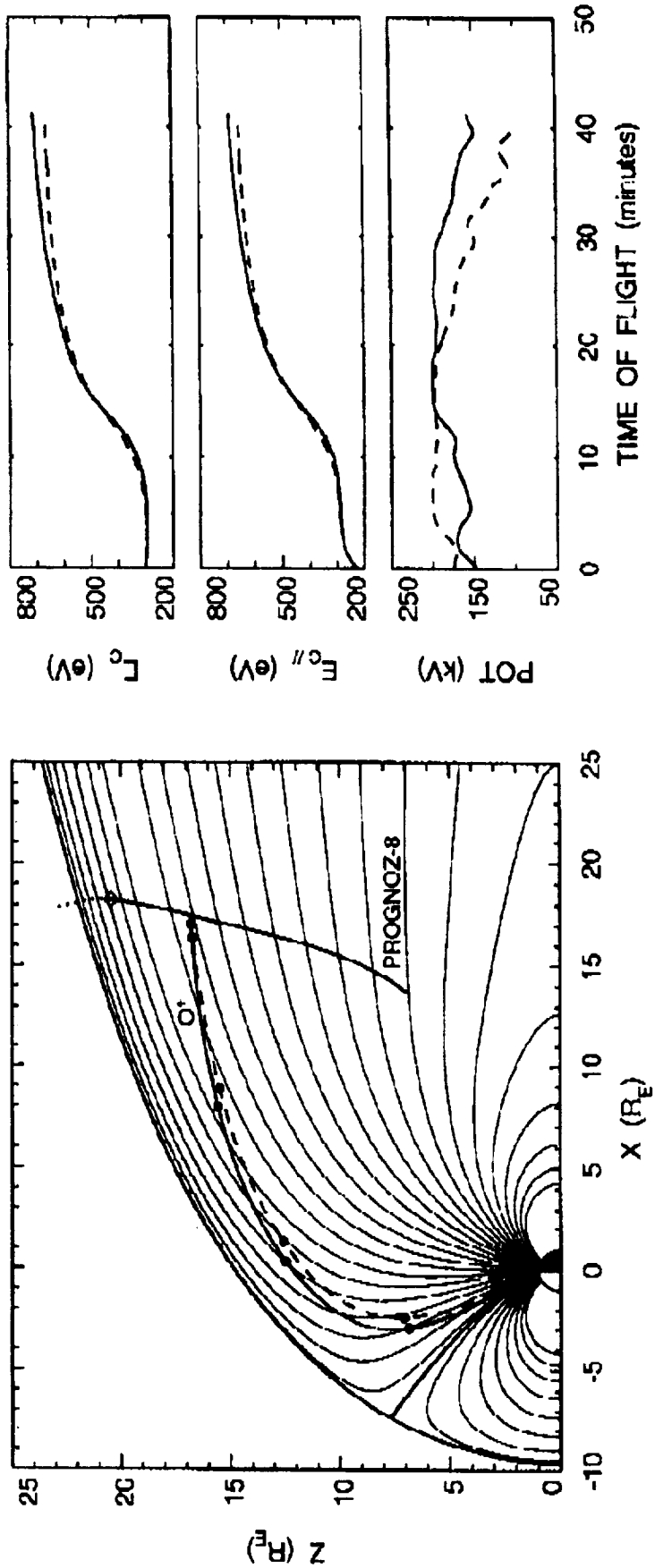

Figure 3

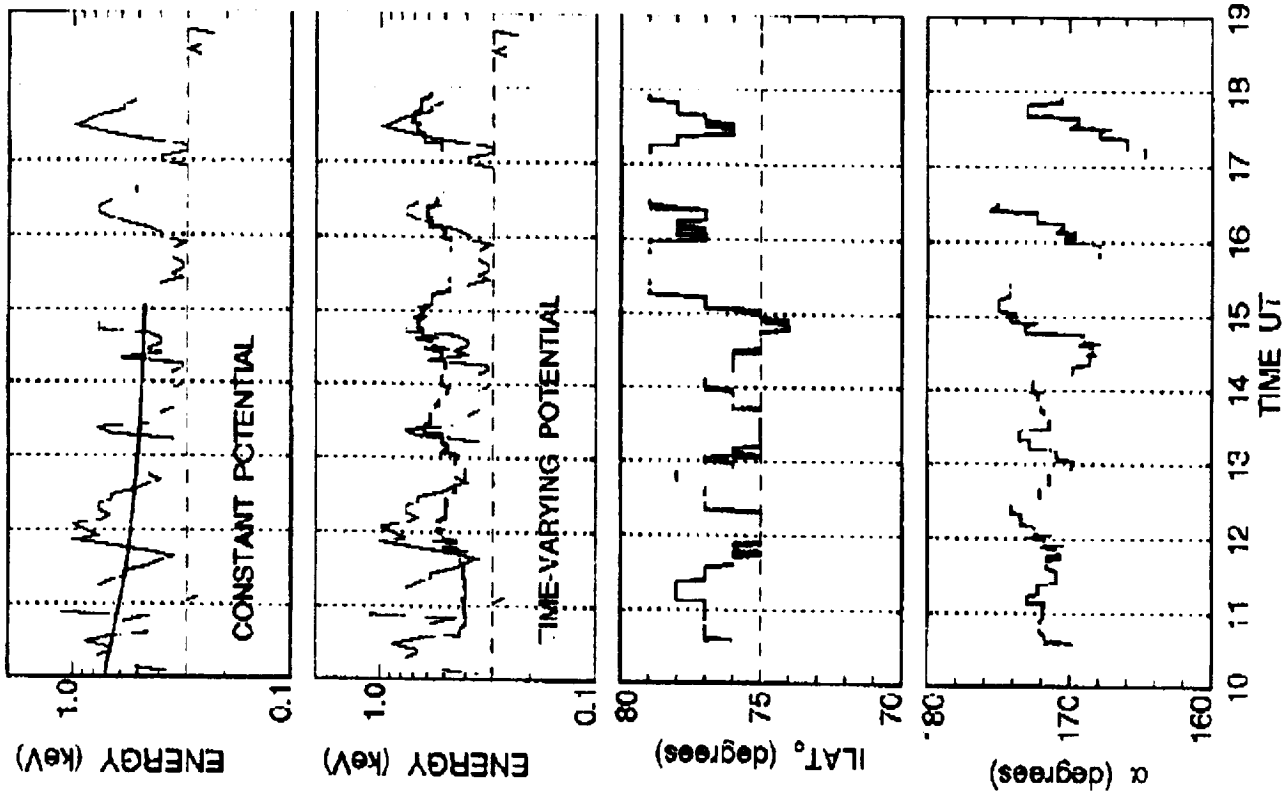
CONSTANT POTENTIAL
TIME-VARYING POTENTIAL
ENERGY (keV)
1.0
0.1
ILAT° (degrees)
80
75
70
α (degrees)
160
170
180
10
11
12
13
14
15
16
17
18
19
TIME UT

Appendix B

Pollack et al reprint
Giles et al. reprint

JOURNAL OF GEOPHYSICAL RESEARCH, VOL. 95, NO. A11, PAGES 18,969–18,980, NOVEMBER 1, 1990

A Survey of Upwelling Ion Event Characteristics

C. J. POLLOCK,[1] M. O. CHANDLER,[1] T. E. MOORE,[1] J. H. WAITE, JR.,[2]
C. R. CHAPPELL,[1] AND D. A. GURNETT[3]

Ionospheric ion upwelling in the vicinity of the dayside cleft has been studied, based primarily on data from the Dynamics Explorer 1 spacecraft. Using retarding ion mass spectrometer low-energy ion data and plasma wave instrument dc electric field data, bulk ion plasma parameters, including ion species density and field-aligned bulk velocity and flux, have been derived at points within a number of observed upwelling ion events for the ion species H^+, He^+, O^+, and O^{++}. The ion species bulk parameters near the source latitude are examined and compared. We find that the upwelling plasma is rich in O^+, which typically comprises ~90% of the particle density, followed by H^+ at somewhat less than 10%, and then He^+ and O^{++}, each comprising ~1% of the upwelling ion particle density. The upwelling O^+ ion flux is also commonly dominant over that associated with the other species, with normalized values near the source region which are typically near 10^9 cm^{-2} s^{-1}. The fractional upward H^+ flux is not as small as the fractional H^+ density due to the much larger H^+ upward flow velocities. Integration of the product of the normalized upward ion species flux and the upwelling ion occurrence probability (Lockwood et al., 1985) over the source area yields an estimate of the source strength of this low-altitude cleft region magnetospheric plasma source of 2.6×10^{25} ions s^{-1}.

1. INTRODUCTION

During recent years, it has been consistently demonstrated that the Earth's ionosphere acts as a significant source of magnetospheric plasma [*Shelley et al.*, 1972; *Young et al.*, 1977; *Ghielmetti et al.*, 1978; *Johnson*, 1979; *Balsiger et al.*, 1980; *Gorney et al.*, 1981; *Lundin et al.*, 1982; *Collin et al.*, 1984; *Yau et al.*, 1984, 1985; *Lennartsson and Shelley*, 1986]. In fact, it has recently been argued [*Chappell et al.*, 1987] that ionospheric plasma may fully populate the magnetosphere, with no significant solar wind source being required to account for observed magnetospheric charged particle populations. Recognition of the importance of the ionosphere as a source of magnetospheric plasma began with observations of heavy ions, previously believed to be gravitationally bound to low geocentric altitudes, at magnetospheric altitudes. As such observations continued to be reported, in diverse magnetospheric regions such as the ring current [*Johnson et al.*, 1977], the plasma sheet [*Peterson et al.*, 1981], and the plasma sheet boundary layer and tail lobes [*Eastman et al.*, 1984], it became apparent that escaping plasma transport from very low altitudes must be quite common. At the beginning of the 1980s, however, the questions of transport mechanisms and specific source regions were only beginning to be observationally addressed.

Observations of outflowing ionospheric ions have been reported by a number of authors in the last decade. Outflowing ion distributions which have apparently evolved, beginning with transverse (to **B**) acceleration and followed by magnetic mirror folding, have been observed near 1 R_E [*Sharp et al.*, 1977] in the topside ionosphere [*Klumpar*, 1979] and at sounding rocket altitudes [*Whalen et al.*, 1978; *Yau et al.*, 1983; *Moore et al.*, 1986*a*; *Kintner et al.*, 1989]. Since the launch of Dynamics Explorer 1 (DE 1), observation of low-energy ionospheric plasma outflows has become very common. The realization that the dayside magnetospheric cleft region represents a significant source of outflowing plasma began early in the DE mission, based on backward trajectory analysis of upflowing beams observed in high-altitude (2–4 R_E) polar cap field lines [*Waite et al.*, 1985]. This realization reached maturity with the work of *Lockwood et al.* [1985] who used DE 1 retarding ion mass spectrometer (RIMS) data to study the statistical occurrence of various types of ionospheric outflows. That work identified a persistent (occurrence probability exceeds 0.5 in source region) source of plasma emanating from the dayside auroral zone, showed that this source apparently favors the prenoon region of magnetic local time, and showed that there is a strong relationship between the low-latitude edge of the source region and the location of (usually downward) field-aligned currents. They labeled the observation of the distinctive RIMS spin-time signature associated with this outflow as an upwelling ion event (UWI). *Moore et al.* [1986*b*] and *Waite et al.* [1986] presented case studies of an UWI, observed near 1930 UT on day 71 of 1982. They derived bulk flow parameters for several species and demonstrated that the upwelling ion plasma core is hot and conically shaped, having undergone transverse energization at some lower altitude. They also noted a strong shear in the transverse electric field associated with the event.

The purpose of the present study is to more broadly investigate the bulk properties of UWIs, using RIMS and plasma wave instrument (PWI) quasi-static electric field data. The results of the study yield quantification of the densities and the upward field-aligned velocities and fluxes, for the ion species H^+, He^+, O^+, and O^{++}, associated with these flows. These parameters, as measured near the lower-latitude edge of the events, where the flows are most intense, will be presented. All of the available altitude normalized ion flux measurements from within the upwelling ion events are combined with the statistical occurrence probabilities derived by *Lockwood et al.* [1985] to produce spatial source strength distributions. Integration over these distributions yields an improved measure of the total low-energy ion outflow rate from this source region.

[1]NASA Marshall Space Flight Center, Alabama.
[2]Southwest Research Institute, San Antonio, Texas.
[3]Department of Physics and Astronomy, University of Iowa, Iowa City.

Paper number 90JA01095.
0148-0227/90/90JA-01095$05.00

2. INSTRUMENTATION

2.1. *The Spacecraft*

The observations presented in this report were gathered using instruments flown aboard the Dynamics Explorer 1 (DE 1) spacecraft. DE 1 was launched on August 3, 1981, into a highly elliptical polar orbit with apogee and perigee altitudes at 23,300 km (4.66 R_E, geocentric) and 570 km, respectively. The orientation of the orbit plane is fixed in the geocentric equatorial inertial (GEI) frame of reference, so that in the geocentric solar ecliptic (GSE) frame of reference, it is seen to rotate westward at a rate of 0.98°/day. This provides for approximately one full 360° rotation of the orbit plane in geocentric local time per year. Further, the DE 1 line of orbital apsides rotates about the negative orbit plane normal at a rate of 120°/year, so that the geographic latitudes of apogee and perigee drift retrograde at that rate. The spacecraft orbit, then, very nearly repeats itself, in the Earth's frame of reference, once every 3 years. These aspects of the spacecraft orbit influence our ability to study UWIs, not only because the source region has a limited geocentric solid angular extent, but also because the flowing plasma seems to evolve substantially with altitude. Therefore, the plasma characteristics which give rise to the distinctive RIMS UWI signature appear to exist only in a small region of space sampled by the spacecraft for several months once every 3 years. Furthermore, the orbit forces a phase-locked altitude-local time sampling which may bias the occurrence statistics of the local time extent of the upwelling ion source region. Other aspects of the DE mission have been described elsewhere [*Hoffmann and Schmerling*, 1981].

2.2 *Retarding Ion Mass Spectrometer*

Positive ion parameters presented in this report were obtained using the DE 1 retarding ion mass spectrometer (RIMS) [*Chappell et al.*, 1981]. The RIMS instrument consists of three similar sensor heads, one each viewing parallel and antiparallel to the spacecraft spin axis (negative and positive Z heads, respectively) and the third viewing in the spin plane (radial head). The two Z heads feature circular fields of view with half angles of 45°, while the radial head views a field which has a 45° half angle in the plane perpendicular to the spin plane and a 20° half angle in the spin plane. Since the DE 1 spin axis is nearly perpendicular to the geomagnetic field, the fields of view of the two Z heads are centered nearly perpendicular to that field, and the field of view of the radial head sweeps through a nearly full range of pitch angles with the spacecraft spin. All three sensor heads were designed to discriminate among incoming positive ions on the basis of energy per charge (0–50 eV/q), using a retarding potential analyzer (RPA), and on the basis of mass per charge (1–32 amu/q), using a magnetic mass spectrometer. Further, each sensor utilizes two detectors that are sensitive to ions with mass ratios of 4 to 1 such that, for example, while one detector is viewing O^+, the other is viewing He^+. The RPA on the radial head failed in late 1981, with the retarding grid having become electrically grounded to the spacecraft chassis so that, subsequent to the failure date, all ions with energies per charge greater than any positive spacecraft potential were passed into the magnetic mass spectrometer. The mass spectrometer, in turn, is characterized by a finite energy passband, whose width is dependent upon the species mass per charge and varies from approximately 250 eV for H^+ down to 16 eV for O^+. The upwelling ion densities, field-aligned bulk velocities, and fluxes presented below were derived using ion data from the RIMS radial head.

2.3. *Quasi-Static Electric Fields*

Quasi-static electric field data presented in this report and used in deriving ion bulk parameters were obtained using the Z axis antenna of the plasma wave and quasi-static electric field instruments [*Shawhan et al.*, 1981]. This tubular, 9-m (tip to tip) antenna is sensitive to the electric field component perpendicular to the spacecraft spin plane. The geomagnetic field is nearly (within 5° in 95% of our cases and always within 12° for our data set) contained within the DE 1 spin plane, so that the Z component electric field is associated with convective plasma drifts which are approximately within the spin plane and perpendicular to the ambient geomagnetic field. This electric field component is provided at a rate of 16 samples s^{-1} over a nominal range of 0.5 mV m^{-1} to 2 V m^{-1}. Characteristics of this instrument which are pertinent to the analysis techniques employed in this study will be described below.

3. DATA ANALYSIS

3.1. *Data Selection*

The observations presented here are taken from a subset of upwelling ion events identified by M. Lockwood through a survey of the RIMS data as displayed in the DE 1 microfiche (with format similar to Figure 2*a* displaying data for the species H^+ and He^+) in conjunction with his study of the occurrence of various types of terrestrial ion outflows [*Lockwood et al.*, 1985]. Lockwood et al. used a qualitative visual signature identification technique to identify these upwelling ion events. The RIMS spin-time upwelling ion event signature has been described elsewhere (see, for example, Plate 3 of *Lockwood et al.* [1985]). This signature is again illustrated in the O^+ data presented in Figure 2*a*, where the count rate in the O^+ channel is shown plotted in grey scale versus UT (along with certain orbital parameters) along the abscissa and the RIMS radial head viewing direction, with respect to the spacecraft ram direction, along the ordinate. The solid and dashed lines running through the spectrogram from left to right indicate viewing angles along the positive and negative geomagnetic field directions, respectively. For northern hemisphere passes, ions detected while viewing along the positive magnetic field direction are moving in the antifield direction and, therefore, away from the Earth. The signature of the event is evident in Figure 2, beginning near 2320 UT and continuing until just past 2327 UT. The ramp-like upward flux intensification, followed by a sharp cutoff and return to ram-dominated flow into the instrument at the low-latitude edge of the event, typifies the signature of these events used by Lockwood et al. in their fiche survey.

Having surveyed the available data obtained between October 1981 and October 1983, Lockwood et al. identified 86 upwelling ion events. These events were identifiable in the fiche for periods of time ranging from 1 to 15 min, providing a total of nearly 450 min of observation within the events. Of these 86 events, we have selected 39 for inclusion in the analysis for this report. This selection was based, in part, on the requirement that the RIMS instrument be operating in a mode without aperture bias applied to the instrument entrance and on the further requirement that the measured Z component of the electric field was deemed reliable. The RIMS instrument features an aperture bias capability, whereby a negative electrostatic potential may be applied to a grid at the entrance aperture, in order to overcome the effects of a positive spacecraft potential, allowing access of very low-energy ions to the instrument. Of the 86 upwelling ion events identified in the Lockwood et al. study, 20 were from times when RIMS was

operating in the aperture bias mode, and analysis of these events has been deferred pending the development of routine analysis tools for this mode. For another 8 events, either the digital RIMS data or the attitude and orbit data were unavailable. Of the remaining 58 events, 16 were rejected because the Z antenna dc electric field data were deemed unreliable. This antenna has a length of 9 m tip to tip, as compared with the spin plane antenna which is 200 m long. It is known to be subject to stray fields that originate from differential spacecraft charging and can have large amplitude relative to the fields of interest. This left 42 events, from which 2 were rejected due to a combination of no electric field data available and highly variable, difficult to interpret ion data and 1 was rejected due to the apparent presence of a telemetry dropout during the event. Thus, 39 of the original 86 events, or 45%, have been processed to obtain ion bulk parameters along the spacecraft track. Of these, 5 have no electric field data, and values of $E_z = 0$ have been assumed. These 39 events, consisting of a total of nearly 200 min of observation, constitute the data set used in the present analysis.

3.2. *Derivation of Ion Bulk Parameters*

Due to the failure of the RIMS radial head RPA, ion energy spectra are not available in the spin plane data. This situation has led to the development of an alternative technique for deriving ion bulk parameters from the RIMS radial heat data. This geometrical technique, developed by *Chandler and Chappell* [1986], provides a measure of the field-aligned ion bulk velocity and field-aligned ion flux of all ions of a given species which fall within the energy passband of the magnetic mass spectrometer. Derivation of the field-aligned bulk velocity depends upon the presumption that there are three distinct contributors to the species bulk velocity in the spacecraft spin plane and frame of reference (see Figure 1). These contributors are the spacecraft-induced ram velocity ($\mathbf{V}_r$), **E x B** drift ($\mathbf{V}_{\mathbf{E}\times\mathbf{B}}$) and field-aligned drift ($\mathbf{V}_\parallel$) velocities. The spacecraft ram component is obtained from the orbit and attitude data base, while the **E x B** drift component is derived, using measured electric and magnetic fields, as

$$\mathbf{V}_{\mathbf{E}\times\mathbf{B}} = \frac{c\mathbf{E}\times\mathbf{B}}{|\mathbf{B}|^2} \approx 10^{-2}\frac{E_z}{|\mathbf{B}|}\hat{(\mathbf{y})} \quad \frac{\text{km}}{\text{s}} \tag{1}$$

where, on the extreme right-hand side, E_z is the measured Z component of the electric field, expressed in mV m^{-1}, and **B** is expressed in gauss. Here, we have used the approximation that the magnetic field lies in the spin plane of the DE 1 spacecraft. As was mentioned above, this approximation is always good to within 12° for the data used in this study. Then, the total spin plane ion species bulk velocity in the spacecraft frame of reference is given as

$$\mathbf{v}_{\text{spin plane}} = (v_{rx} + v_\parallel)\,\hat{\mathbf{x}} + (v_{ry} + v_{\mathbf{E}\times\mathbf{B}})\,\hat{\mathbf{y}} \tag{2}$$

where $v_\parallel$ is the field-aligned bulk velocity we are trying to determine, v_{rx} and v_{ry} are the X and Y components of the ion ram velocity, and

$$\hat{\mathbf{x}} = \hat{\mathbf{B}} \qquad \hat{\mathbf{y}} = \hat{\mathbf{z}} \times \hat{\mathbf{x}} \qquad \hat{\mathbf{z}} = -\hat{\omega}_{sc} \tag{3}$$

Note that positive values of field-aligned bulk velocity correspond to upward and downward drifts in the southern and northern hemispheres, respectively. All field-aligned drifts presented in this paper are upward, however, and we have plotted these as positive. Here, $\hat{\omega}_{sc}$ is parallel to the DE 1 spin angular momentum. The unknown parallel drift velocity is given as

$$v_\parallel = (v_{ry} + v_{\mathbf{E}\times\mathbf{B}})\cot(\alpha) - v_{rx} \tag{4}$$

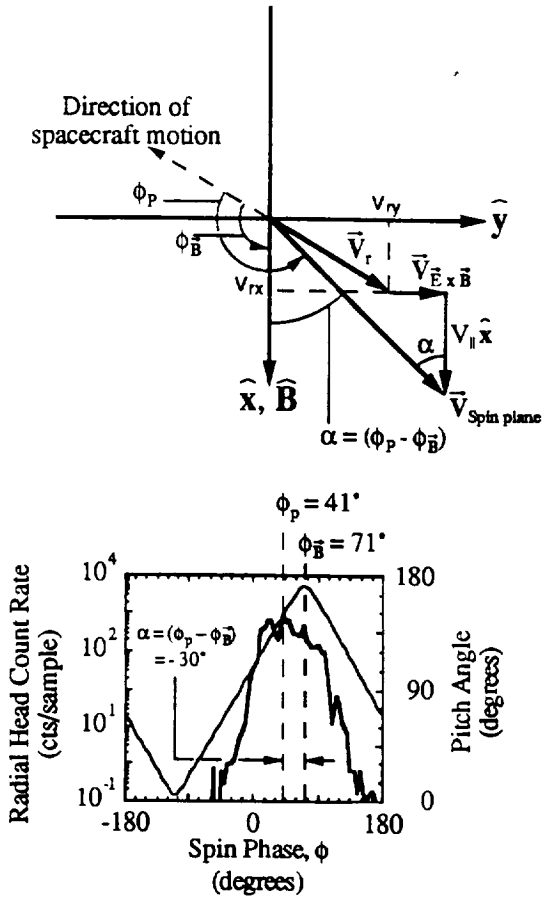

Fig. 1. The coordinate system and geometry used for computing ion species upward bulk velocity from RIMS spin curves and PWI electric field data is displayed in the top panel. At the bottom, a typical RIMS count rate spin curve is shown, and the meaning of angles identified in the sketch above is illustrated. The magnetic pitch angle at which counts are accumulated is displayed as the triangular wave in the bottom panel.

The angle α is measured as the difference

$$\alpha = \phi_p - \phi_B \tag{5}$$

in spin phase angles between the location (ϕ_p) of the centroid of the distribution of ion counts with spin phase and the direction (ϕ_B) along which the positive magnetic field direction is viewed. Spin phase angle (ϕ) is that measured about $+\mathbf{z}$, from the spacecraft velocity vector to the RIMS radial head look direction. In order to derive the field-aligned ion flux for a given species, the product of the instrument count rate and calibrated instrument sensitivity factors are cosine weighted, with respect to the spin plane velocity vector (given in equation (2), above), and integrated over spin phase angles, yielding the flux (J_T) along the direction of the total spin plane velocity vector. The field-aligned flux is then obtained as the product

$$J_\parallel = J_T \cdot \frac{v_\parallel}{|\mathbf{v}_{\text{spin plane}}|} \tag{6}$$

and the species particle density is estimated as

$$n \approx \frac{J_T}{|\mathbf{v}_{\text{spin plane}}|} = \frac{J_\parallel}{v_\parallel} \tag{7}$$

where $|\mathbf{v}_{\text{spin plane}}|$ is determined using equation (2), having deter-

mined $\mathbf{v}_{E\times B}$ using measured fields as in equation (1), the ram components using orbit and attitude data in conjunction with magnetic field data, and $v_\parallel$ using equation (4) as described above. Our estimate for the species particle density is actually a lower bound, which disregards the possible presence of ions at energies lower than any positive spacecraft potential. This technique has been applied to data obtained in and near the 39 upwelling ion event intervals included in this study. We have used 1-min data averages throughout in analyzing the PWI electric field and the RIMS ion data.

3.3. *Error Analysis*

The above analysis involves two potential sources of error. First, for angles (α) near π or 0, corresponding to highly field-aligned or anti-field-aligned flows, the analysis produces values of $v_\parallel$ which are unrealistically large and positive or negative, respectively, for any nonzero difference $(v_{rv} - |v_{E\times B}|)$. We have discarded results which yield a total velocity so large that the corresponding ion kinetic energy per charge would be too large to be passed by the magnetic mass spectrometer. The accuracy with which we can determine α is on the order of $\pm 2°$, so that the analysis of flows which are in actuality within $\sim 2°$ of being field-aligned would be expected to produce values of $v_\parallel$ whose magnitudes are arbitrarily large. We have propagated an uncertainty of $\pm 2°$ in α through the analysis.

Second, the accuracy with which we know the values of the Z component of the dc electric field is limited by the performance of the PWI Z antenna in these low- to medium-density plasma regimes. We have carefully examined the electric field data on a case-by-case basis and selected only those events characterized by spin-averaged field profiles which vary smoothly, or with reasonably small amplitude, both immediately prior to and following the upwelling event itself, as identified in the ion data. Further, we have derived estimates of the magnitude of the uncertainty in the values of E_z, in the manner described below, and propagated these through the analysis. In processing the electric field data, we have begun by producing 4-s (spacecraft spin period = 6 s) averages ($E_{z,4\ s}$) and standard deviations ($\sigma_{4\ s}$) about the means of the 16 sample s^{-1} data, producing 15 pairs of values per minute. The mean values of these two quantities represent 1-min averages of E_z, which we have used in the computation of ion bulk parameters, and of $\sigma_{4\ s}$, which represents a spin period time scale error estimate. Further, a 1-min time scale error estimate ($\sigma_{60\ s}$) is derived as the standard deviation of the 15 values of $E_{z,4\ s}$ about their mean. These two error estimates, in addition to a nominal uncertainty of 4 mV m^{-1}, have been treated as independent contributors to the uncertainty in E_z, as

$$\Delta E_z = \sqrt{\sigma_{4\ s}^2 + \sigma_{60\ s}^2 + \left(4\ \frac{\text{mV}}{\text{m}}\right)^2} \qquad (8)$$

4. RESULTS

4.1. *Results for a Single Pass*

Figure 2 illustrates the nature of the data used in the analysis and the results for a single pass on day 60 of 1982. These results are not typical, in that this was a particularly intense event, observed at unusually low altitude on a day characterized by a sustained high level of geomagnetic activity. The ion and electric field data shown in Figure 2 are plotted against UT, with various spacecraft orbital parameters also indicated along the horizontal axis. The interval selected shows a DE 1 pass from the northern polar cap across the dayside auroral zone.

Figure 2*a* shows the RIMS radial head spin time spectrogram for O^+ and has been described above in the context of data selection. The full time resolution Z component electric field data and the processed Z component data are shown in Figure 2*b* and Figure 2*c*, respectively. The full time resolution electric field data in Figure 2*b* show not only the steady offset induced by spacecraft motion across the magnetic field, but also a distinct modulation induced by nonstationary spacecraft sheath structure. Recall that since the electric Z antenna is aligned with the spacecraft spin axis, spin modulation in this signal is not expected in the presence of spacecraft sheath structure unless the structure changes with spin phase. Note the large-amplitude, unresolved excursions in the electric field signature near 2327 UT. The long wire electric antenna on DE 1 shows a similar signature, which is quite common near the UWI source region. The possible role of these large-amplitude and highly structured electric fields in producing the upwelling ion flows will be addressed in a future publication. The final electric field data product, which is used in computing the ion bulk parameters, is shown in Figure 2*c*, where values of ΔE_z as given in equation (8) are used in determining the size of the error bars. In these 1-min averages, the contribution induced by spacecraft motion has been explicitly removed, and the spin modulation removed by the averaging procedure. It is evident from a comparison of Figures 2*b* and 2*c* that significant structure, present in the unprocessed field data, is lost in the 1-min data product.

In Figures 2*d* through 2*f* the bulk parameters ($V_\parallel$, $J_\parallel$, and n, respectively), derived as described above, are presented for each of the ion species H^+, He^+, O^+, and O^{++}. Although the field-aligned ion velocities and fluxes are generally upward throughout the interval, they are most pronounced during the minute extending from 2325:30 UT to 2326:30 UT. It is at this time that the event is said to maximize in intensity and that the spacecraft is thought to be directly downstream of the upwelling ion flow source, in the dayside polar cleft.

4.2. *Typical Flux, Velocity, and Density Levels at Event Maxima*

The ramplike upwelling ion signatures observed as the spacecraft passes from high latitudes through the dayside auroral zone, followed by sharp cutoffs at the low-latitude edge, are common features of UWI signatures. These features are interpreted in terms of a convective effect, whereby the source of the ion upwelling exists in a localized zone near the low-latitude edge of the event and ions are convected to higher latitudes, dispersing them poleward of the source. From this point of view, the region where the upward flux maximizes, near the low-latitude edge of the event, may be considered to be most closely associated with the source region. The ions observed in this region are characterized by the shortest flight paths from source to observer and, as we note, are those with the largest upward field-aligned velocities, slower particles having been convected further poleward by the time they reach the spacecraft altitude. We have therefore taken the ion bulk parameters measured at this location to be indicative of the intensity of a given event, with the proviso that there is a bias toward larger field-aligned velocities.

Having selected the analyzed data for 39 events, we have isolated the ion bulk parameters at the time in each event when the maximum flux was observed. Figure 3 shows a scatter plot of the measured maximum flux versus the inferred density for each of the four species: H^+, He^+, O^+, and O^{++}. Points lying along the two lines running through the plot represent upward bulk velocities of 1 km s^{-1} and 10 km s^{-1}. While the measured fluxes

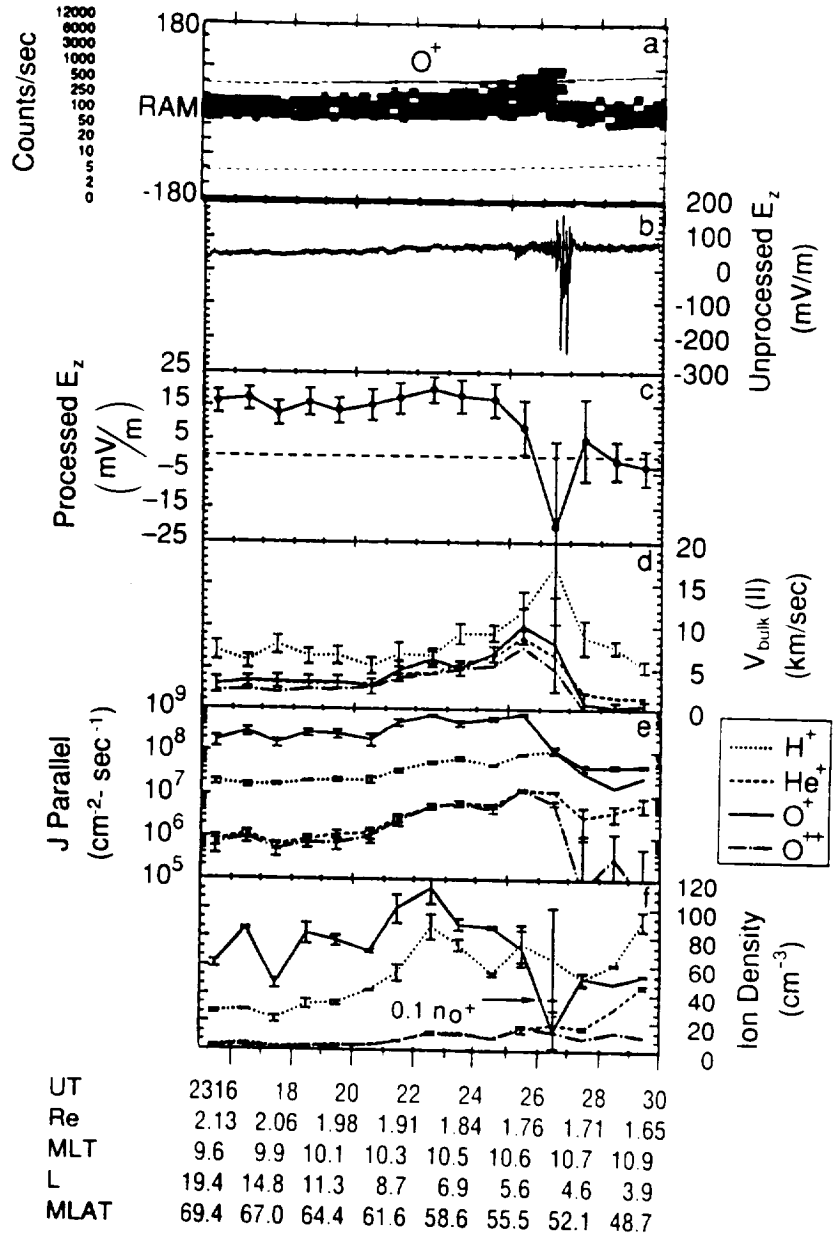

Fig. 2. RIMS ion data and PWI electric field data are displayed as functions of time for a dayside auroral zone pass on day 60 of 1982. The top panel shows a RIMS O^+ spin-time count rate spectrogram in standard RIMS format. The second and third panels from the top show PWI dc electric field data in almost raw and processed formats, respectively (see text). The bottom three panels display derived ion species bulk parameters of upward velocity, upward flux, and particle density for several ion species. Note that the O^+ ion densities have been divided by 10. Various orbital parameters, as well as UT, are listed along the abscissa.

and densities vary over several orders of magnitude, the upward velocities tend to lie between 1 and 10 km s^{-1} for the heavier species and near or above 10 km s^{-1} for the lighter species. Plots of the relative occurrence frequency of maximum density, field-aligned velocity, and flux observed in these events for the species H^+, He^+, O^-, and O^{++} are presented in Figures 4*a* through 4*c*, respectively. In the case of the maximum flux (Figure 4*c*), the flux values plotted along the abscissa have been mapped to a common altitude of 1000 km, according to an r^{-3} scaling law, while the densities and velocities are plotted as measured, irrespective of spacecraft altitude. This is in contrast to the flux values plotted in Figure 3, which are as measured, irrespective of altitude. In Figure 4, the species are differentiated by the plotting symbols used.

Figure 4*a* shows that these events are typically oxygen-rich near the source region with typical fractional and absolute O^+ ion densities of 0.9 and 1000 ions cm^{-3}, respectively. This represents somewhat large O^+ densities for these altitudes (~1.5–2 R_E) as compared with polar cap field lines (see, for example, the total electron density results of *Persoon et al.* [1983], or the ion species density results of M. O. Chandler et al. (Observations of polar ion outflows, submitted to *Journal of Geophysical Research*, 1989). Such large O^+ densities are indicative of increased ionospheric scale heights, probably associated

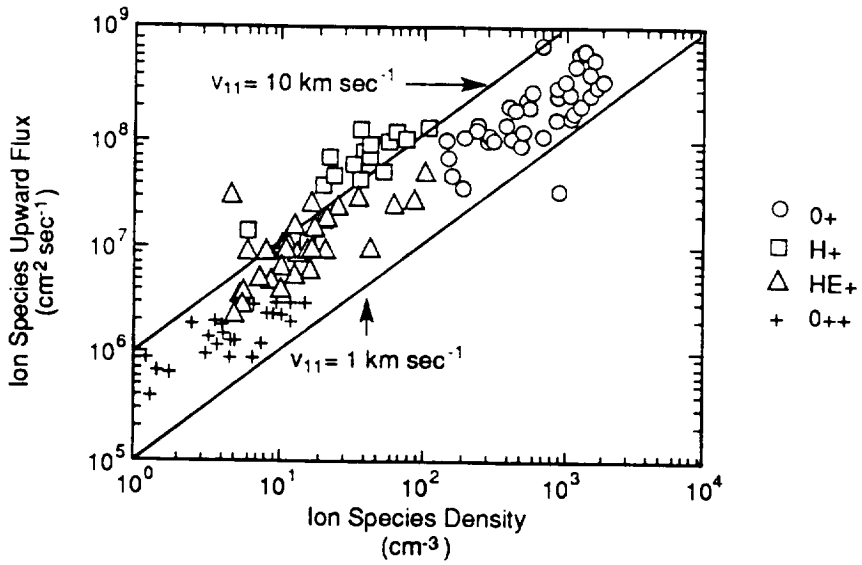

Fig. 3. A scatter plot of measured upward ion flux versus measured ion density at the low-latitude edge of UWIs is shown for several ion species. The data were gathered over a range of DE 1 altitudes between 1.3 and 2.1 R_E. The straight lines running through the plots show the loci of points for ions moving upward at 1 km s^{-1} (lower line) and 10 km s^{-1} (upper line).

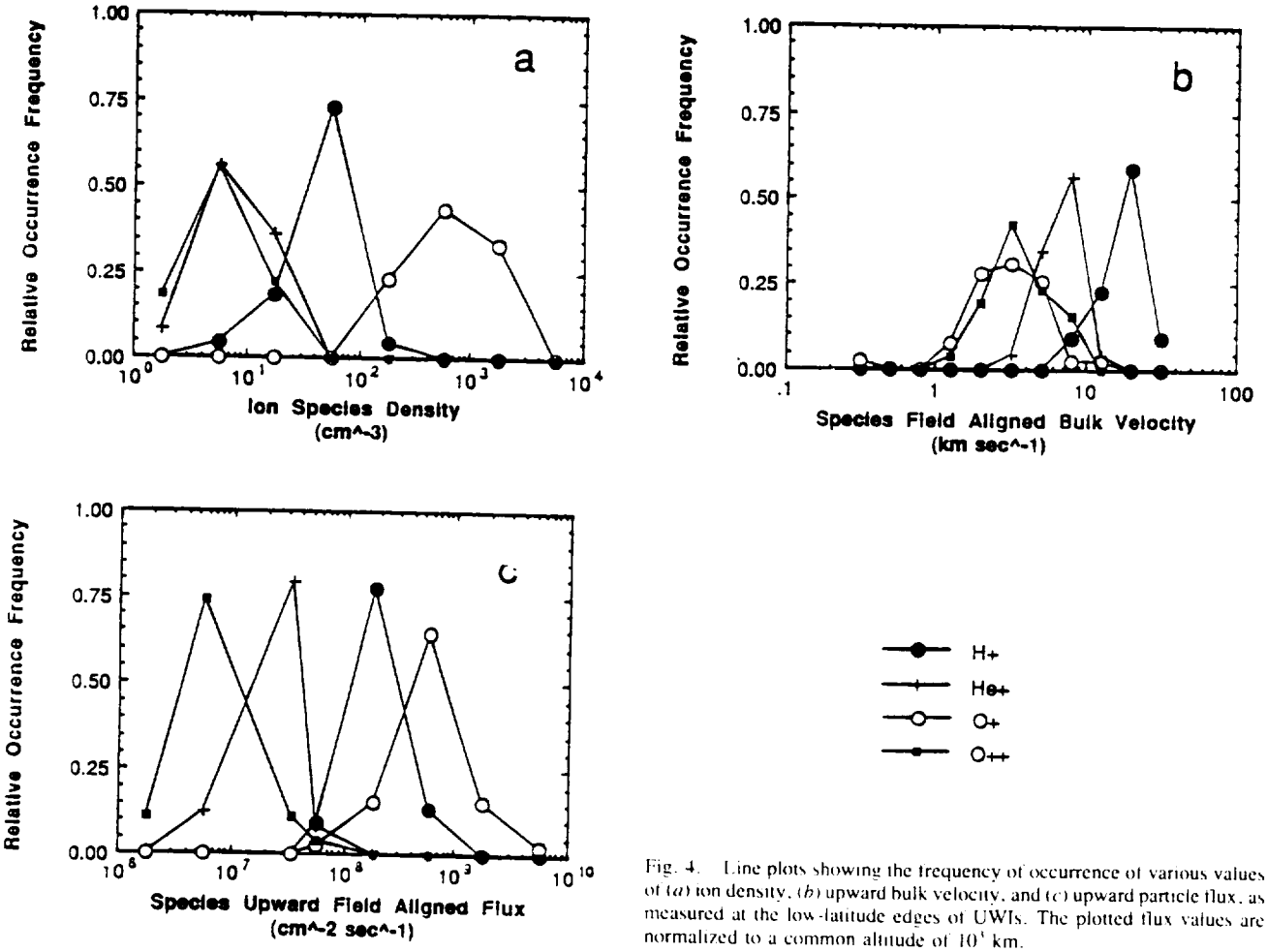

Fig. 4. Line plots showing the frequency of occurrence of various values of (*a*) ion density, (*b*) upward bulk velocity, and (*c*) upward particle flux, as measured at the low-latitude edges of UWIs. The plotted flux values are normalized to a common altitude of 10^4 km.

with bulk ionospheric heating at much lower altitudes. These O^+ density results are consistent with the model polar wind results of *Schunk and Sojka* [1989]. Our H^+ density results are in wide variance with those of Schunk and Sojka, however, with typical observed H^+ densities of ~100 ions cm^{-3} at geocentric distances between 1.5 and 2 R_E as compared with model results in excess of several thousand ions per cubic centimeter (at 2500 km altitude).

The upwelling O^+ flux (Figure 4*c*) is also dominant over that associated with the other ions, with maximum scaled flux levels which typically approach 10^9 ions cm^{-2} s^{-1}, far in excess of predicted polar wind O^+ flux levels. On the other hand, the largest field-aligned velocities are measured in the H^+ ions, for which the upward bulk velocity is generally greater than 10 km s^{-1} near the latitude of the source region. More modest bulk velocities, of the order of 3 km s^{-1}, are typically observed in the O^+ ions.

We have found that the measured upward field-aligned bulk velocity varies systematically with species mass per charge, with light ions moving upward with higher velocity than the heavier ions. This point is illustrated with Figure 5, where characteristic upward bulk velocities are plotted as a function of species charge per unit mass. The distribution of velocities shown in Figure 5 is dominated by the H^+ ions (at $q/m = 1$) which are clearly moving upward much faster than the other species, although the He^+ ions are also significantly faster than the two species (O^+ and O^{++}) plotted. The trend is not as strongly supported when comparing the O^+ and O^{++} ions either in this figure, which is derived from the mean values of the bulk velocities observed at maximum flux, or on a case-by-case basis, where the O^+ is often seen to be moving upward with higher velocity than the O^{++}. We have shown a power law fit to the data in Figure 5, which yields

$$v_{\parallel} \cong 17 \left\{ \frac{Z}{(m/m_p)} \right\}^{0.6} \quad \frac{\text{km}}{\text{s}}$$

where Z is the ion charge state and (m/m_p) is the ion mass, normalized to the proton mass. Processes yielding energies proportional to ion charge but independent of ion mass would give rise to a square root dependence of $v_{\parallel}$ upon (q/m). An example of such a process is acceleration in a parallel (to **B**) electric field. However, the warm and anisotropic nature of these upwelling plasmas, along with their high density, suggests that the outflow arises due to transverse heating in the topside of an already warm cleft ionosphere, followed by upward magnetic folding of the ion distributions. The analysis of the thermal properties of these events is beyond the scope of this report and will be reported in a future paper. However, it is to be noted that upwelling ion flows are typically warm and anisotropic, with temperatures (transverse to **B**) of several electron volts, as reported by *Moore et al.* [1986*b*].

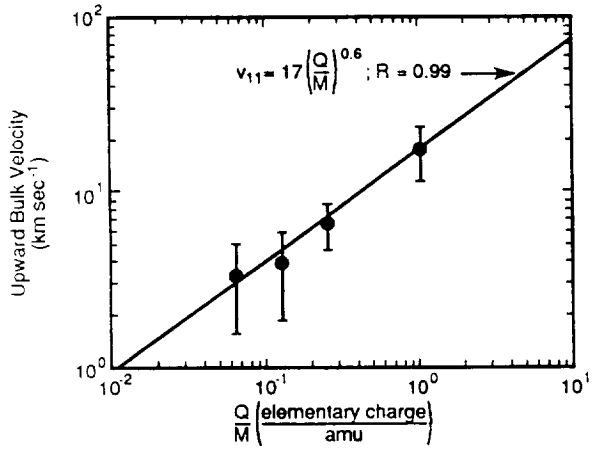

Fig. 5. Mean values of ion species upward bulk velocities are plotted versus the species charge per unit mass. The velocities plotted are those derived from measurements taken at the lower-latitude edges of UWIs, where the upward flux is seen to maximize. The line indicates a power law fit to the data, with the fit parameters indicated.

Delcourt et al. [1989] have modeled the evolution of these ion flows using particle ray tracing techniques in realistic gravitational, electric, and magnetic fields. They have found that the upwelling ions generally escape the Earth's immediate vicinity in large numbers and travel in an extended plume over the polar cap into the geomagnetic tail and plasma sheet, where the heavier species are rather dramatically accelerated as they cross the neutral sheet.

4.3. *Bulk Parameter Correlations and Dependence on Location and Geomagnetic Activity*

The relationship between spatial location and the occurrence of ion upwelling has been investigated by *Lockwood et al.* [1985]. Their study showed that for DE 1 altitudes below 3 R_E, geocentric, the probability of observing the asymmetric RIMS spin-time signature of an upwelling ion event peaks at near 0.7 in the prenoon magnetic local time (MLT) sector and at invariant latitudes (IL) between 75° and 80° (see their Plate 4*c*). The question arises as to whether the intensity of the upward flow shows systematic variation with the location of the source region. In Figure 6, we present scatter plots of the upwelling O^+ flux, measured during the minute of maximum intensity within the event and normalized to a common altitude of 1000 km, versus MLT (Figure 6*a*) and IL (Figure 6*b*). There is substantial scatter in the observations, with several particularly large flux values, and no apparent systematic trend. The intensity of the outflow does not seem to be correlated with the latitude or MLT at which the observations are made within the source region.

There is, however, some indication that the ion composition within these events varies systematically with magnetic local time, with the fractional minor species density increasing toward local noon. Figure 7 provides a convenient summary of the ion composition for a number of cases in which all four ion species were measured simultaneously. As noted earlier, the bulk of the ion plasma consists of O^+, comprising about 90% of the ion density, while H^+ contributes ~10%, and He^+ and O^{++} each contribute ~1%. The upwelling O^+ flux typically represents a smaller percentage (~70%) of the total upward flux, due primarily to the larger H^+ bulk velocities. In Figure 7, we show the fractional ion composition plotted versus the magnitude |MLT − 12| to illustrate the existence of a possible systematic relationship between proximity to local noon and ion composition within these events. Note that values are plotted along the abscissa without regard to whether data were collected in the prenoon or postnoon sector. The fractional composition of the minor species appears to increase with proximity to local magnetic noon. The case for the compositional dependence upon MLT is stronger for O^{++} (linear correlation coefficient = −0.7) than for the other species. The reason for this dependence is unclear. The O^+ density (and therefore total ion density) appears to decrease with proximity to noon, although the data are scattered (linear correlation coefficient $|R| \sim 0.3$), while the absolute minor species densities show no significant trend. These apparent trends in the ion composition could be anomalous, resulting from correlations between MLT and altitude imposed by the DE 1 orbit. Further study of this subject will be required.

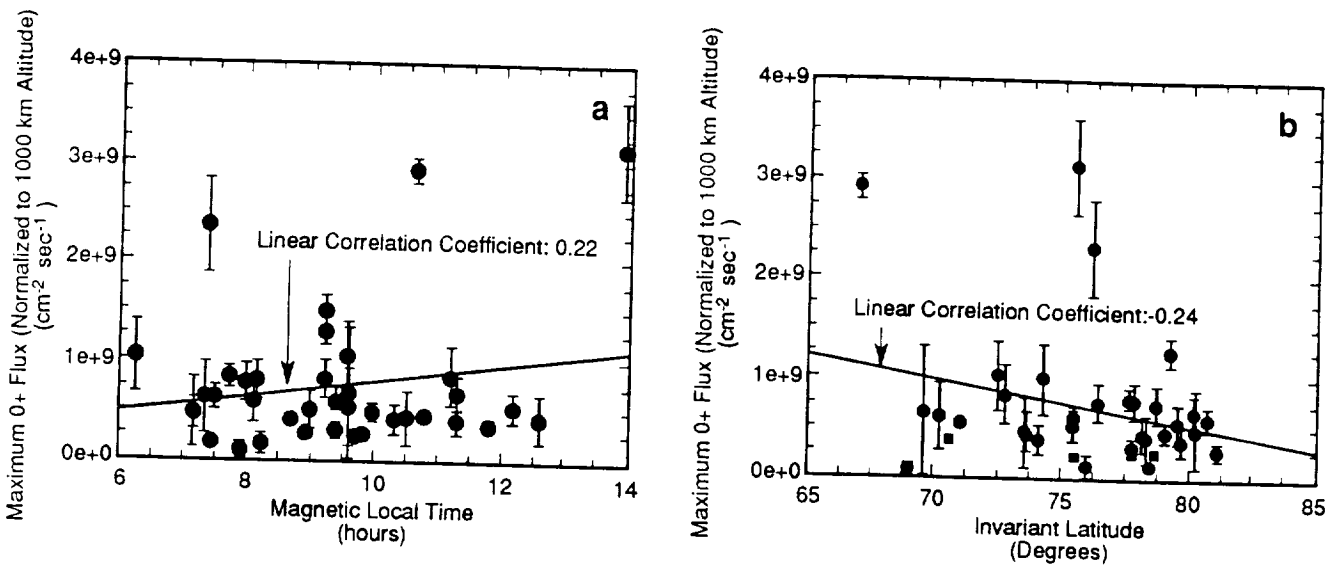

Fig. 6. Upward O^+ flux (normalized to 1000 km altitude) is plotted in scatter plots versus (*a*) the MLT and (*b*) the IL at which the observations were made. The flux shown is that measured at the low-latitude edge of UWIs, where the flux maximizes. Linear fits to the data and the associated linear correlation coefficients are shown.

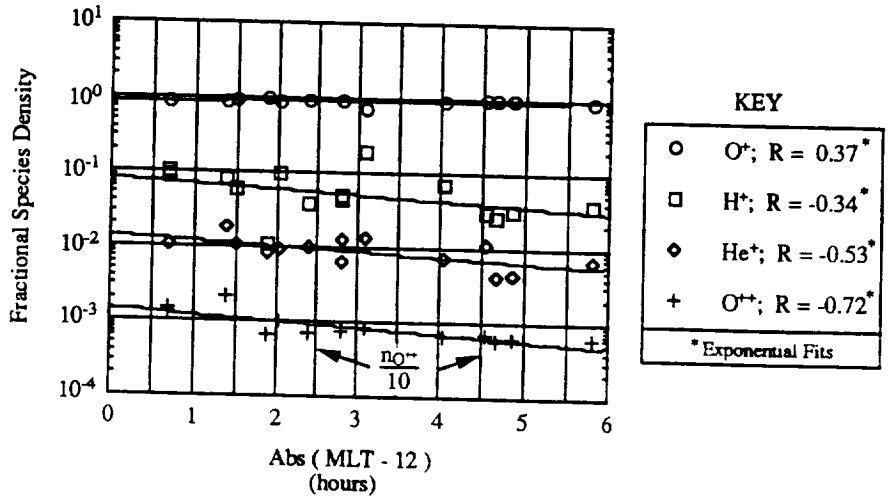

Fig. 7. The fractional densities of the species O^+ (open circles), H^+ (open squares), He^+ (open diamonds), and O^{++} (crosses) are displayed in scatter plot format versus the separation (in hours) from local magnetic noon at which the observations were made. The data for O^{++} have been divided by 10 to provide for a clearer display. The composition data are as determined during the minute within a given UWI when the upward O^+ flux maximizes, generally at the lower-latitude edge of the event.

As shown by *Lockwood et al.* [1985], the invariant latitude of the upwelling ion source region varies systematically with geomagnetic activity, moving to lower latitudes with increasing values of the 3-hour *Kp* index. The association of this upwelling source region with the geomagnetic polar cleft and its systematic latitudinal variation is further illustrated in Figure 8, where the invariant latitude at which the maximum upwelling O^+ flux occurs is plotted versus a measure of the interplanetary magnetic field (IMF) B_z component. The values of B_z plotted were obtained from hourly averages published by the National Space Science Data Center (NSSDC) World Data Center A for Rockets and Satellites. These data are a compilation based on IMP 8 and ISEE 3 observations. The plotted values represent weighted (and corrected for solar wind transit time) hourly averages of B_z during the hour immediately preceding the minute in UT during which the flux observation was obtained. For example, in the case of day 71 of 1982 the maximum O^+ flux was observed at 1934 hours UT. The value of B_z associated with that event is taken as

$$\langle B_z \rangle = \frac{34[B_{z(1900\text{–}2000)}] + 26(B_{z(1800\text{–}1900)})}{60} \quad (9)$$

where $B_{z(xxxx\text{–}yyyy)}$ was obtained from the World Data Center data base. We have indicated a least squares linear fit to the data, which yields a correlation coefficient of 0.72. We have also shown (dashed lines) the linear least squares results of *Carbary and Meng* [1986], giving the fitted locations of the poleward and equatorward cusp boundaries, based on DMSP F-2 and F-4 low-energy electron signatures, as functions of B_z (measured by the

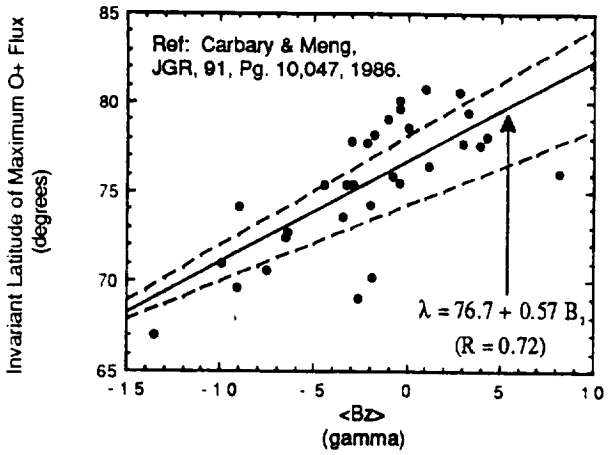

Fig. 8. A scatter plot of the latitude at which the upward O^+ flux maximizes within UWIs, versus the preceding hourly average of the IMF B_z component (corrected for solar wind transit time to the magnetopause). The solid line represents a linear least squares fit to the data. The two dashed lines show the locations of the upper- and lower-latitude edges of the cleftlike (see text) electron precipitation signatures as functions of B_z. These edges are as determined in the study of *Carbary and Meng* [1986].

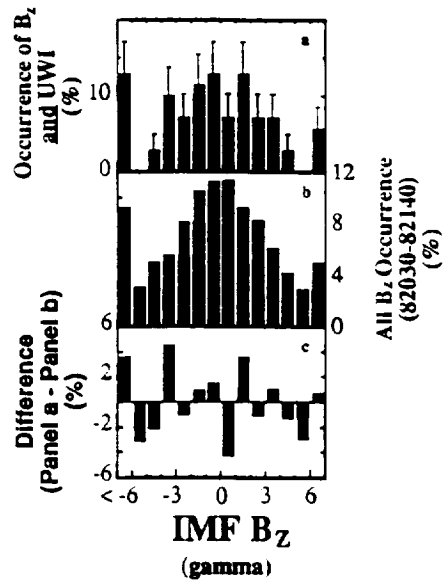

Fig. 9. The occurrence, during the period between days 36 and 268 of 1982, of various values of the IMF B_z component is studied, both in relationship with the occurrence of UWIs and independent of such occurrence. (*a*) The distribution of B_z values measured during the hour immediately preceding a RIMS UWI observation. (*b*) The distribution of B_z for all the available data, without regard to RIMS observations. (*c*) The difference between the data in Figures 9*a* and 9*b*. These differences should reveal any significant trend in the dependence of the occurrence of dayside ion upwelling upon B_z. All IMF data are corrected for solar wind transit time to the magnetopause.

IMP 8/GSFC (Goddard Space Flight Center) magnetometer). We note here that although *Carbary and Meng* [1986] use the word "cusp," the study they performed applies to a broader region (in MLT) which is more properly referred to as the "magnetospheric cleft" [*Carbary and Meng*, 1986, Figure 2; *Newell and Meng*, 1988]. The distinction is significant because the cusp, found within a region highly localized near noon MLT, as thought to connect to the dayside magnetopause, while the cleft, found within a broad region which stretches across the dayside, is associated with the low-latitude boundary layer. Although, as in the Carbary and Meng study, there is significant scatter in the data, Figure 8 unambiguously locates the upwelling ion source region within the magnetospheric polar cleft, as identified by the low-energy electron signature.

There does not, however, appear to exist a strong relationship between either the occurrence probability or intensity of upwelling ions and the averaged value of the IMF B_z during the hour immediately preceding the observation of ion upwelling in the RIMS data. In Figure 9, we study the occurrence of values of B_z as observed, both in conjunction with an UWI observation and regardless of UWI observation. All three panels in Figure 9 feature an abscissa which is composed of B_z values binned in 1 γ bins, from -6 γ to $+6$ γ, with the leftmost bin including all observations of B_z less than -6 γ and the rightmost bin those with B_z greater than or equal to $+6$ γ. There were a total of 70 observed UWI events for which the IMF data were available during both the present and previous hours, allowing the weighted average described in the previous paragraph to be performed. The value plotted along the ordinate of Figure 9*a* represents the percentage of those 70 events which were characterized by a weighted hourly average of B_z which fell within the given bin. The error bar is derived from the square root of the number of samples in the bin. For example, 9 ± 3 of the events were associated with a value of B_z of less than -6 γ, yielding $12.8 \pm 4.3\%$ of the 70 samples. In Figure 9*b* the occurrence of frequency of B_z values, for all available hourly IMF data during the same time period as in Figure 9*a* (days 36–268 of 1982), are plotted for comparison. The distribution in Figure 9*b* is peaked near $B_z = 0$ and falls off quite symmetrically to either side. The large occurrences in the extreme bins are a reflection of the larger bin size. Figure 9*c* displays the differences between the data in the above two panels, such that the plotted values are equal to those plotted in Figure 9*a*, less those plotted in Figure 9*b*. If the occurrence of UWI events were dependent upon B_z, we would expect to see that reflected most clearly in Figure 9*c*. If, for example, UWIs were more likely to occur for negative values of B_z, we would expect to see positive differences in Figure 9*c* for $B_z < 0$ and negative differences for $B_z > 0$. No such trend is evident, and we conclude from these data that UWI occurrence is not dependent upon the average value of B_z during the hour immediately preceding event observation.

A similar statement can be made regarding the dependence of upwelling O^+ intensity on the averaged B_z values, as illustrated using the scatter plot of Figure 10. Here we have plotted the maximum upwelling O^+ flux, normalized to 1000 km altitude, measured during a given event versus the hourly averaged value of B_z for the hour immediately preceding event observation. The linear correlation coefficient of -0.14 indicates no significant dependence among the parameters plotted. These results are somewhat surprising, in view of recent observations of *Lockwood et al.* [1988] which suggest that dayside ion upwelling may be a direct consequence of magnetic coupling at the subsolar magnetopause. Further study of the relationship of UWI events to interplanetary and magnetospheric conditions will be the subject of a future publication.

4.4. *Cleft Region Source Strength*

The upward ion flux levels discussed in the previous sections are not typical of the entire dayside auroral zone, but are representative of the most intense portions of the upwelling flows.

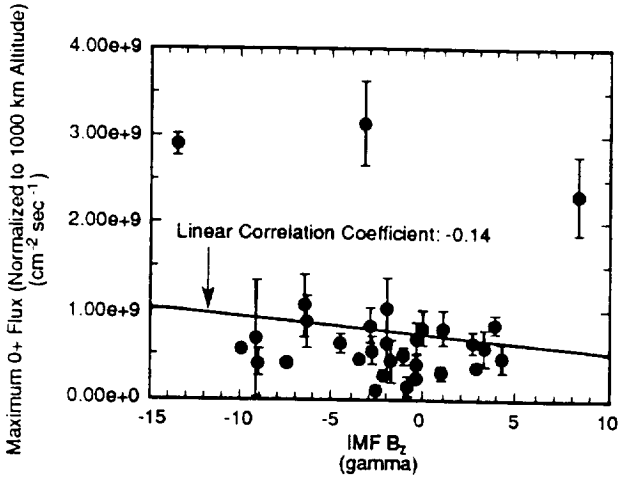

Fig. 10. Upwelling O^+ flux is displayed as a scatter plot versus the immediately preceding hourly averaged value of the IMF B_z component, corrected for solar wind transit time to the magnetopause. The flux values plotted are the maximum values measured within the UWIs and are normalized to a common altitude of 10^3 km. A linear fit to the data, as well as the resulting linear correlation coefficient, is indicated.

in the immediate vicinity of the source region. We have computed bulk parameters from regions downstream (generally poleward) of the source region as well. All the measured fluxes, as well as a measure of the occurrence frequency of dayside ion upwelling, need to be incorporated into any estimate of the total ion outflow from this ionospheric source. The expectation value for the upward particle flux at any location may be expressed as the product of the upward flux measured at that location at the time when an upwelling ion event is observed and the probability that an upwelling ion event will be observed at that location. We have binned our ion flux measurements in IL and MLT and combined them as a product with similarly binned values of the occurrence probabilities reported by *Lockwood et al.* [1985]. We have used 5° IL bins between 50° and 90° and 1-hour MLT bins from 0 to 24 hours. The mean flux in a given bin is taken as

$$\overline{J_{i,j}} = \frac{\sum_{n=1}^{N} J_{i,j,n}}{N} \tag{10}$$

where $J_{i,j,n}$ represents the nth of a total of N flux observations (normalized to 1000 km altitude) in the angular bin associated with the indices (i,j). The expectation value for the flux in the bin (i,j) is then given as

$$\langle J \rangle_{i,j} = (\overline{J_{i,j}}) \times (f^{u}_{i,j}) \tag{11}$$

where $f^{u}_{i,j}$ is the occurrence probability reported by *Lockwood et al.* [1985]. Expectation values computed in this manner are presented in Figure 11 for the species H^+, He^+, O^+, and O^{++}, where the value of $\log_{10}(\langle J \rangle_{i,j})$ is plotted in polar grey scale versus IL and MLT. The expectation values plotted in Figure 11 represent the closest estimate we can make at this time of the mean upwelling source strength for the various ion species shown. The outflowing source region may extend poleward of the region shown in Figure 11; however, such an extension is not identifiable within the context of the UWI signature identification on which this work is based. As in the case of the maximum event fluxes reported in previous sections, O^+ and H^+ show the most

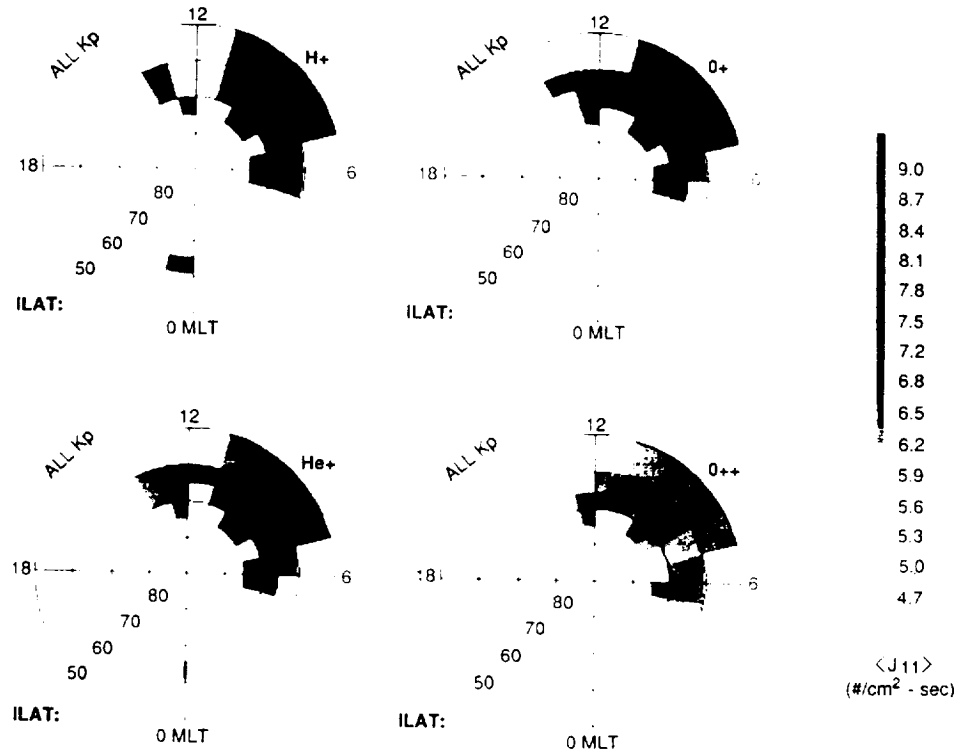

Fig. 11. The expectation value $\langle J_{\parallel} \rangle$ for the upward parallel flux is plotted for the ion species H^+, O^+, O^{++}, and He^+, in polar grey scale format versus IL and MLT. The flux in a given IL-MLT bin is derived as the product of the average flux measured in that bin within UWIs and the probability that an UWI will be observed within the bin.

intense outflows, followed by He^+ and O^{++}. In all cases, the source region is rather spatially structureless.

The fluxes shown in Figure 11 represent the ion flux expected at an altitude of 1000 km, having been scaled from the observation altitudes according to an $(r/r_0)^3$ dependence, where r and r_0 are the geocentric radii of the observation point and the 1000 km altitude surface, respectively. The total hemispheric particle outflow rate may be obtained by integrating over the distributions shown in Figure 11. To facilitate the integration, the fluxes are further scaled to the Earth's surface, where IL and the spherical magnetic latitude are equivalent. The total terrestrial outflow (I) from this dayside source region, for a given ion species, is then given as

$$I = 2 \int_H \langle \mathbf{J}(r,\lambda,\phi) \rangle \, d\mathbf{a}$$

$$= 2 R_E^2 \left(\frac{r_0}{R_E}\right)^3 \int_0^{2\pi} d\phi \int_0^{\pi} d\lambda \, \langle J_\parallel(r_0,\lambda,\phi) \rangle \qquad (12)$$

where we have approximated the geomagnetic field lines as radial and the factor of 2 accounts for source regions in each hemisphere. This integration has been numerically carried out over the distributions of fluxes shown in Figure 11. The resulting outflows are listed in Table 1. These numbers may underestimate the total outflow, since significant UWI outflows may occur poleward of regions identified as being within UWIs.

TABLE 1. The Total Rate $\langle J_\parallel \rangle$ at Which Ions Flow out of the Dayside Cleft Region

Ion Species	$\langle J_\parallel \rangle$, ions s^{-1}
H^+	5×10^{24}
He^+	9×10^{23}
O^{++}	2×10^{23}
O^+	2×10^{25}

Flows from both hemispheres are included.

The ion outflow is dominated by O^+, with 2×10^{25} ions s^{-1} emanating from the dayside cleft region. The H^+ source strength represents ~20% of the total outflow, while the minor species (O^{++} and He^+) are at the several percent level or less. These results are to be compared with those of *Yau et al.* [1985] who studied major ion outflows at energies such that 10 V ≤ E/q ≤ 17 kV. They reported extensively on outflows at latitudes including the auroral zone and polar cap, distinguishing among flow levels on the basis of geomagnetic activity, MLT/IL regime, and solar cycle. Many of the results of *Yau et al.* [1985] are summarized in their Table 1. They found the total net auroral zone ion outflow to lie between 2×10^{25} and 4×10^{25} ions s^{-1} for H^+ and between 1×10^{25} and 8×10^{25} for O^+, depending on geomagnetic activity and solar cycle. In our Table 1, we show a total UWI O^+ outflow of 2×10^{25} ions s^{-1}. This is of the same order as that reported by Yau et al. during geomagnetically quiet times. On the other hand, our results show a total H^+ outflow of 5×10^{24} ions s^{-1}, a factor of 5 smaller than that reported by Yau et al. during geomagnetically quiet times. We believe these figures apply to ions with energies less than or of the order of 10 eV/q. This is based on both the published work of *Moore et al.* [1986*b*] and on other, unpublished work, which show typical ion thermal energies within these events of 5 – 10 eV/q. The flux levels in the current study are representative of a wide range of geomagnetic activity. The available data do not permit breaking down the global UWI outflow according to geomagnetic activity. It appears, especially in the case of the O^+, that the UWI source represents a substantial fraction of the total global ion outflow.

5. Conclusions

With the data presented in the sections above we have reported the bulk properties of the upwelling ion plasma in the dayside cleft region. We have quantified the distribution of ion species density, upward bulk velocity, and flux within the cleft source region. Additionally, we have combined the bulk flow results from a number of these events with the occurrence probabilities obtained by *Lockwood et al.* [1985] to give reliable estimates of the source strength distribution as a function of MLT and IL. Finally, we have presented a measure of the total cleft region source strength in terms of the number of ions per second to flow away from the ionosphere. The following specific conclusions may be drawn from the work presented above.

1. All observed ion species are seen to participate in the ion upwelling. Within a given event, the upward flux typically maximizes near the low-latitude edge of the outflow. At that location, typical ion species densities, upward field-aligned bulk velocities, and upward field-aligned fluxes (mapped to a common altitude of 1000 km) are summarized in Table 2. The distributions about these typical values have been presented in Figure 4.

TABLE 2. Typical Ion Bulk Parameters as Measured Within, but Near the Lower-Latitude Edge of Upwelling Ion Events

Species Bulk Parameter	O^+	H^+	He^+	O^{++}
n, cm^{-3}	600	50	15	7
$v_\parallel$, km s^{-1}	3	16	7	4
$J_\parallel$,* particles cm^{-2} s^{-1}	6×10^8	2×10^8	10^7	6×10^6

*Scaled to a common altitude of 1000 km.

2. There is a systematic dependence of the upward field-aligned ion bulk velocity upon the species charge-to-mass ratio, with the velocity increasing approximately with the square root of q/m. This dependence is illustrated in Figure 5.

3. The intensity of UWIs, as measured by the maximum upward O^+ flux observed within an event, does not show significant systematic variation as a function of MLT or IL. This is indicative of a rather uniform outflow from the dayside cleft region. This point is illustrated in Figure 6, where scatter plots of the maximum normalized O^+ flux versus MLT and IL are presented. The point is further illustrated, with respect to all measured flux values for the species H^+, He^+, O^+, and O^{++}, in Figure 11, where the expectation value of the normalized upward flux is shown plotted in polar form.

4. The ion density composition of the outflow shows a weak dependence upon MLT, however, with minor species, particularly O^{++}, representing a larger fractional composition near magnetic local noon. This point is illustrated in Figure 7.

5. The statistical association of UWIs with the dayside magnetospheric cleft, as identified by low-energy electron signatures [*Carbary and Meng*, 1986], is illustrated in Figure 8. This association points up the likelihood of a relationship between the phenomenon of dayside ion upwelling and the solar wind-magnetosphere interaction.

6. There is, however, no clear-cut relationship between either the occurrence or intensity of UWIs and the immediately preceding hourly averaged value of the IMF B_z component. These facts are illustrated in Figures 9 and 10, respectively. As the simplest

measure of the degree of electromagnetic coupling between the magnetosphere and solar wind, one might expect to find increased occurrence or intensity of UWIs with increasingly negative B_z if, for example, UWIs were directly associated with variable aspects of the large-scale auroral convection morphology or with the occurrence of magnetopause flux transfer events, both of which depend upon B_z. The results presented here indicate that neither is the case.

7. Our estimate of the ion outflow rates (including both hemispheres) from this dayside cleft source have been presented in Table 1. These estimates are given based on data collected between days 36 and 137 of 1982, and almost all were from northern hemisphere passes. Thus, they are generally representative of spring conditions during an active portion of the solar cycle. Virtually all levels of geomagnetic activity are represented. In the case of O^+ and H^+, these numbers validate the cleft ion fountain contributions used by *Chappell et al.* [1987] and *Delcourt et al.* [1989] in demonstrating the significance of the ionosphere as a magnetospheric plasma source.

Acknowledgements. The authors are grateful to the RIMS team at Marshall Space Flight Center (MSFC) and the programming staff of Boeing Corporation for assistance with the data reduction software. We would also like to thank the National Space Science Data Center (NSSDC) for providing the interplanetary magnetic field data. Support for C. J. Pollock came from the National Research Council, under their Resident Research Associateship program.

The Editor thanks M. Lockwood and A. W. Yau for their assistance in evaluating this paper.

REFERENCES

Balsiger, H., P. Eberhardt, J. Geiss, and D. T. Young, Magnetic storm injection of 0.9- to 16-keV/e solar and terrestrial ions into the high-altitude magnetosphere, *J. Geophys. Res.*, *85*, 1645–1662, 1980.

Carbary, J. F., and C. I. Meng, Correlation of cusp latitude with B_z and AE (12) using nearly one year's data, *J. Geophys. Res.*, *91*, 10,047–10,054, 1986.

Chandler, M. O., and C. R. Chappell, Observations of the flow of H^+ and He^+ along magnetic field lines in the plasmasphere, *J. Geophys. Res.*, *91*, 8847–8860, 1986.

Chappell, C. R., S. A. Fields, C. R. Baugher, J. H. Hoffman, W. B. Hanson, W. W. Wright, and H. D. Hammack, The retarding ion mass spectrometer on Dynamics Explorer A, *Space Sci. Instrum.*, *5*, 477–491, 1981.

Chappell, C. R., T. E. Moore, and J. H. Waite, Jr., The ionosphere as a fully adequate source of plasma for the Earth's magnetosphere, *J. Geophys. Res.*, *92*, 5896–5910, 1987.

Collin, H. L., R. D. Sharp, and E. G. Shelley, The magnitude and composition of the outflow of energetic ions from the ionosphere, *J. Geophys. Res.*, *89*, 2185–2194, 1984.

Delcourt, D. C., C. R. Chappell, T. E. Moore, and J. H. Waite, Jr., A three-dimensional numerical model of ionospheric plasma in the magnetosphere, *J. Geophys. Res.*, *94*, 11,893–11,920, 1989.

Eastman, T. E., L. A. Frank, W. K. Peterson, and W. Lennartsson, The plasma sheet boundary layer, *J. Geophys. Res.*, *89*, 1553–1572, 1984.

Ghielmetti, A. G., R. G. Johnson, R. D. Sharp, and E. G. Shelley, The latitudinal, diurnal, and altitudinal distributions of upward flowing energetic ions of ionospheric origin, *Geophys. Res. Lett.*, *5*, 59–62, 1978.

Gorney, D. J., A. Clarke, D. Croley, J. Fennell, J. Luhmann, and P. Mizera, The distribution of ion beams and conics below 8000 km, *J. Geophys. Res.*, *86*, 83–89, 1981.

Hoffman, R. A., and E. R. Schmerling, Dynamics Explorer program: An overview, *Space Sci. Instrum.*, *5*, 345–348, 1981.

Johnson, R. G., Energetic ion composition in the Earth's magnetosphere, *Rev. Geophys.*, *17*, 696–705, 1979.

Johnson, R. G., R. D. Sharp, and E. G. Shelley, Observations of ions of ionospheric origin in the storm-time ring current, *Geophys. Res. Lett.*, *4*, 403–406, 1977.

Kintner, P. M., W. Scales, J. Vago, R. Arnoldy, G. Garbe, and T. Moore, Simultaneous observations of electrostatic oxygen cyclotron waves and ion conics, *Geophys. Res. Lett.*, *16*, 739–742, 1989.

Klumpar, D. M., Transversely accelerated ions: An ionospheric source of hot magnetospheric ions, *J. Geophys. Res.*, *84*, 4229–4237, 1979.

Lennartsson, W., and E. G. Shelley, Survey of 0.1- to 16-keV/e plasma sheet ion composition, *J. Geophys. Res.*, *91*, 3061–3076, 1986.

Lockwood, M., J. H. Waite, Jr., T. E. Moore, J. F. E. Johnson, and C. R. Chappell, A new source of suprathermal O^+ ions near the dayside polar cap boundary, *J. Geophys. Res.*, *90*, 4099–4116, 1985.

Lockwood, M., M. F. Smith, C. J. Farrugia, and G. L. Siscoe, Ionospheric ion upwelling in the wake of flux transfer events at the dayside magnetopause, *J. Geophys. Res.*, *93*, 5641–5654, 1988.

Lundin, R., B. Hultqvist, E. Dubinin, A. Zackarov, and N. Pissarenko, Observations of outflowing ion beams on auroral field lines at altitudes of many earth radii, *Planet. Space Sci.*, *30*, 715–726, 1982.

Moore, T. E., C. J. Pollock, R. L. Arnoldy, and P. M. Kintner, Preferential O^+ heating in the topside ionosphere, *Geophys. Res. Lett.*, *13*, 901–904, 1986*a*.

Moore, T. E., M. Lockwood, M. O. Chandler, J. H. Waite, Jr., C. R. Chappell, A. Persoon, and M. Sugiura, Upwelling O^+ ion source characteristics, *J. Geophys. Res.*, *91*, 7019–7031, 1986*b*.

Newell, P. T., and C. I. Meng, The cusp and the cleft/boundary layer: Low-altitude identification and statistical local time variation, *J. Geophys. Res.*, *93*, 14,549–14,556, 1988.

Persoon, A. M., D. A. Gurnett, and S. D. Shawhan, Polar cap electron densities from DE 1 plasma wave observations, *J. Geophys. Res.*, *88*, 10,123–10,136, 1983.

Peterson, W. K., R. D. Sharp, E. G. Shelley, R. G. Johnson, and H. Balsiger, Energetic ion composition of the plasma sheet, *J. Geophys. Res.*, *86*, 761–767, 1981.

Schunk, R. W., and J. J. Sojka, A three-dimensional time-dependent model of the polar wind, *J. Geophys. Res.*, *94*, 8973–8991, 1989.

Sharp, R. D., R. G. Johnson, and E. G. Shelley, Observations of an ionospheric acceleration mechanism producing energetic (keV) ions primarily normal to the geomagnetic field direction, *J. Geophys. Res.*, *82*, 3324–3328, 1977.

Shawhan, S. D., D. A. Gurnett, D. L. Odem, R. A. Helliwell, and C. G. Park, The plasma wave and quasi-static electric field instrument (PWI) for Dynamics Explorer-A, *Space Sci. Instrum.*, *5*, 535–550, 1981.

Shelley, E. G., R. G. Johnson, and R. D. Sharp, Satellite observations of energetic heavy ions during a geomagnetic storm, *J. Geophys. Res.*, *77*, 6104–6110, 1972.

Waite, J. H. Jr., T. Nagai, J. F. E. Johnson, C. R. Chappell, J. L. Burch, T. L. Killeen, P. B. Hays, G. R. Carignan, W. K. Peterson, and E. G. Shelley, Escape of suprathermal O^+ ions in the polar cap, *J. Geophys. Res.*, *90*, 1619–1630, 1985.

Waite, J. H. Jr., T. E. Moore, M. O. Chandler, M. Lockwood, A. Persoon, and M. Sugiura, Ion energization in upwelling ion events, in *Ion Acceleration in the Magnetosphere and Ionosphere*, *Geophys. Monogr. Ser.*, vol. 38, edited by T. Chang, pp. 61–66, AGU, Washington, D. C., 1986.

Whalen, B. A., W. Bernstein, and P. W. Daly, Low altitude acceleration of ionospheric ions, *Geophys. Res. Lett.*, *5*, 55–58, 1978.

Yau, A. W., B. A. Whalen, A. G. McNamara, P. J. Kellogg, and W. Bernstein, Particle and wave observations of low-altitude ionospheric ion acceleration events, *J. Geophys. Res.*, *88*, 341–355, 1983.

Yau, A. W., B. A. Whalen, W. K. Peterson, and E. G. Shelley, Distribution of upflowing ionospheric ions in the high-altitude polar cap and auroral ionosphere, *J. Geophys. Res.*, *89*, 5507–5522, 1984.

Yau, A. W., E. G. Shelley, W. K. Peterson, and L. Lenchyshyn, Energetic auroral and polar ion outflow at DE 1 altitudes: Magnitude, composition, magnetic activity dependence, and long-term variations, *J. Geophys. Res.*, *90*, 8417–8432, 1985.

Young, D. T., F. Geiss, H. Balsiger, P. Eberhardt, A. Ghielmetti, and H. Rosenbauer, Discovery of the He^{2+} and O^{2+} ions of terrestrial origin in the outer magnetosphere, *Geophys. Res. Lett.*, *4*, 561–564, 1977.

M. O. Chandler, C. R. Chappell, T. E. Moore, and C. J. Pollock, Space Science Laboratory, NASA, Marshall Space Flight Center, AL 35812.

D. A. Gurnett, Department of Physics and Astronomy, University of Iowa, Iowa City, IA 52242.

J. H. Waite, Jr., Department of Space Physics, Southwest Research Institute, 3500 Culebra Road, San Antonio, TX 78284.

(Received January 2, 1990;
revised April 20, 1990;
accepted May 8, 1990.)

JOURNAL OF GEOPHYSICAL RESEARCH, VOL. 99, NO. A9, PAGES 17,483–17,501, SEPTEMBER 1, 1994

Statistical survey of pitch angle distributions in core (0-50 eV) ions from Dynamics Explorer 1: Outflow in the auroral zone, polar cap, and cusp

B. L. Giles,[1] C. R. Chappell,[2] T. E. Moore,[1] R. H. Comfort,[3] and J. H. Waite Jr.[4]

Abstract. Core (0-50 eV) ion pitch angle measurements from the retarding ion mass spectrometer on Dynamics Explorer 1 are examined with respect to magnetic disturbance, invariant latitude, magnetic local time, and altitude for ions H^+, He^+, O^+, M/Z=2 (D^+ or He^{++}), and O^{++}. Included are outflow events in the auroral zone, polar cap, and cusp, separated into altitude regions below and above 3 R_E. In addition to the customary division into beam, conic, and upwelling distributions, the high-latitude observations fall into three categories corresponding to ion bulk speeds that are (1) less than, (2) comparable to, or (3) faster than that of the spacecraft. This separation, along with the altitude partition, serves to identify conditions under which ionospheric source ions are gravitationally bound and when they are more energetic and able to escape to the outer magnetosphere. Features of the cleft ion fountain inferred from single event studies are clearly identifiable in the statistical results. In addition, it is found that the dayside pre-noon cleft is a consistent source of escape velocity low-energy ions regardless of species or activity level and the dayside afternoon cleft, or auroral zone, becomes an additional source for increased activity. The auroral oval as a whole appears to be a steady source of escape velocity H^+, a steady source of escape velocity He^+ ions for the dusk sector, and a source of escape velocity heavy ions for dusk local times primarily during increased activity. The polar cap above the auroral zone is a consistent source of low-energy ions, although only the lighter mass particles appear to have sufficient velocity, on average, to escape to higher altitudes. The observations support two concepts for outflow: (1) The cleft ion fountain consists of ionospheric plasma of 1-20 eV energy streaming upward into the magnetosphere where high-latitude convection electric fields cause poleward dispersion. (2) The auroral ion fountain involves field-aligned beams which flow out along auroral latitude field lines; and, in addition, for late afternoon local times, they experience additional acceleration such that the ion energy distribution tends to exceed the detection range of the instrument (>50-60 eV).

1. Introduction

At polar latitudes, because the Earth's dipole field is nearly vertical, charged particles in the ionosphere created by photoionization or particle impact ionization are relatively free to move upward along the magnetic field lines and populate higher-altitude regions of the magnetosphere. Since the discovery of energetic O^+ ions by *Shelley et al.* [1972], ion composition measurements have revealed that a significant amount of plasma in the Earth's magnetosphere is of ionospheric origin [e.g., *Chappell et al.*, 1987; *Moore et al.*, 1989; *Moore*, 1991]. The importance of this terrestrial source is confirmed by the presence of energized ionospheric ions throughout the magnetosphere, such as the ring current and plasma sheet [*Johnson et al.*, 1977; *Geiss et al.*, 1978; *Lennartsson et al.*, 1979; *Balsiger et al.*, 1980; *Lundin et al.*; 1980, *Peterson et al.*, 1981; *Sharp et al.*, 1982; *Eastman et al.*, 1984; *Lennartsson and Shelley*, 1986], the magnetopause and magnetosheath region [*Peterson et al.*, 1982; *Hultqvist*, 1983], the magnetotail lobes [*Sharp et al.*, 1981], and the plasma mantle and magnetotail boundary layer [*Frank et al.*, 1977; *Hardy et al.*, 1977; *Lundin et al.*, 1982a, b; *Candidi et al.*, 1982]. In addition, it has been shown that a significant portion of these ionospheric-source ions have energies below 1 keV [*Yau et al.*, 1984; *Giles et al.*, 1988; *Delcourt et al.*, 1988]. These lower-energy particles are very sensitive to small fluctuations in local magnetic and electric fields. They interact with charge carriers for magnetospheric and ionospheric currents and operate as a permeating medium in which plasma waves are generated and propagated to other parts of the magnetosphere thereby influencing larger-scale interactions. Thus information about the dynamics of this plasma component is an effective tracer for broader scale magnetospheric processes.

In understanding the transport and dynamics of charged particles, information about the particle pitch angle distribution (PAD), the arrangement of directional flux with respect the local magnetic field direction, is an invaluable aid. For example, case studies by *Sharp et al.* [1977, 1979] exploited field-aligned pitch angle distributions to infer the presence, and

[1]Space Sciences Laboratory, NASA Marshall Space Flight Center, Huntsville, Alabama.
[2]NASA Marshall Space Flight Center, Huntsville, Alabama.
[3]Department of Physics and Center for Space Plasma and Aeronomic Research, University of Alabama, Huntsville.
[4]Southwest Research Institute, San Antonio, Texas.

Paper number 94JA00864.
0148-0227/94/94JA-00864$05.00

vertical extent of, parallel potential drops within an auroral acceleration region. Also, occurrence statistics of distinct PAD classifications have been used to examine possible plasma source locations, acceleration regions, and the subsequent evolution of plasma distributions during transport [e.g., *Nagai et al.*, 1983; *Yau et al.*, 1984]. The lowest-energy ions, in particular, have been shown to exhibit complex pitch angle characteristics such as field-aligned beams, conics, and trapped (pancake) distributions [*Chappell*, 1982; *Chappell et al.*, 1982a].

The retarding ion mass spectrometer (RIMS) experiment on Dynamics Explorer 1 (DE 1) represents a major effort to thoroughly characterize the lowest-energy plasma component by measuring ions ranging from 0 eV (or spacecraft potential) up to 50 eV throughout almost the entire volume of the inner magnetosphere, from the topside ionosphere out to 4.67 R_E. The RIMS effort has, in its lifetime, revealed previously unobserved ionospheric plasma sources to the magnetosphere and called into question accepted theories concerning the relative contributions of the internal and external sources to magnetospheric plasma content. Specific to the RIMS instrument are observations of the supersonic polar wind [*Nagai et al.*, 1984], a source of low-energy heavy ions from the polar cap and the cleft region [*Waite et al.*, 1985; *Lockwood et al.*, 1985a, b], upward fluxes of N^+, N^{++} [*Chappell et al.*, 1982b] and of molecular ions N_2^+, NO^+, and O_2^+ [*Craven et al.*, 1985]. It is this data set that will be used to obtain pitch angle distributions of the individual charged particle species.

One of the most intriguing topics in magnetospheric physics research that will be addressed is the question regarding the source of particles populating the inner magnetosphere. Concentrations and relative dynamic behaviors of H^+, He^{++}, and O^+ are commonly used as indicators of a solar wind or ionospheric source. The RIMS mass spectrometer is capable of resolving several mass peaks, including H^+, He^+, O^+, O^{++}, and one at a charge-to-mass ratio of 2. Because RIMS provides no direct information on charge state, these latter measurements could conceivably be H_2^+, He^{++}, or D^+. *Breig et al.* [1987] and *Breig and Hanson* [1991] have reported on deuterium ion flows in the thermosphere. In this case the instrument is a predecessor of RIMS which again, yields the M/Z=2 mass peak with no charge information, but additional correlative evidence with H^+ determines these samples to be D^+. *Young et al.* [1977, 1982] and *Comfort et al.* [1988] report observations in the relatively cold outer plasmasphere that are most likely terrestrial source He^{++}. In the present work, because the DE 1 orbit samples low altitudes where D^+ measurements are likely and samples higher altitudes where low-energy He^{++} measurements are possible, the RIMS measurements will be referred to as being of the M/Z=2 ion. It is thought, because of the RIMS energy range, that any He^{++} measurements would represent doubly-ionized helium produced in the ionosphere or plasmasphere, not cooled solar wind He^{++}. Regardless though, of whether the M/Z=2 measurements are representative of He^{++} or D^+, the key issue is whether evidence exists for these ions, and of H^+, He^+, O^+, and O^{++}, to have an ionospheric source and then flow outward, such that they populate both inner and outer portions of the magnetosphere.

In section 2 we describe the RIMS instrument and the DE orbit, and outline the pattern recognition technique used. Section 3 describes the classification of the data in terms of pitch angle distributions and details the consequences of observing low-energy particles with a moving spacecraft. Section 4 contains occurrence probability data with respect to magnetic disturbance, invariant latitude, magnetic local time (MLT), and geocentric altitude for invariant latitudes above 60°. Section 5 discusses these data in relation to the transport and dynamics of plasma in the Earth's inner magnetosphere. Section 6 is a summary. A paper (Giles et al., Statistical survey of pitch angle distributions in core (0-50 eV) ions from Dynamics Explorer 1: Map of the magnetosphere's low-energy ion component, unpublished manuscript, 1994) presents statistics for invariant latitudes below 60°, examining trends with disturbance, magnetic latitude, MLT and L shell.

2. Instrumentation and Data Analysis Considerations

The survey covers the ions routinely measured by the DE 1/RIMS instrument (H^+, He^+, O^+, M/Z=2, and O^{++}) in the energy range 0-50 eV. The observed count rates for each ion were classified according to their pitch angle distribution as determined from the radial sensor head of the instrument as it rotated through a full range of pitch angles in each 6-s satellite spin period. As the spacecraft spins, the radial head (mounted perpendicular to the spin axis) responds to ion fluxes for nearly the full range of angles (-180° to +180°) with respect to the spacecraft ram direction. With knowledge of the Earth's magnetic field in relation to spacecraft ram, the RIMS spin angle response corresponds closely to a pitch angle distribution (detailed in section 3). The instrument and its operational characteristics are described by *Chappell et al.* [1981], *Fields et al.* [1982], and *Olsen et al.* [1985].

The elliptical polar orbit has perigee of 675-km altitude and apogee of 24,875-km altitude. The motion of the Earth around the Sun causes the orbit plane to drift westward at a rate of 1 hour MLT every 15.4 days (covering 24 hours in 12 months); the orbit line of apsides drifts 0.328° geographic latitude each day (moving from one pole to the other in 18 months). All available data, from October 19, 1981, to December 31, 1984 (a full precession/rotation cycle), are used to provide nearly complete local time and latitudinal coverage out to 4.67 R_E. However, the 3 to 1 ratio between the drift of the line of apsides and the westward drift of the orbit plane does result in specific areas of poor sampling in local time for a given altitude. For example, in the 0 to 6 MLT sector, midaltitudes in the auroral latitude regions are not well sampled. In addition to regions not reached by the orbit, the instrument is not always operated down to the DE 1 perigee of 675 km. At low altitudes the plasma density can be quite high and the instrument often enters a shutoff mode to protect the particle-detecting channeltrons from excessive count rates.

The instrument operational modes allowed programmed sampling of the mass range such that the major masses were sampled more frequently and constitute a larger portion of the database. Table 1 lists the number of 1-min spin angle distribution samples for each species above 60° invariant latitude (ILAT) in four MLT quadrants and two geocentric distance levels. Over 500,000 samples were obtained for the H^+, He^+, and O^+ ions and over 400,000 samples for the M/Z=2 and O^{++} ions. Because of the varying sample rate, the statistical calculations are carried out for each ion species separately; the probabilities presented are characteristic of the population of individual ion species, not of the ion population as a whole. Fifty-eight percent of the data were obtained during periods of relatively low activity ($Kp \leq 3$) and 42% during high activity ($Kp > 3$).

Table 1. Numbers of 1-min Pitch Angle Distribution Samples for H^+, He^+, O^+, $M/Z=2$, and O^{++}

	H^+		He^+		O^+		$M/Z=2$		O^{++}	
Local Time	$1<R_E<3$	$3<R_E<5$	$1<R_E<3$	$3<R_E<5$	$1<R_E<3$	$3<R_E<5$	$1<R_E<3$	$3<R_E<5$	$1<R_E<3$	$3<R_E<5$
0 to 6	8,387	122,203	8,533	123,370	7,495	112,735	5,596	74,726	5,591	74,729
6 to 12	10,167	148,543	10,328	150,109	9,433	139,414	6,804	104,465	6,801	104,464
12 to 18	28,230	116,300	28,684	118,276	25,704	108,569	20,222	84,867	20,219	84,870
18 to 24	31,234	120,432	31,671	122,108	29,793	119,895	22,352	88,057	22,351	88,061
Total samples		585,496		593,079		553,038		407,089		407,086

It should be noted that, for the 0 to 50 eV energy range, floating spacecraft potentials can prevent the detection of the lowest-energy ions. The RIMS team dealt with this spacecraft charging by the addition of a biasable voltage plate at the entrance aperture programmable to 0, -2 -4, or -8 V relative to the spacecraft potential. The present data set includes all available data, regardless of aperture bias setting. It is possible that the data set does not include particles with ram energy-per-charge less than the potential of the spacecraft.

For each ion the raw RIMS data are read and the counts-per-accumulation period (12 ms) are averaged over the time resolution period for each spin angle bin. For this study, 1-min time averages with 5° spin angle bins were chosen. This 5° spin angle bin refers to the center of the view cone and does not imply 5° resolution in the measurements. A subroutine scans the counts-versus-spin-phase-angle array to identify and characterize, in terms of centroids, widths, and skews, local maxima in the distribution with respect to the magnetic field direction. Next, a filtering pattern recognition routine produces the spin angle distribution description for each minute of RIMS data. When combined with orbit parameters and magnetic activity indices, this is the source for statistical analysis. Further description of the data analysis may be found in the work by *Giles* [1993].

The relations used to calculate the centroid and coefficient of skewness, taken from *Beyer* [1984], apply to discrete data grouped into a distribution having spin angle bin classifications θ_i, $i = 1, 2, ..., k$, and corresponding measurement values (in this case, instrument count rate per spin angle bin), $f(\theta_i)$, $i = 1, 2, ..., k$. The centroid is an arithmetic mean given by

$$C_m = \frac{\sum_{i=1}^{k} f(\theta^*)\theta^* \delta\theta}{\sum_{i=1}^{k} f(\theta^*)\delta\theta} \quad (1)$$

where

$$\theta^* = \frac{1}{2}(\theta_i + \theta_{i+1}) \quad (2)$$

$$f(\theta^*) = \frac{1}{2}\left(f(\theta_i) + f(\theta_{i+1})\right) \quad (3)$$

$$\delta\theta = (\theta_{i+1} - \theta_i) \quad (4)$$

The coefficient of skewness is given by

$$\alpha_3 = \frac{M_3}{(M_2)^{\frac{3}{2}}} \quad (5)$$

where M_2 and M_3 are the second and third moments about the mean of the sample. The rth moment about the mean, M_r, is given by

$$M_r = \frac{1}{n}\sum_{i=1}^{k} f(\theta^*)(\theta^* - C_m)^r \quad (6)$$

3. Classification of Spin Angle Data in Terms of Pitch Angle Distributions

3.1. Relationship to Pitch Angle Distributions

Strictly speaking, spacecraft spin angle distributions observed in situ are not true pitch angle distributions as customarily defined. The measured spin angle is defined in the reference frame of the spacecraft, which is different from the plasma rest frame due to spacecraft motion (2 to 8 km s^{-1}, depending on spacecraft altitude). This difference in reference frame is of little consequence provided the thermal speed, $(2\ kT/M)^{1/2}$, of the plasma is large compared to the spacecraft "ram" speed. For an average spacecraft speed of 5 km s^{-1} a factor-of-5 ratio of thermal speed to spacecraft speed requires 3.5 eV for H^+, 13 eV for He^+, and 52 eV for O^+.

Because RIMS responds to ions with energies considerably below this threshold, the RIMS spin angle data contain information about both the angular distribution of the plasma in its own frame of reference (the conventional pitch angle distribution) and the drift motion of the plasma relative to the spacecraft. These two aspects of instrument response tend to dominate independently – one at times obscuring the other – depending on the plasma's thermal speed and its relation to the spacecraft and plasma drift speed. Figure 1 illustrates the extremes of this motional influence.

Figure 1 shows simulated RIMS spin angle responses to a bi-Maxwellian plasma distribution ($T_\perp/T_\parallel = 5$) for four combinations of plasma thermal and drift speeds. The simulation adopts a numerical quadrature approach to the solution of the response integral, using a sum over aperture area, solid angle, and energy and weighted with the appropriate instrument response factor to obtain the correct energy-angle dependent relationship between detector count rate and directional flux. The parameters illustrating the limits of response were chosen for ease of understanding but without strict adherence to physical likehood in any given region of the polar ionosphere. In each case the spacecraft speed is set at 5 km s^{-1} perpendicular to **B**. Shown beside each spin angle plot are two phase-space schematic diagrams to clarify the orientation of the various spacecraft and plasma components. Both display velocity space, one in the spacecraft reference frame, the other in the frame of reference of the plasma.

In Figure 1a the H^+ ions have the perpendicular thermal

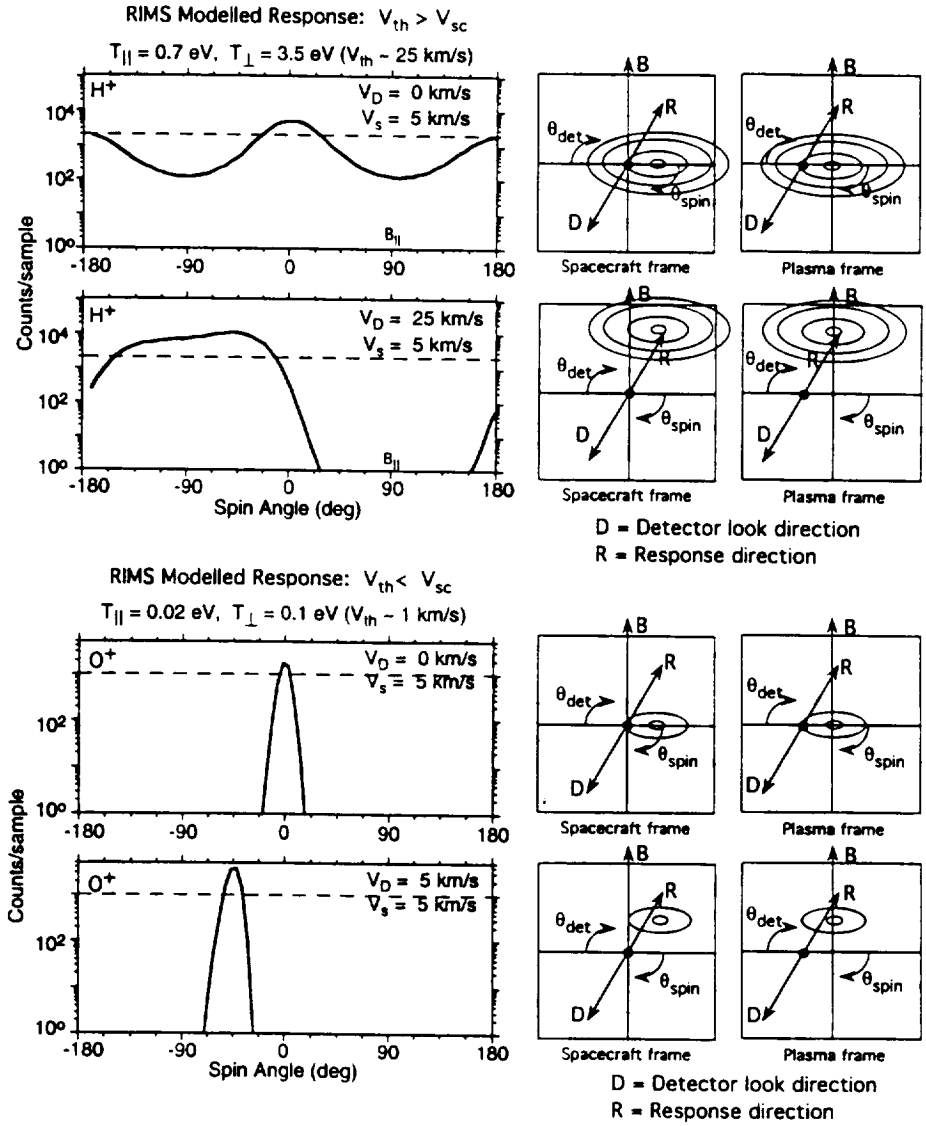

Figure 1. Simulated retarding ion mass spectrometer (RIMS) spin angle responses to bi-Maxwellian plasma distributions ($T_{\perp}/T_{||} = 5$). Also shown are phase space diagrams, drawn schematically, locating the various spacecraft and plasma components. Note that instrument response is to ions with velocities anti-parallel to the detector look direction. (a) H^+ ions with perpendicular thermal speed component greater than spacecraft speed by a factor of 5. The top panel assumes a stationary plasma and the bottom panel assumes V_D = 25 km s^{-1}, parallel to **B**. (b) O^+ ions with perpendicular thermal speed a factor of 5 below the spacecraft speed and with same drift speed assumptions as Figure 1a. For plasmas with thermal speeds smaller than the spacecraft and drift speeds, relative drift motion dominates the response. For plasmas with thermal speeds larger than the spacecraft and drift speeds, the true plasma frame distribution function emerges.

speed component greater than the spacecraft speed by a factor of 5 (V_{th} ~ 25 km s^{-1} and V_{sc} = 5 km s^{-1}). In the top panel the RIMS response is to a stationary plasma (drift speed V_D = 0); the angular characteristics of the distribution are clearly visible as peaks in the spin angle directions perpendicular to the magnetic field (0° and 180°). The relative motion of the spacecraft (5 km s^{-1} with respect to the stationary plasma) appears as an elevation in count rate in the direction of spacecraft motion (0°). The bottom panel assumes V_D = 25 km s^{-1}, parallel to **B**. In this case, bulk drift speed comparable to thermal speed, the angular characteristics of the distribution have become nearly unresolvable although the additional drift speed of the distribution may be identified by the shift from ram in the direction corresponding to an addition of the spacecraft and drift velocity vectors. (Without regard to the relationship of V_{th} to V_{sc}, simulation of the instrument response shows that angular features are resolvable for $T_{\perp}/T_{||}$ ratios greater than ~1.5).

In Figure 1b the response is for a bi-Maxwellian distribution of O^+ ions with perpendicular thermal speed a factor of 5 below the spacecraft speed (V_{th} ~1 km s^{-1} and V_{sc} = 5 km s^{-1}). In the upper panel, even though V_D = 0, the angular characteristics of the bi-Maxwellian are not resolvable within the detection thresholds of the instrument and the distribution appears as a single peak at the spacecraft ram direction. The bottom panel assumes V_D = 5 km s^{-1} parallel to **B**, the additional

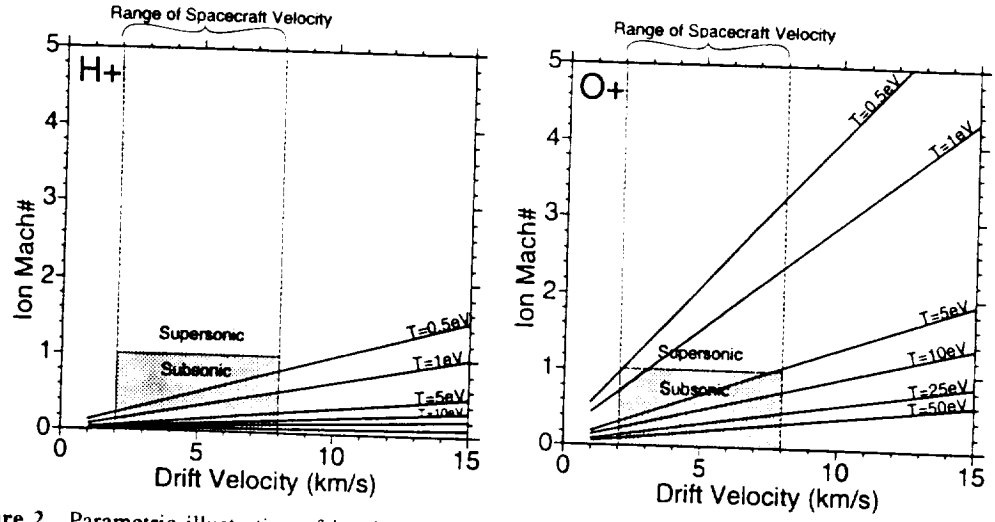

Figure 2. Parametric illustration of ion Mach number for drift and thermal components relevant to RIMS. It is for subsonic (thermal speed greater than drift speed) ion Mach numbers that the angular characteristics of the distribution will be resolvable. The shaded region delineates the range of spacecraft velocity with altitude (~7.6 km s^{-1} at 1.5 R_E geocentric, ~4.2 km s^{-1} at 3 R_E, and ~2.3 km s^{-1} at 4.5 R_E) and therefore the ion Mach range for a discernible relative drift motion effect to the spin angle measurements (i.e., not dominated by the angular response). For light ions with thermal energies below ~0.4 eV the data will be dominated by the relative drift motion, a range for which detection is difficult due to positive spacecraft potentials. For heavy ions (O^+) the drift motion is important for thermal energies up to 5 eV and so will be a frequent spin angle feature in the heavy ion outflow samples.

drift speed of the distribution again apparent as a shift from ram.

In summary then, for plasma with thermal speeds much smaller than those of the spacecraft and drift speeds, the relative drift motion dominates the response, leading to a "rammed" flux peak in the direction of relative wind as seen in the spacecraft frame. In this case the angular information is given by subtle features of the detailed shape of the rammed peak but is often indeterminate. For plasma with thermal speeds much larger than those of the spacecraft and drift speeds, the true plasma frame distribution function emerges clearly, although the relative drift motion, appearing as small asymmetries in the angular information, may be difficult to resolve. The RIMS data included in this survey span this entire range of extremes, although the specific set of plasma parameters contributing is mass dependent.

Figure 2 illustrates this for H^+ and O^+ by plotting plasma parameters covered by the data set as a function of ion Mach number. Here ion Mach number is defined as the ratio of the distribution drift velocity (in the Earth frame) to the ion thermal speed $(2\ kT/M)^{1/2}$. Roughly speaking then, it is for subsonic (thermal speed greater than drift speed) ion Mach numbers that the angular characteristics of the distribution will be resolvable. Figure 2 shows that for drift velocities less than 15 km s^{-1} H^+, outflows are subsonic for thermal components as low as 1.0 eV. Hence the angular characteristics of the H^+ samples in the data set should be easily resolvable except for the coldest plasma with strong (V_D > 15 km s^{-1}) drift velocities. O^+ outflows are subsonic at 15 km s^{-1} for thermal components above 10 eV and at 8 km s^{-1} for thermal components above 5 eV. Therefore, for heavy ion outflows with temperatures below 5-10 eV, the angular information will frequently be indeterminate.

Similarly, the drift motion effect is resolvable in the supersonic Mach number range. Because for small thermal components it is the relative difference between drift and spacecraft velocity that is important, Figure 2 can be reinterpreted in terms of a zero ion drift velocity. The shaded region then serves to delineate the range of spacecraft velocities with altitude (~7.6 km s^{-1} at 1.5 R_E geocentric, ~4.2 km s^{-1} at 3 R_E, and ~2.3 km s^{-1} at 4.5 R_E) and therefore the ion Mach range for a discernible relative drift motion effect to the spin angle measurements (i.e., not dominated by the angular response). In the shaded region the relative difference between drift and spacecraft velocity is small, so that light ion (H^+) outflow measurements with thermal energies below ~0.4 eV will be dominated by the relative drift motion – a range for which detection is difficult due to positive spacecraft potentials. For heavy ions (O^+) the drift motion effect is significant for thermal energies up to 5 eV, and so will be a frequent spin angle feature in the heavy ion outflow samples.

3.2. The Classification Scheme

Our approach is to separate the spin angle data into categories representing distinct physical behaviors, both for angular characteristics (the conventional pitch angle distribution) and on the basis of apparent drift speed relative to the spacecraft. As a consequence to this, since the local ion escape speed is near to that of the spacecraft, the apparent drift speed allows us to categorize plasma behaviors loosely in relation to the local escape speed.

Figure 3 shows data measured by RIMS, and they are given as examples of the distribution types featured in this paper. The data are plotted as accumulated counts per sample versus spin phase angle. In addition, the detector pitch angle is plotted as a function of spin angle. The counts per sample is proportional to the integral ion flux for the energy range 0 to 50 eV with approximate conversion ratios of counts to integral flux of 3.1×10^4 counts cm^{-2} s^{-1} $ster^{-1}$ for H^+, 1.9×10^4 counts

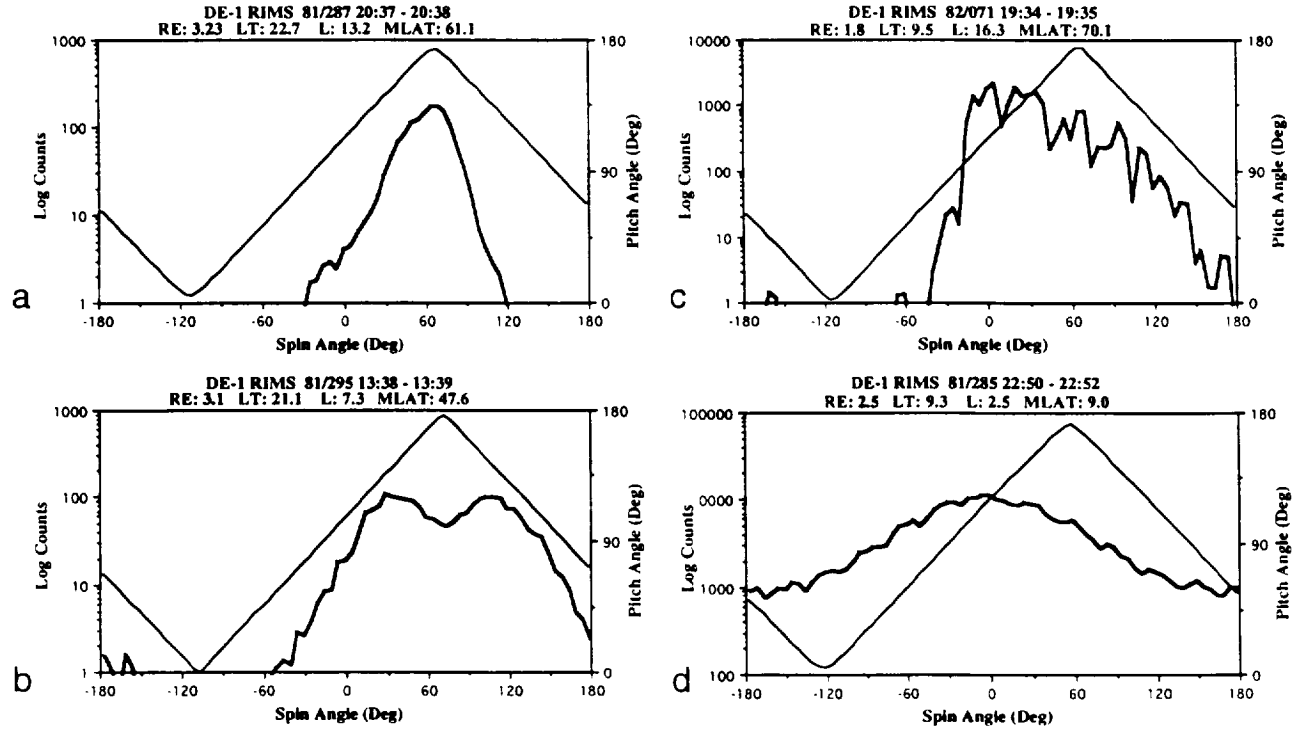

Figure 3. Examples of DE 1 RIMS spin angle distributions typical of high-latitude outflow. Approximate conversion factors from count rate to integral ion flux are given in the text. Illustrated are: (a) unidirectional field-aligned beams, (b) uni-directional field-aligned conics, (c) asymmetric distributions characteristic of the upwelling ion signature, and (d) rammed distributions, which illustrate the effect of comparable spacecraft and plasma outflow velocities as discussed in section 3.

$cm^{-2}\ s^{-1}\ ster^{-1}$ for He^+, and 4.4×10^4 counts $cm^{-2}\ s^{-1}\ ster^{-1}$ for O^+. These factors, which reflect the mass-dependent angular response, are based on preflight and in-flight calibration procedures; the ratios are time-dependent and are offered here only as a general approximation.

The unidirectional field-aligned beam distributions (Figure 3a) are characterized by a single flux peak centered at the field direction (here near 180° pitch angle). These distributions may be shifted from the field direction due to a combination of convection, drift, and spacecraft velocity effects. The important distinction is that these distributions are ordered by pitch angle (magnetic field direction) instead of by spin angle (the velocity vector of the spacecraft) and therefore correspond to field-aligned flows with velocity greater than that of the spacecraft. The rammed distribution (Figure 3d) is most commonly identified in the data by a dome-shaped symmetric peak centered at or near the satellite ram direction. From the arguments above, the rammed distributions correspond to plasma flows that are slower than the spacecraft. The unidirectional field-aligned conic (Figure 3b) are those having flux peaks between the directions perpendicular and parallel to the magnetic field direction. In this example, the spin angle distribution appears as a large single peak but with a distinct drop in count rate at the field direction (180° pitch angle). In other examples, the conic can appear as two separate peaks. The asymmetric distributions (Figure 3c) appear as a single peak in count rate near the spacecraft ram direction but with a notable asymmetry toward the upward magnetic field direction. RIMS samples that have a skew coefficient (equation (5)) exceeding 0.75 toward the upward magnetic field direction will be categorized asymmetric. In the example shown the coefficient of skew is 0.798 defined about the centroid position (14.6° in this example) for the portion of the distribution (61.7° in spin angle width) above the count level equal to $1/e^2$ times the maximum. It is this data signature that is associated with the upwelling ion events first identified by *Lockwood et al.* [1985a]. Distributions fall into the intermediate category when a single peak in the count rate falls between the field and ram directions. For this reason, they cannot be readily assigned to either category and tend to be the samples in which the plasma and spacecraft velocities are more nearly equal. Within the RIMS data set, downflowing field-aligned beam distributions primarily consist of ions falling under the influence of gravity, the velocity of which is expected to be only a few kilometers per second. The unidirectional field-aligned downflows category is a subset of the rammed and intermediate categories and contains the ion downflows for which a clear downward drift velocity is resolvable.

The remaining distribution classifications covered in this paper, nothing observed and low counts, are to classify data signatures that do not fall into one of the categories defined above. The data intervals that have counts below the 2 counts-per-sample noise level are assigned to the "nothing observed" category. The data intervals that have counts above the noise level, but without identifiable maxima are assigned to the "low-count" category. A later paper will examine distribution types primarily identified with midlatitudes (i.e., counterstreaming and trapped); all distribution types are included in the counting statistics so that the porportions reported are representative of the full population.

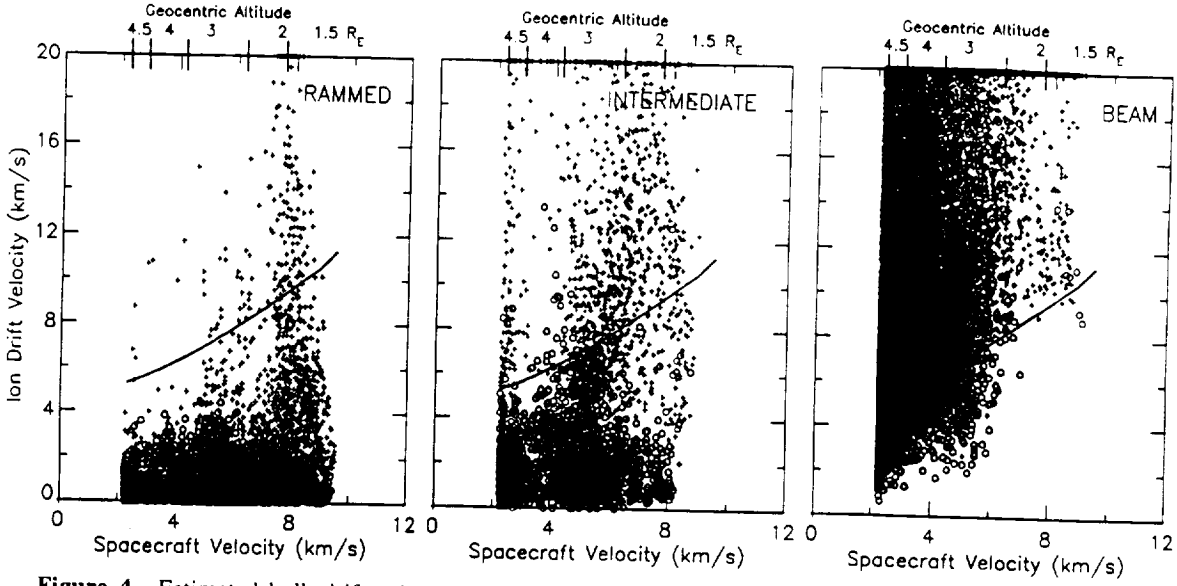

Figure 4. Estimated bulk drift velocities for samples in the rammed, intermediate, and beam PAD categories as a function of spacecraft velocity (and consequently, as a function of altitude which is noted at the top of the plots). The heavy black line marks the ion drift velocity necessary to escape Earth's gravitational potential. The field-aligned outflows correspond to ion drift speeds that are (1) less than, (2) comparable to, or (3) much faster than that of the spacecraft. This separation by observed spin angle distribution serves to identify which PAD categories contain gravitationally bound ions and which contain ions that are more energetic and thus able to escape to outer magnetospheric regions.

Figure 4 quantifies the inferred outflow drift velocities associated with three of the above categories by providing a rough estimate of the bulk drift velocity for each sample as a function of spacecraft velocity (and consequently, as a function of altitude). The heavy black line marks the ion drift velocity necessary to escape Earth's gravitational potential. The intention is to bracket the range of plasma drift speed that result in a given sample being assigned to one category or another. Other studies by DE investigators [*Chandler et al.*, 1991; *Pollock et al.*, 1990] report detailed velocity statistics for polar wind and cleft ion fountain outflows.

The calculation assumes the plasma drift velocity to be aligned with the magnetic field (i.e., no convection) and that only the spacecraft velocity component transverse to the field may bias the observed distribution toward the direction of spacecraft motion. We use the approximation that the magnetic field lies in the spacecraft spin plane . This is generally valid within 12° for the present data set (and within 5° for 91% of the samples). Provided the spin angle corresponding to the centroid of the observed plasma distribution (α) and the spin angle corresponding to the magnetic field direction (β) do not coincide, the plasma drift velocity may be calculated from

$$V_{\text{plasma}} = \frac{V_{\text{spacecraft}} \sin(\alpha)}{\sin(\beta - \alpha)} \tag{7}$$

Figure 5 is a sketch of the vector measurements and angles relating to this calculation. For the rammed category all outflow velocities, with few exceptions (all H^+), fall below the required plasma escape velocity across the entire altitude range; consequently, the samples represented by this category, without additional energization, must either reenter the ionosphere or be trapped by magnetic mirror effects. The intermediate category is a mixture of escaping and nonescaping H^+ samples, and contains mainly nonescaping O^+. The beam category contains the majority of escape velocity samples for both ion species, although there is a significant portion of relatively "fast," but nevertheless nonescaping, O^+ at the highest altitude (lowest spacecraft velocity) bins.

At high latitudes, then, the field-aligned outflows fall into three categories (rammed, intermediate, and field-aligned beams), which, for the energy range detectable by RIMS, correspond to ion flow speeds that are (1) less than, (2) comparable to, or (3) much faster than that of the spacecraft. This separation by observed spin angle distribution serves to identify

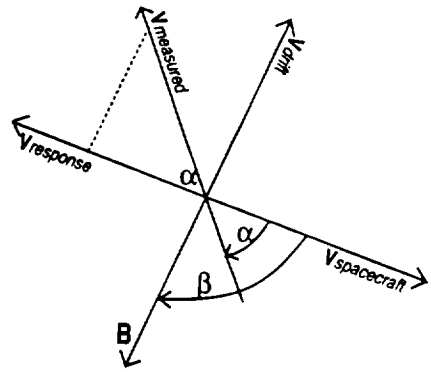

Figure 5. Sketch of the vector measurements and angles for the bulk drift velocity calculation shown in Figure 4. The value α is the centroid of the observed plasma distribution, and β is the spin angle corresponding to the magnetic field direction. The calculation assumes the plasma drift velocity to be aligned with the magnetic field (i.e., no convection) and that only the spacecraft velocity component transverse to the field may bias the observed distribution toward the direction of spacecraft motion.

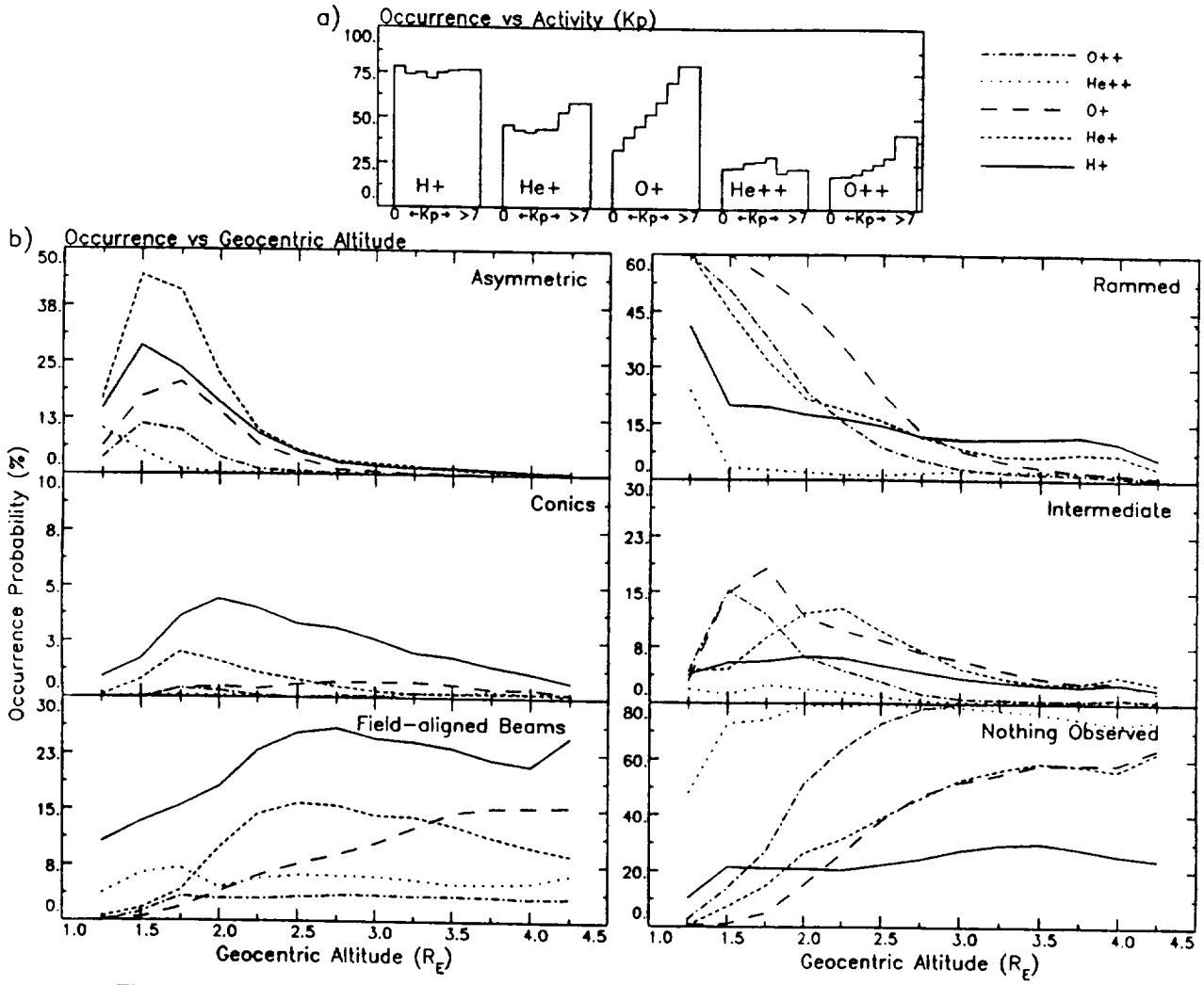

Figure 6. (a) The percentage of samples, during which RIMS was programmed to accept a given ion, the instrument was able to detect that ion. Shown are seven *Kp* bins for H^+, He^+, O^+, *M/Z*=2, and O^{++}. The occurrences are calculated for invariant latitudes above 60° without regard to PAD category, altitude, or local time. (b) In six panels, occurrence with altitude for asymmetric, unidirectional field-aligned conics, unidirectional field-aligned beams, rammed, intermediate, and nothing observed; the calculations include only data above 60° ILAT. The prominent feature to note is the separation of the various distribution types into distinct altitude ranges.

which ions will be gravitationally bound and which are more energetic and thus able to escape to outer magnetospheric regions.

4. Statistical Results

4.1. Occurrences With *Kp* and Altitude

The RIMS instrument, when programmed to detect a selected mass species, may or may not detect appreciable ion counts above the noise threshold within the 0-50 eV energy range. Figure 6a summarizes, as a percentage of the total number of samples, when RIMS measured ion counts above a 2 counts-per-sample threshold. Data are shown for seven magnetic activity level (*Kp*) bins for the ions, H^+, He^+, O^+, *M/Z*=2, and O^{++}. The occurrences are calculated for invariant latitudes above 60°, without regard to altitude, local time, or the categories of pitch angle distributions defined above. The figure simply indicates in what percentage of samples, during which the instrument was programmed to accept a given ion, the instrument was able to detect that ion.

Counts of 0-50 eV H^+ are measured above the detection threshold in 75-78% of the samples, with no significant variation with magnetic activity. In contrast, occurrences of the O^+ ions are strongly dependent on the activity level. At the lowest *Kp* bin, O^+ ions are measured in 33% of the samples; this percentage rises steadily with activity, exceeding the occurrences of H^+ for the highest *Kp* bin. The He^+ ion occurrence probabilities lie between those of H^+ and O^+ and point to a weak dependence on activity. Displaying a pattern similar to that of O^+, O^{++} appears in about 19% of the samples for low *Kp* levels and increases to 41% during times of high *Kp*. *M/Z*=2 ions are seen in 20-29% of the samples, with no clear trend with activity.

Figure 6b has six panels showing the percentage of occurrences as a function of altitude for: (1) asymmetric distributions, (2) unidirectional field-aligned conics, (3) unidirectional field-aligned beams, (4) rammed, (5) intermediate, and

(6) nothing observed; the calculations include only data above 60° ILAT and are sorted without regard to local time. The probability calculations are carried out for each ion species separately. The prominent feature to note in the altitude profiles is the separation of distribution types into distinct altitude ranges. The asymmetric, intermediate, and rammed distributions appear with greatest frequency at altitudes below 2.25 R_E for all ions. Unidirectional conics, most clearly identified in the H^+ samples, peak in probability at midaltitudes between 1.75 and 3 R_E. Unidirectional beams tend to populate the higher end of the altitude range; they reach maximum frequency above 2.5 R_E for H^+ and He^+ and 3.5 R_E for O^+. The nothing observed category, samples with counts below the noise level, also peaks in probability at higher altitudes for He^+, O^+, and O^{++}. Statistics for the M/Z=2 PAD types, not easily viewed in this format, display relatively higher frequencies at the lowest altitudes with the exception of intermediate distributions which occur with uniform frequency across the entire altitude range. It should be noted that in this format, distributions occurring in relatively small areas of local time or latitude will be averaged out in the sort over all local times and latitudes above 60°; this is especially true for the M/Z=2 ion in which the overwhelming number of nothing observed samples masks the contribution of auroral zone outflows.

4.2. Low-Altitude ($R_E \leq 3.0$) Observations

Plate 1 shows low-altitude ($R_E \leq 3.0$) ILAT versus MLT occurrence probabilities (2.5° by 1-hour bins) for rammed (Plate 1a), field-aligned beams (Plate 1b), asymmetric (Plate 1c), and intermediate distributions (Plate 1d). Results are shown for H^+, He^+, and O^+ and divided into $Kp \leq 3$ and $Kp > 3$. The linear scale at the top of these plots and the ones that follow represent the occurrence probability as a percentage, the number of samples fitting the distribution criteria divided by the total number of samples for that ion. The color red represents all probabilities greater than the number noted to the right; similarly, the color blue represents all probabilities lower than the number noted to the left. Corresponding statistics for M/Z=2 and O^{++}, without Kp division, are shown in Plate 2. Fewer M/Z=2 and O^{++} samples at low altitudes preclude statistical calculations by activity level. Note that, for this altitude range, the predawn local time quadrant between 60° and 75° ILAT is not well sampled ("white" indicates less than 15 samples were obtained in a given bin). Although the discussion applies only to the variability of distributions occurring above 60° ILAT, we chose 50° ILAT for the minimum value in these spectrograms to provide overlap and ease of comparison with mid-latitude statistics reported elsewhere.

For $R_E \leq 3.0$ there are relatively few occurrences of H^+ rammed (Plate 1a) at polar cap or auroral zone latitudes except for a small increase (<20%) in occurrences between 70°-80° and 6-12 MLT. All ion species display high occurrences for the rammed category below 60° to 65° ILAT. These are plasmasphere isotropic distributions and characteristically tend toward lower invariant latitudes with increased activity. He^+ rammed PADs occur at greater than 50% probability from midnight to dawn between 60° and 80° ILAT. The O^+ rammed occurs at >50% probability covering ILAT > 70° from premidnight to about 9 MLT. In addition, the O^+ rammed occurs at >25% probability between 60° and 70° ILAT across the dayside. For all ions there is an absence of occurrences at auroral zone latitudes for afternoon local times; occurrences also decrease with increasing magnetic activity. Statistics for rammed O^{++} follow the O^+ pattern with the level of occurrence probability being similar. M/Z=2 follows the He^+ pattern, with probabilities lower by ~50%. In the case of M/Z=2 and O^{++}, and to an extent O^+, lower probability at plasmasphere latitudes as compared to the H^+ and He^+ statistics will be reflected as high probability for the same latitudes in the low counts category. This is a consequence of both the lower relative concentration of these ions within the plasma and instrument operational characteristics (less frequent sampling resulting in erratic low-count distributions).

H^+ low-altitude field-aligned beams (Plate 1b) occur with greater than 30% probability in an oval pattern that covers nearly all local times and appears to be roughly coincident with the auroral oval. There is an expansion of this oval to lower latitudes for high Kp level and evidence of an increase in probability. The He^+ and O^+ probabilities also follow the auroral oval pattern except for an absence of beams in the morning sector – the area populated by rammed distributions. Again, there is an expansion to lower latitudes for higher Kp and increased probability. O^{++} statistics for the beam distributions are not conclusive, although it can be said that O^{++} beams occur with about 10% probability at the same latitudes and local times as for O^+. Since O^+ beam statistics increase uniformly with activity, we might expect the averaging of O^{++} beams over all Kp to lower the mean proportions shown in Plate 2. The M/Z=2 beams, a category which also contains measurements of ~1 keV protons, follows the auroral oval with ~10% probability.

For all ions the asymmetric PAD (Plate 1c, and also referred to as upwelling ion events) has greatest occurrence on the prenoon dayside at invariant latitudes above 65° for the light ions and above 75° for the heavier ions. In addition, there are significant probabilities, increasing with Kp, in the afternoon dayside, and, for the light ions, in the region about 20-22 MLT above 70° ILAT. The overall level of occurrence is higher during active conditions by as much as 20%; much of this increase being the increased afternoon dayside events. Unlike H^+ and He^+, few O^+, M/Z=2, or O^{++} asymmetric events are observed for the polar cap. *Lockwood et al.* [1985a] noted that when the dayside cleft upwelling feature is identified for O^+, the feature is present for all ions measured, so that the cleft region behavior exhibited by O^+ is representative of that for H^+, He^+, M/Z=2, and O^{++} as well. The reverse is not always true. When sorting the lighter ions, the programmed pattern recognition algorithm identifies additional periods of time as fitting the asymmetric criteria (skew coefficient >0.75). Therefore more samples and spatial coverage are tagged as asymmetric for H^+ and He^+ than for O^+. The upwelling ion events associated with the dayside cleft region [*Lockwood et al.*, 1985a] are clearly seen in the O^+ statistics but are imbedded within a larger population of heat flux distributions for H^+ and He^+.

H^+ intermediate distributions (Plate 1d) occur at 10-15% probability across the dayside between 60° and 70° ILAT and at 10-15% probability over the polar cap. He^+ and O^+ intermediate are at 10-20% probability over the polar cap and between 65° to 70° ILAT for all local times. Those over the polar cap increase in probability with activity. Statistics for O^{++} follows the O^+ pattern with a similar spatial pattern but somewhat lower probability. Few M/Z=2 intermediate events are observed above 55° ILAT.

Plate 3 shows low-altitude ($R_E \leq 3.0$) ILAT versus MLT oc-

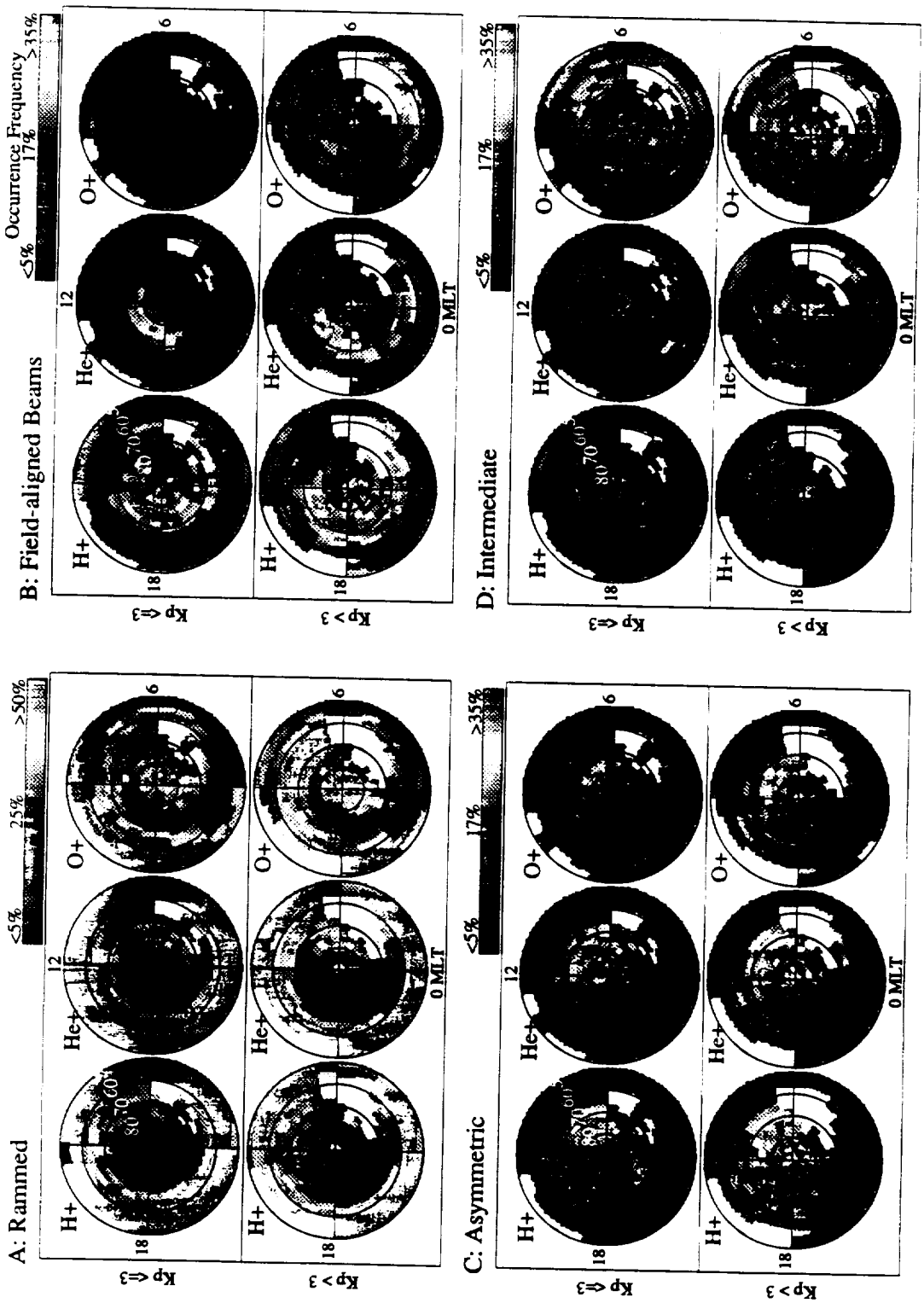

Plate 1. Low-altitude ($R_E \leq 3.0$) ILAT versus MLT occurrence probabilities (2.5° by 1-hour bins) for (a) rammed, (b) field-aligned beams, (c) asymmetric, and (d) intermediate distributions. Results are for H^+, He^+, and O^+ and divided into $Kp \leq 3$ and $Kp > 3$. The linear scale at the top of these figures and the ones that follow represent the occurrence probability as a percentage (the number of samples fitting the distribution criteria divided by the total number of samples). The color red represents all probabilities greater than the number noted to the right; similarly, the color blue represents all probabilities lower than the number noted to the left.

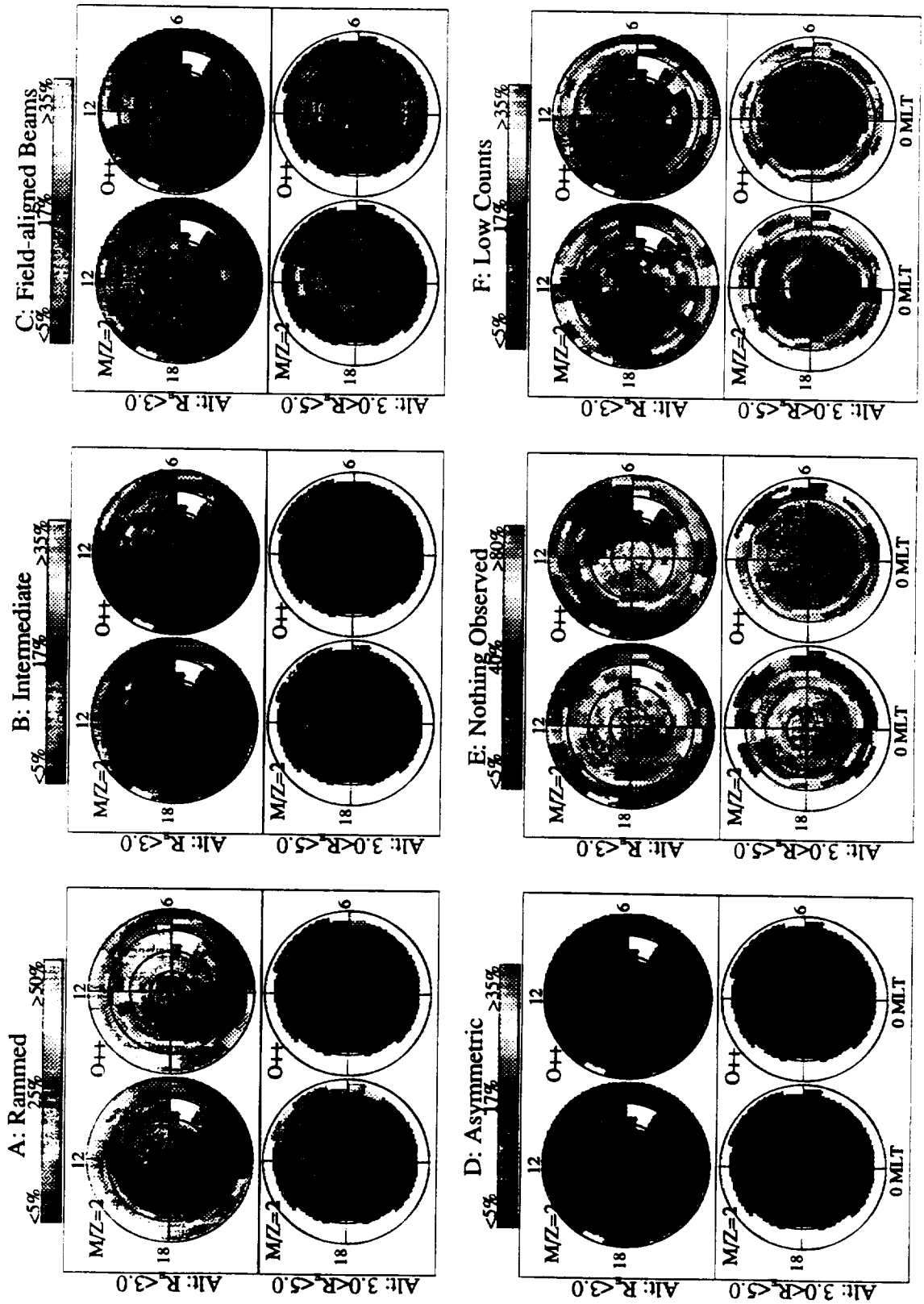

Plate 2. ILAT versus MLT occurrence probabilities for (a) rammed, (b) intermediate, (c) unidirectional field-aligned beams, (d) asymmetric, (e) nothing observed, and (f) low-count distributions. Results are shown for $M/Z=2$ and O^{++} and divided into low altitude ($R_E \leq 3.0$) and high altitude ($3.0 < R_E \leq 4.67$).

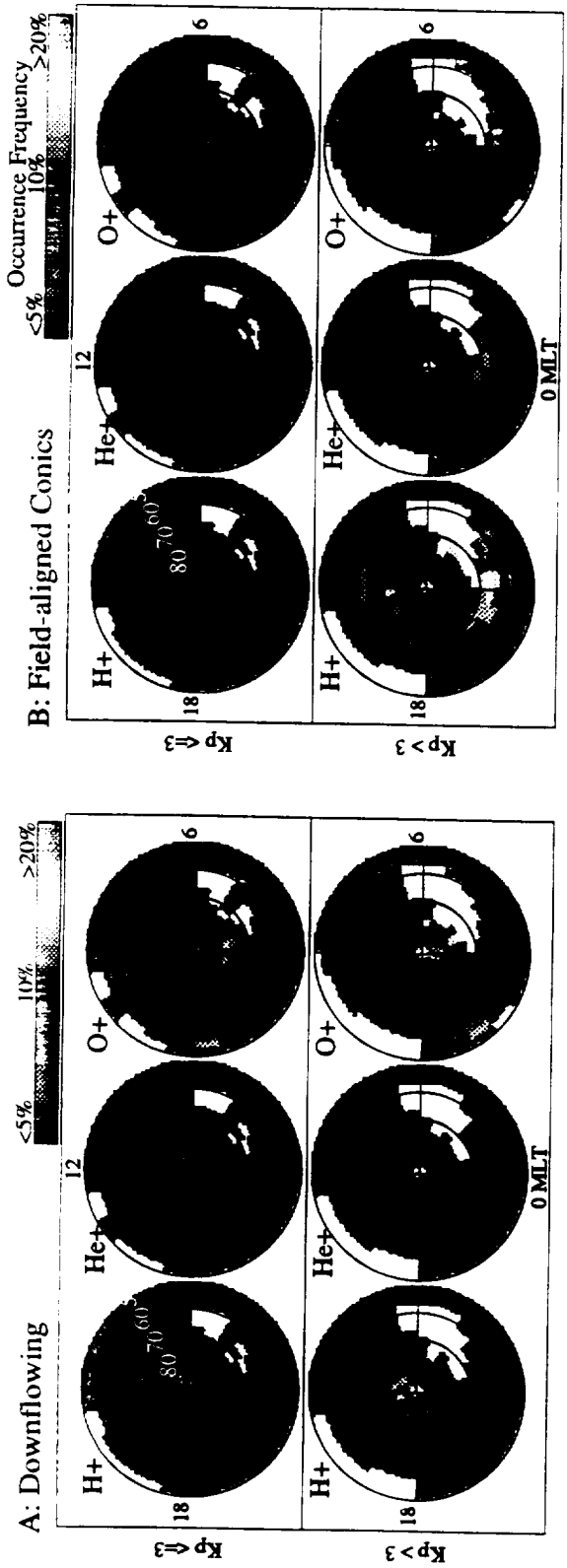

Plate 3. Low-altitude ($R_E \leq 3.0$) ILAT versus MLT occurrence probabilities (2.5° by 1-hour bins) for (a) downflowing and (b) unidirectional field-aligned conic distributions. Results are for H^+, He^+, and O^+ and divided into $Kp \leq 3$ and $Kp > 3$.

currence probabilities for downflowing distributions (Plate 3a) and field-aligned conics (Plate 3b). Results are shown only for H^+, He^+, and O^+ and divided into $Kp \leq 3$ and $Kp > 3$. The downflowing distributions (Plate 3a) are difficult to distinguish from the rammed category for the RIMS energy range because the downward drift speed of the ions tends to be relatively small. H^+ downflows are discernible at polar cap latitudes above 80° with an increase in occurrences with activity. There are also H^+ downflows at 70°-75° ILAT from 11 to 13 MLT. O^+ downflows appear over the nightside polar cap above 80° ILAT with no resolvable change with activity increase. Irregular regions of O^+ downflows also appear below 60° ILAT and are believed associated with convection near the plasmapause. Occurrences of He^+, M/Z=2, and O^{++} downflows are less than 5% overall. The H^+ unidirectional conics (Plate 3b) are most frequently observed at invariant latitudes between 70° and 80° in the dayside local time sectors, and at invariant latitudes between 60° and 70° on the nightside. There is an increase (about 10%) in probability for observations of conics with an increase in magnetic activity. The unidirectional conic occurrences for the remaining ions are below 10% although, at least in the case of He^+, the occurrences show hints of following the H^+ pattern.

4.3. Higher-Altitude ($3.0 < R_E \leq 4.67$) Observations

Plate 4 shows high-altitude ($3.0 < R_E \leq 4.67$) ILAT versus MLT occurrence probabilities for rammed (Plate 4a), field-aligned beams (Plate 4b), asymmetric (Plate 4c), and intermediate distributions (Plate 4d). Results are for H^+, He^+, and O^+ and divided into $Kp \leq 3$ and $Kp > 3$. Corresponding statistics for M/Z=2 and O^{++}, without the Kp division, are shown in Plate 2.

The high occurrences of heavy ion rammed distributions (Plate 4a) at low altitudes do not appear in the high-altitude statistics. In fact, there is almost a complete absence of rammed distributions at auroral zone and polar cap latitudes for all the ions measured with the exception of a small area of about 10-15% probability for high activity at 70°-80° ILAT postmidnight for H^+ and at 65°-75° ILAT premidnight for O^+. Again, the probabilities below 60° to 65° ILAT are associated with plasmasphere isotropic distributions.

H^+ high-altitude beams (Plate 4b) occur not only for auroral latitudes but at all latitudes greater than 70° across the full dayside sector. On the nightside, beams are observed with comparable probability only for auroral oval latitudes from midnight to dawn, the beams almost disappearing at from dusk to midnight. He^+ beams occur with greatest probability (20-30%) at invariant latitudes between 60° and 80° between 6 to 19 MLT. There are somewhat lower, but still significant (15-18%), probabilities at 60° to 65° latitude from midnight to dawn. O^+ high-altitude beams occur with greatest probability during higher activity. These are at latitudes greater than 70°-75°, covering the entire polar cap between for all local times; and also from 60° to 65° between midnight and noon. For the high-altitude observations, in addition to an invariant latitude expansion with increasing magnetic activity, the beams are also observed at lower invariant latitudes for heavier masses. This expansion is between 5° and 10° for each of the mass species. For M/Z=2, a category which also contains measurements of ~1 keV protons, there is about 15% probability between 75° and 80° ILAT on the dayside and between 60° to 70° ILAT on the nightside. The probability for

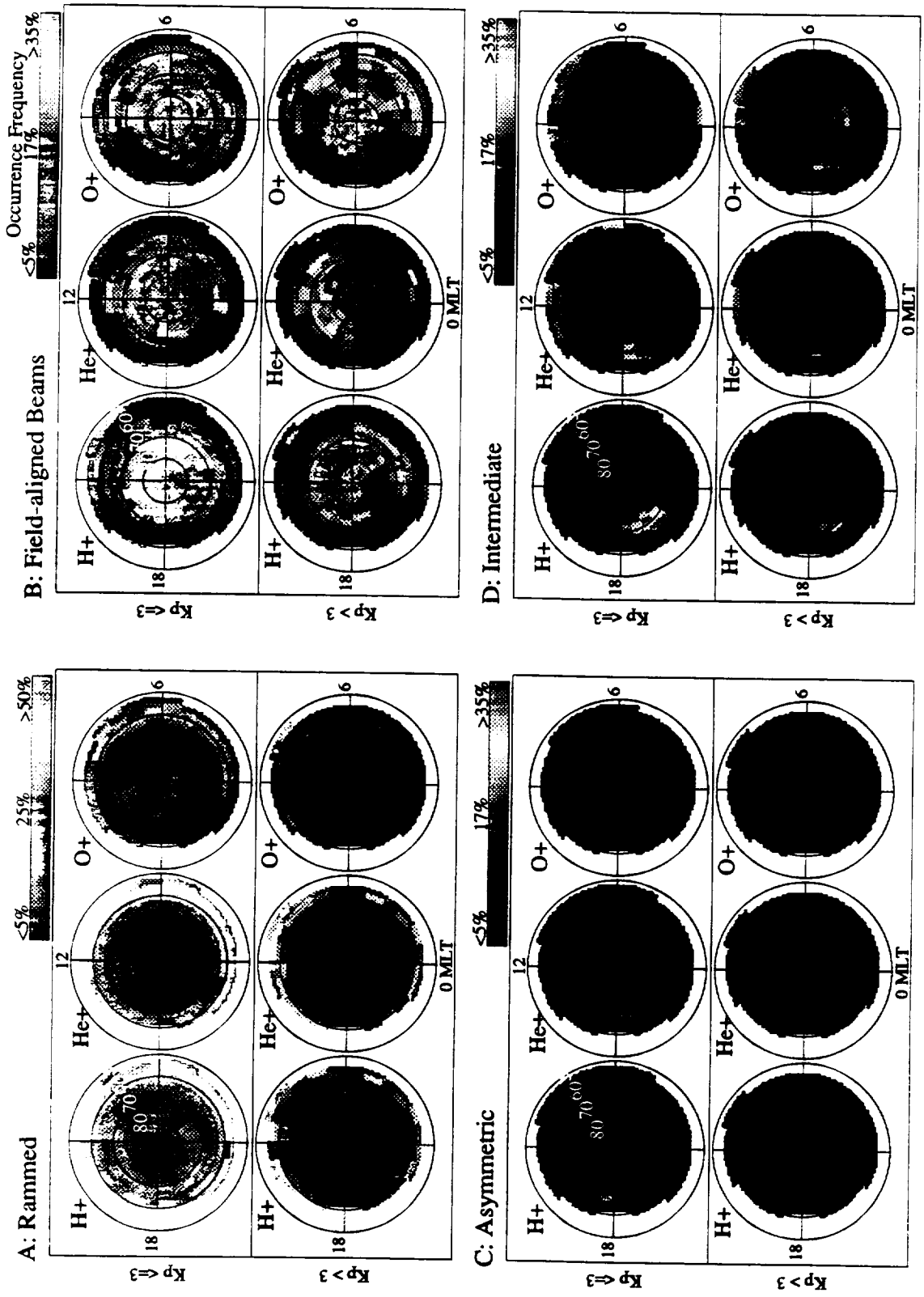

Plate 4. Higher-altitude ($3.0 < R_E \leq 4.67$) ILAT versus MLT occurrence probabilities for (a) rammed, (b) field-aligned beams, (c) asymmetric, and (d) intermediate distributions. Results are for H^+, He^+, and O^+ and divided into $Kp \leq 3$ and $Kp > 3$.

O^{++} unidirectional beams is less than 10% with the exception of a small area of about 15% probability at 70°-80° ILAT and 11-13 MLT.

The asymmetric distributions (Plate 4c) make up less than 5% of the PAD samples at high altitude with the exception of a small area of about 10% probability for H^+ at 65°-75° ILAT on the nightside for high magnetic activity. Similar to the ram and asymmetric results, the intermediate category (Plate 4d) is a much smaller proportion of the high-altitude sample population and, instead of appearing spread over the entire polar cap as for the low-altitude observations, they are limited to the nightside auroral zone between 20 MLT and 2-4 MLT. The distribution of observations is similar for all ions with lighter ions appearing at slightly lower latitudes and movement toward higher latitudes with higher magnetic activity.

4.4. Absence of Cold Plasma Observations

Plate 5 shows low-altitude ($R_E \leq 3.0$) ILAT versus MLT occurrence probabilities for nothing observed (Plate 5a) and low count distributions (Plate 5b) and high-altitude ($3.0 < R_E \leq 4.67$) probabilities for nothing observed (Plate 5c) and low count distributions (Plate 5d). Results are shown for H^+, He^+, and O^+ and divided into $Kp \leq 3$ and $Kp > 3$. Statistics for M/Z=2 and O^{++}, not sorted for activity, are shown in Plate 2.

H^+ low-altitude nothing observed events (Plate 5a) occur for latitudes above 70° ILAT across the nightside and above 80° ILAT across the dayside for low Kp and with lower frequency above 70° ILAT at all local times for high Kp. For high altitude the H^+ nothing observed events (Plate 5b) occur over the polar cap and, for low Kp, at auroral zone latitudes near midnight. There is also significant probability below 60° ILAT at dusk, indicating a depletion of thermal ions in the plasma trough area there. He^+ low-altitude nothing observed events occur at >30% probability for all latitudes above 65° across the nightside and above 70° ILAT across the dayside. There is an expansion to slightly lower latitudes for higher Kp and slightly overall decreased probability. For high altitude the He^+ nothing observed events occur at >50% probability for all latitudes above 65°-70° ILAT at all local times. High-altitude O^+ nothing observed events occur at up to 75% probability over the entire polar cap and auroral zone area for low Kp; for high Kp the O^+ nothing observed events drop dramatically in frequency and follow the auroral oval pattern. O^{++} generally follows the pattern of O^+, although without division with Kp it is not known whether a decrease in occurrence probability occurs with activity. M/Z=2 follows that of He^+.

Low-count statistics are not significant at low altitude (Plate 5c), the observations that do occur appear at outer plasmasphere/plasma trough latitudes. For high altitude the low count category (Plate 5d) becomes important for the H^+ ion near midnight at auroral zone and polar cap latitudes.

5. Discussion

The low-energy (<50 eV) H^+, He^+, O^+, M/Z=2, and O^{++} RIMS spin angle distributions for latitudes greater than 60° have been classified into the following pitch angle distribution categories: unidirectional field-aligned beams, downflows, conics, asymmetric, rammed, intermediate, low counts, and nothing observed.

5.1. Ionospheric Source Regions

The statistical survey shows that low-energy outflow from the high-latitude ionosphere occurs for all the measured ions with a spatial and statistical distribution dependent on magnetic activity. For convenience, we discuss the outflows in terms of three regions: the dayside cleft, auroral zone, and polar cap.

During quiet times, cleft region upwelling ion events (the asymmetric distributions in Plate 1) are observed almost exclusively in the prenoon sector. The area of most probable observation becomes smaller and is bounded at higher invariant latitudes for the heavier mass species. These asymmetric, field-aligned spin distributions are identified as ions carrying an upward heat flux, with both parallel and perpendicular velocity components, and so "upwell" in response to heating below the satellite [*Moore et al.*, 1985; *Biddle et al.*, 1985; *Lockwood et al.*, 1985a]. *Moore et al.* [1985] demonstrated that the upwellings exhibit conic structure in the energetic tail of the distribution and suggested that the distinction between the unidirectional beam, conic, and upwelling categories may be a matter of the degree by which transverse acceleration affects the low-energy core of the distribution. The probability of observing upwelling events in the morning sector is relatively steady regardless of activity level which contrasts sharply with the large increase with activity seen with the auroral O^+ outflowing beams (Plate 1b). This is consistent with *Lockwood et al.* [1985a] in which these prenoon O^+ outflows from the polar cleft ionosphere were first identified as a major source of heavy ions for the polar cap magnetosphere. There is, in addition, a distinct spatial change for cleft outflow with increased activity – at higher Kp levels upwelling events appear on the afternoon dayside and the area of peak probability spreads to lower latitudes. In a study of the source characteristics of these events, *Moore et al.* [1986] found typical energies to be of the order of 10 eV and found that the distinctive transverse ion heating exceeds gravitational escape requirements. Evidence from this and the other studies indicates then, that the dayside prenoon cleft is a consistent source of low-energy ions of velocity sufficient to escape to outer magnetosphere regions regardless of species (including the minor ions M/Z=2 and O^{++}) or activity level and that the dayside afternoon auroral zone becomes an additional source during increasing activity.

While it is clear from the statistics that this asymmetric data signature, an indicator of transverse heating in the ionospheric outflows, is specific to auroral latitudes, it cannot be unambiguously stated that they are unique to the dayside auroral zone. Figure 6b shows the peak observance of these events to be between 1.5 and 2.0 R_E geocentric altitude. Unfortunately, due to a combination of instrument operation and orbital constraints, samples taken below 1.75 R_E geocentric cover only the 5 to 12 MLT range. Samples between 1.75 and 2.0 R_E geocentric add auroral latitudes from 19 to 24 MLT. If, as has been suggested, the upwelling data signature evolves by magnetic folding to a field-aligned conic distribution, and if the asymmetric data signature does exist for the entire auroral zone, we would expect to find ample evidence of conics at nightside auroral latitudes, which is the case as can be seen in Plate 3b.

Low-energy ion outflows associated with the auroral oval itself are mainly of the unidirectional beam type (Plate 1b). For

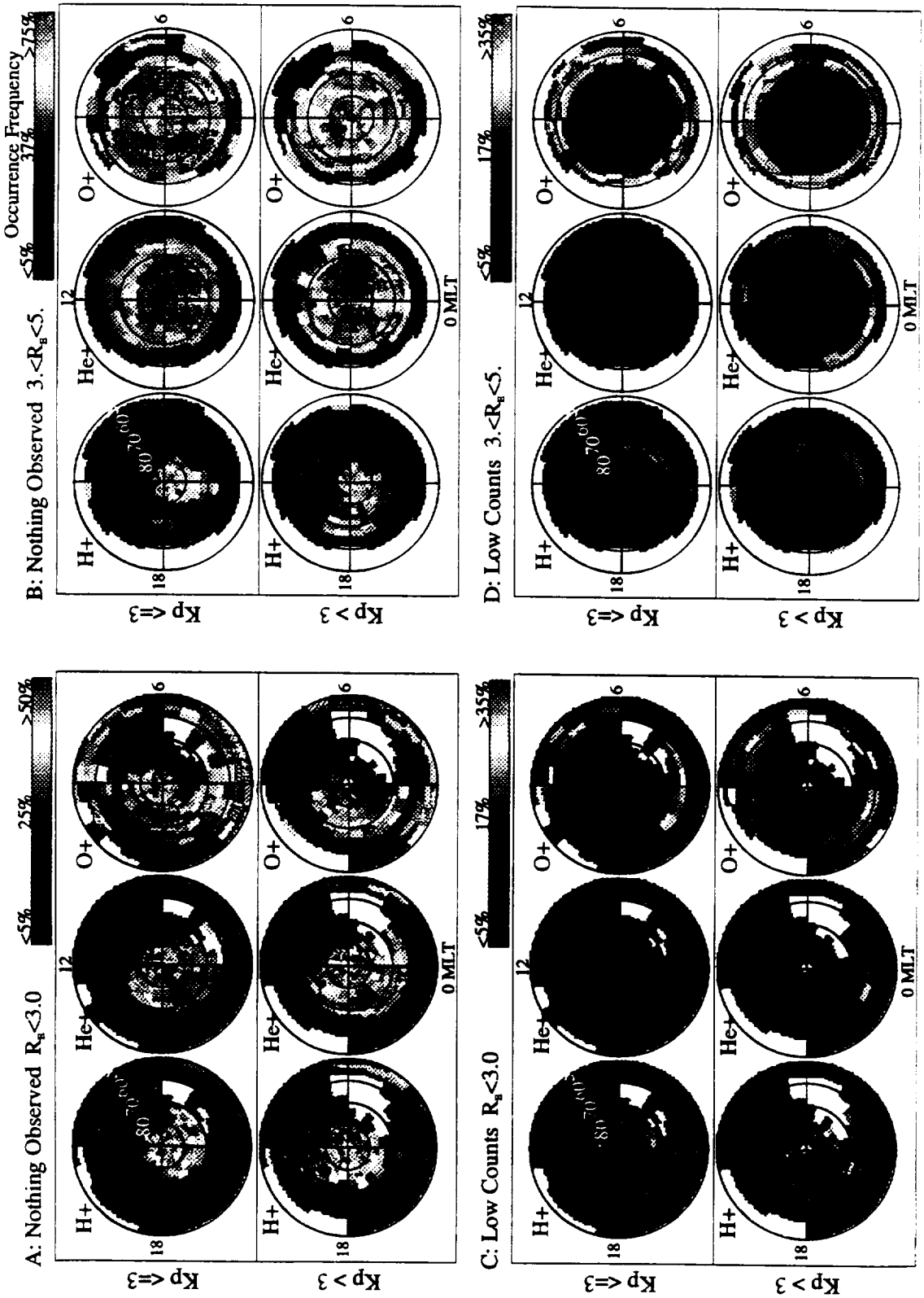

Plate 5. Low-altitude ($R_E \leq 3.0$) ILAT versus MLT occurrence probabilities for (a) nothing observed and (c) low-count distributions and high-altitude ($3.0 < R_E \leq 4.67$) probabilities for (b) nothing observed and (d) low-count distributions. Results are shown for H^+, He^+, and O^+ and divided into $Kp \leq 3$ and $Kp > 3$.

H^+, unidirectional beams are observed in the auroral zone for most all local times, increasing by about 10% with activity. The beam distributions are observed at progressively lower invariant latitudes for heavier mass species. These observations are in agreement with the earlier studies of *Ghielmetti et al.* [1978] and *Gorney et al.* [1981] in that the occurrence of upward flowing beams appears to be associated with the statistical auroral oval. The occurrence frequencies peak more equatorward on the nightside than for the dayside, and peak at lower invariant latitudes during disturbed times. The observations are also consistent with *Yau et al.* [1984], who also found that the oval of upflowing beams is energy dependent (the low-energy upflowing oval occurring poleward of the energetic ion upflowing oval). In addition, for heavier ions the beams display a distinct asymmetry in distribution speed between dawn and dusk local time sectors. For He^+ and O^+ the unidirectional beams are observed primarily for the dusk sector and increase significantly in probability with increasing activity (as much as a 30% increase for O^+). The "nothing observed" category complements this duskside behavior by having probability greater than 50% in this same region for low activity and decreasing sharply for high activity (Plate 5a). In the dawn sector the heavier ion distributions, especially O^{++}, tend to be the lower velocity rammed type (Plate 1a). Since the unidirectional beam distributions generally have adequate escape velocity (Figure 4), the auroral zone then appears to be a steady source of escape velocity H^+ for all local times, a steady source of escape velocity He^+ ions on the duskside, and a source of escape velocity heavy ions on the duskside but primarily during increased activity. The fact that the He^+ and O^+ low-altitude dawn-sector rammed and intermediate distributions (Plates 1a and 1d) fill in the missing beam distributions suggests that there is an amount of low-energy heavy ions unable to escape to high altitudes unless acted upon by energization processes which are correlated with increased activity. The M/Z=2 ion beam statistics contain measurements of ~1 keV protons and so it is unclear whether escape velocity outflows other than the asymmetric type exist for this mass type.

For latitudes poleward of the auroral zone the pitch angle distribution statistics vary with mass, activity level, and local time. The majority of the heavy ion observations in which significant counts are detected (>50 or 60%) are of the rammed and intermediate type (Plates 1a and 1d), which still indicate field-aligned upflow, but with velocities comparable to the spacecraft and shown in section 3 not to be sufficient for escape to higher altitudes without additional energization. There is also a dawn-dusk asymmetry reflected in the ion distribution "speed" in which higher speed distributions appear with greatest frequency at dusk and lower speed distributions have greatest frequency at dawn. There appear to be small changes in the probability levels with magnetic activity, a slight increase in rammed distributions, and a small decrease in intermediate observations; however, it is important to note that there is always low-energy O^+ at low altitudes over the entire high-latitude region regardless of activity (Figure 6b). On the other hand, H^+ has a significant number of heat flux (asymmetric), unidirectional beams, and intermediate events for latitudes poleward of the auroral zone, the probabilities for these categories increasing with activity. There are relatively few rammed distributions H^+, although the "nothing observed" category for H^+ has >50% probability for low Kp. The He^+ observations have characteristics of both H^+ and O^+, the "nothing observed"/heat flux statistics of H^+ and the rammed/intermediate statistics of O^+. Overall, the region poleward of the auroral zone is again a consistent source of low-energy ions, although we would expect only the lighter mass particles to have sufficient velocity to escape to higher altitudes.

5.2. Evolution of Field-Aligned Distributions During Outflow

By comparing distribution types at low altitudes with those at high altitudes we can infer something about how low-energy ion distributions evolve after ionosphere injection. The rammed distributions, which make up a significant portion of dawnside heavy ion observations at low altitude, essentially disappear at high altitude (Plate 4a). These either reenter the ionosphere or are trapped by magnetic mirror effects. If these low drift velocity rammed distributions instead experienced energization, such that the ramming effect no longer dominated, then we would expect a significant portion of "faster speed" distributions such as intermediate or field-aligned beams in the dawnside polar cap, which is not the case. For similar reasons the intermediate distributions seen at low altitudes are also believed to return to the ionosphere or remain trapped. At low altitude, only the asymmetric and field-aligned conic distributions, which reflect a significant degree of transverse acceleration, and the field-aligned beam distributions appear to account for the statistical patterns observed at high altitudes. The observations support two mechanisms, which may well be related, for low-energy outflow into the outer magnetosphere (the cleft ion fountain, so named by *Lockwood et al.* [1985b], and its counterpart in other sectors of the auroral oval) what the present authors call the auroral ion fountain.

The cleft ion fountain, as explained by *Lockwood et al.* [1985b], consists of ionospheric plasma of 1-20 eV energy streaming upward into the magnetosphere where high-latitude convection electric fields can modify the ion path resulting in a poleward dispersion. This effect is a well-documented feature [cf. *Waite et al.*, 1986; *Moore et al.*, 1985; *Tsunoda et al.*, 1989] and is clearly evident by the beam distributions at high altitude over the polar cap (Plate 4b). It is not certain whether all the high-altitude O^+ polar cap observations originate from the cleft ion fountain mechanism; however, the very low probabilities of observing escape velocity O^+ outflow at low altitudes in the polar cap would indicate that this is so. The outflows in Plate 4b also demonstrate the mass spectrometer effect associated with the cleft fountain whereby the lighter ions escape to the magnetosphere tail regions, but the heavier low-energy ions, such as O^+, are more influenced by the convection electric field and are swept toward the nightside auroral region and plasma sheet. For weaker convection, heavier ions outflowing on the dayside would be swept antisunward over the polar cap and reenter the nightside polar ionosphere. This is supported by the Plate 3 O^+ downflows.

The auroral ion fountain concept is reflected in the field-aligned beam and conic results. For the RIMS instrument the unidirectional field-aligned beams correspond to pitch angle distributions that have not undergone magnetic mirroring and can be represented by a drifting Maxwellian distribution with supersonic drift speed [*Moore et al.*, 1985]. Traveling upward, these ions flow along high-latitude field lines that are open; or closed in a highly elongated fashion such that bouncing would occur over long time periods and be disrupted by nonadiabatic

processes. Low-altitude auroral latitudes are populated by beam distributions near dusk, "slower" intermediate or rammed distributions at dawn, and conics on the nightside (Plates 1 and 3). High-altitude, late-afternoon beams are almost absent; instead the region is represented by the intermediate and "nothing observed" categories (Plates 4 and 5). It is hypothesized that low-altitude field-aligned beams flow outward along auroral field lines, and for late afternoon, experience additional acceleration, such that the ion energy distribution exceeds the instrument detection range (>50-60 eV). Higher-energy beams, particularly those >1 keV, have been shown to have strong local time dependence, being concentrated near dusk at auroral latitudes [*Gorney et al.*, 1981; *Yau et al.*, 1984; *Kondo et al.*, 1990].

The sequence of events for both the cleft ion fountain and the auroral ion fountain is consistent with the theory that a continuum of behavior exists such that the upwelling distributions evolve with altitude into conics and then high-altitude, field-aligned flows (cf. Figure 6). Conics correspond to upward field-aligned flows that have some additional perpendicular velocity component. Conic distributions typical of the midaltitude nightside have been studied by *Moore et al.* [1985] and found to originate between 1000 and 2000 km altitude which is consistent with the altitude distribution shown in Figure 6. The study of *Gorney et al.* [1981], based on electrostatic analyzer data at higher energies (0.09 to 3.9 keV), found that ion conics occur in the geocentric distance range of 1.4 up to the S3-3 apogee at 2.3 R_E, or about 2500- to 8000-km altitude and that ion beams occur primarily above about 2.2 R_E, or 7200-km altitude, with the frequency increasing with altitude. During quiet times the S3-3 conics were associated with the daytime polar cusp region, but were observed uniformly in local time during disturbed times. The older studies did not distinguish between events peaked near 90° pitch angle (our asymmetric category) and those peaked between 120° and 170° pitch angle (our conic category). However, they are consistent with our observations in that our dayside asymmetric events exist for all activity levels, while those observations associated with our more narrowly defined conic category are found to increase with activity and are distributed in local time. The S3-3 results are also consistent in that quiet time ion beams have maximum frequency in the premidnight sector and are mainly confined to the dusk sector during disturbed times.

5.3. Considerations on the Absence of Cold Plasma Observations

The "low-count" and "nothing observed" categories are representative of two possible conditions: regions in which the ions have energy so low that they are repelled by positive spacecraft potentials or of regions where there are no ions within the detection range of the instrument, the low-count samples being those that occur near the limits of the instrument response (~0.1 ions cm^{-3} with no potential barrier). Analysis of RIMS data by *Olsen* [1989] established a density-potential relationship such that the satellite accumulates positive charge on entering density regions below 1000 cm^{-3}, rising slowly to about +1 V at 100 cm^{-3}, and about +5 V at 10 cm^{-3}. By preventing measurements of the coldest plasma components, this potential can mask out an isotropic background plasma or, when the potential is sufficiently high, can give the appearance that no cold plasma exists in a region. This effect is known to be a concern in the plasmapause and trough region, where densities are of the order of 7 to 70 cm^{-3} and the spacecraft reaches potentials of +2 to +5 V [*Olsen*, 1989]. At altitudes above the ionosphere in the polar regions, densities again can be sufficiently low so that observation of ions of classical polar wind speed is possible only during negative aperture bias instrument modes to offset the positive potential [*Nagai et al.*, 1984]. We cannot always assume, in low-density regions, that cold plasma does not exist just because it has not been measured.

The RIMS H^+ nothing observed events at low altitude may be representative of an inability to observe the lowest-energy polar wind outflows in low-density regions. As detailed in the above discussion on the "auroral ion fountain," at high altitude near midnight, the H^+ nothing observed events are thought to be measurements in which the low-altitude outflows have been accelerated beyond the range of the instrument. The He^+ and O^+ events in the dusk auroral zone are probably a mixture of the two effects.

6. Summary

We have presented a statistical study of the occurrence frequency distribution of low-energy ion pitch angle distributions in the near-Earth magnetosphere using measurements from the retarding ion mass spectrometer aboard Dynamics Explorer 1. A relationship is shown between pitch angle distributions of different masses (H^+, He^+, O^+, M/Z=2, and O^{++}) and velocity characteristics. The added spatial dimensions in this study relative to earlier work provide a more detailed picture of ion transport events. Occurrence frequencies are determined for all measured ions as a function of altitude, invariant latitude, magnetic local time, and magnetic activity (Kp). From this study, several characteristics are apparent.

6.1. Overall Occurrence With Activity

The probability of observing H^+ and M/Z=2 distributions for ILAT >60° was found to be independent of magnetic activity. He^+ was found to be weakly dependent, while O^+ and O^{++} were strongly dependent on magnetic activity. The large increase in O^+ and O^{++} observations with increasing activity was found to be composed primarily of escape velocity unidirectional field-aligned and upwelling distribution types.

Upwelling (transversely heated, upflowing) ions occur predominantly, but perhaps not exclusively, in the pre-noon sector at 70°-80° ILAT. At higher Kp levels the events are observed with increased probability on the afternoon dayside and at slightly lower latitudes for all ion species.

The occurrence of unidirectional beams, for all ion species including M/Z=2, is consistent with the location and geomagnetic activity dependent expansion and contraction of the auroral oval. The data suggest that beam distributions observed at higher altitudes are predominately associated with the upwelling distributions observed at lower altitudes and that the paths for ions injected at low altitude in the dayside auroral oval include some amount of convection antisunward over the polar cap, as suggested in the *Lockwood et al.* [1985a, b] cleft ion fountain sequence.

Peak conic and upwelling ion observations occur predominantly at geocentric distances of 1.75 and 2.0 R_E, respectively, while field-aligned beams occur most frequently above about 2.0 to 2.25 R_E, especially for the heavier ions. Since

angular distributions tend to become increasingly "beamlike" at higher altitudes because of magnetic focusing it is thought that the upwelling events may well evolve into the observed unidirectional conic and beam distributions as the ions travel outward along the magnetic field direction.

6.2. Ionospheric Source Regions

The dayside prenoon cleft is a consistent source of low-energy ions of escape velocity regardless of species or activity level and the dayside afternoon cleft, or auroral zone, region adds to this source for increased activity.

The auroral oval as a whole appears to be a steady source of escape velocity H^+ ions at all local times, a steady source of escape velocity He^+ ions for the dusk sector, and a source of escape velocity heavy ions for dusk but primarily for increased activity.

The region poleward of the auroral zone is a consistent source of low-energy ions, although only the lighter mass particles appear to have sufficient velocity to escape to higher altitudes.

6.3. Evolution of Field-Aligned Distributions During Outflow

The observations support two concepts for outflow: (1) The cleft ion fountain consists of ionospheric plasma of 1-20 eV energy streaming upward into the magnetosphere where high-latitude convection electric fields modify the ion paths resulting in a poleward dispersion of the ion trajectories. (2) The auroral ion fountain consists of field-aligned beams which stream outward along auroral latitude field lines, and in addition, for late afternoon local times, experience additional acceleration, such that ion energy distributions tend to exceed the detection range of the instrument (>50-60 eV).

6.4. Absence of Cold Plasma Observations

The "low-count" and "nothing observed" trends with magnetic activity appear to complement that of the unidirectional field-aligned beam distributions and are representative of two possible conditions: regions in which the ions have energies relative to the spacecraft so low that they are repelled by positive spacecraft potentials or regions with no ions having energies within the detection range of the instrument. We cannot always assume, in low-density regions, that cold plasma does not exist just because it has not been measured.

Acknowledgments. The authors would like to thank the RIMS team at Marshall Space Flight Center and the programming staff of the Boeing corporation for assistance with the DE telemetry reduction software. The research at the University of Alabama in Huntsville was sponsored by grant NAG8-234. The authors thank both referees for their helpful comments.

The Editor thanks W. B. Hanson and A. W. Yau for their assistance in evaluating this paper.

References

Balsiger, H., P. Eberhardt, J. Geiss, and D. T. Young, Magnetic storm injection of 0.9- to 16-keV/*e* solar and terrestrial ions into the high-altitude magnetosphere, *J. Geophys. Res.*, *85*, 1645, 1980.

Beyer, W. H., *CRC Standard Mathematical Tables*, p. 496, CRC Press, Boca Raton, Fl, 1984.

Biddle, A. P., T. E. Moore, and C. R. Chappell, Evidence for ion heat flux in the light ion polar wind, *J. Geophys. Res.*, *90*, 8552, 1985.

Breig, E. L., and W. B. Hanson, Deuterium and hydrogen flows in the thermosphere, *J. Geophys. Res.*, *96*, 17,779, 1991.

Breig, E. L., S. Sanatani, and W. B. Hanson, Deuterium in the daytime thermosphere, *J. Geophys. Res.*, *92*, 225, 1987.

Candidi, M., S. Orsini, and V. Formisano, The properties of ionospheric O^+ ions as observed in the magnetotail boundary layer and northern plasma lobe, *J. Geophys. Res.*, *87*, 9097, 1982.

Chandler, M. O., J. H. Waite Jr., T. E. Moore, Observations of polar ion outflows, *J. Geophys. Res.*, *96*, 1421, 1991.

Chappell, C. R., Initial observations of thermal plasma composition and energetics from Dynamics Explorer-1, *Geophys. Res. Lett.*, *9*, 929, 1982.

Chappell, C. R., S. A. Fields, C. R. Baugher, J. H. Hoffman, W. B. Hanson, W. W. Wright, H. D. Hammack, G. R. Carignan, and A. F. Nagy, The retarding ion mass spectrometer on Dynamics Explorer-A, *Space Sci. Instrum.*, *5*, 477, 1981.

Chappell, C. R., J. L. Green, J. F. E. Johnson, and J. H. Waite Jr., Pitch angle variations in magnetospheric thermal plasma – Initial observations from Dynamics Explorer-1, *Geophys. Res. Lett.*, *9*, 933, 1982a.

Chappell, C. R., R. C. Olsen, J. L. Green, J. F. E. Johnson, and J. H. Waite Jr., The discovery of nitrogen ions in the Earth's magnetosphere, *Geophys. Res. Lett.*, *9*, 937, 1982b.

Chappell, C. R., T. E. Moore, and J. H. Waite Jr., The ionosphere as a fully adequate source of plasma for the Earth's magnetosphere, *J. Geophys. Res.*, *92*, 5896, 1987.

Comfort, R. H., I. T. Newberry, and C. R. Chappell, Preliminary statistical survey of plasmaspheric ion properties from observations by DE 1/RIMS, in *Modeling Magnetospheric Plasma, Geophys. Monogr. Ser.*, vol. 44, edited by T. E. Moore and J. H. Waite Jr., p. 107, AGU, Washington, D. C., 1988.

Craven, P. D., R. C. Olsen, C. R. Chappell, and L. Kakani, Observations of molecular ions in the Earth's magnetosphere, *J. Geophys. Res.*, *90*, 7599, 1985.

Delcourt, D. C., B. L. Giles, C. R. Chappell, and T. E. Moore, Low-energy bouncing ions in the magnetosphere: A three-dimensional numerical study of Dynamics Explorer 1 data, *J. Geophys. Res.*, *93*, 1859, 1988.

Eastman, T. E., L. A. Frank, W. K. Peterson, and W. Lennartsson, The plasma sheet boundary layer, *J. Geophys. Res.*, *89*, 1553, 1984.

Fields, S. A., C. R. Baugher, C. R. Chappell, D. L. Reasoner, H. D. Hammack, W. W. Wright, and J. H. Hoffman, Instrument manual for the retarding ion mass spectrometer on Dynamics Explorer-1, *NASA Tech. Mem. 82484*, 1982.

Frank, L. A., K. L. Ackerson, and D. M. Yeager, Observations of atomic oxygen (O^+) in the Earth's magnetotail, *J. Geophys. Res.*, *82*, 129, 1977.

Geiss, J., H. Balsiger, P. Eberhardt, H. P. Walker, L. Weber, D. T. Young, and H. Rosenbauer, Dynamics of magnetospheric ion composition as observed by the GEOS mass spectrometer, *Space Sci. Rev.*, *22*, 537, 1978.

Ghielmetti, A. G., R. G. Johnson, R. D. Sharp, and E. G. Shelley, The latitudinal, diurnal, and altitudinal distributions of upward flowing energetic ions of ionospheric origin, *Geophys. Res. Lett.*, *5*, 59, 1978.

Giles, B. L., Inner magnetosphere circulation of thermal ions inferred from observed pitch angle distributions, Ph.D. thesis, Univ. of Ala., Huntsville, 1993.

Giles, B. L., C. R. Chappell, J. H. Waite Jr., T. E. Moore, and J. L. Horwitz, Dynamic evolution of low-energy ions in the terrestrial magnetosphere, in *Modeling Magnetospheric Plasma, Geophys. Monogr. Ser.*, vol. 44, edited by T. E. Moore and J. H. Waite Jr., p. 177, AGU, Washington, D. C., 1988.

Gorney, D. J., A. Clarke, D. Croley, J. Gennell, J. Luhmann, and P. Mizera, The distribution of ion beams and conics below 8000 km, *J. Geophys. Res.*, *86*, 83, 1981.

Hardy, D. A., J. W. Freeman, and H. K. Hillis, Double-peaked ion spectra in the lobe plasma: Evidence for massive ions?, *J. Geophys. Res.*, *82*, 5229, 1977.

Hultqvist, B., On the origin of the hot ions in the disturbed dayside magnetosphere, *Planet. Space Sci.*, *31*, 173, 1983.

Johnson, R. G., R. D. Sharp, and E. G. Shelley, Observations of ions of ionospheric origin in the stormtime ring current, *Geophys. Res. Lett.*, *4*, 403, 1977.

Kondo, T., B. A. Whalen, A. W. Yau, and W. K. Peterson, Statistical analysis of upflowing ion beam and conic distributions at DE 1 altitudes, *J. Geophys. Res.*, *95*, 12,091, 1990.

Lennartsson, W., and E. G. Shelley, Survey of 0.1- to 16-keV/*e* plasma sheet ion composition, *J. Geophys. Res.*, *91*, 3061, 1986.

Lennartsson, W., E. G. Shelley, R. D. Sharp, R. G. Johnson, and H. Balsiger, Some initial ISEE-1 results on the ring current composition and dynamics during the magnetic storm of December 11, 1977, *Geophys. Res., Lett.*, *6*, 483, 1979.

Lockwood, M., J. H. Waite Jr., T. E. Moore, J. F. E. Johnson, and C. R. Chappell, A new source of suprathermal O^+ ions near the dayside polar cap boundary, *J. Geophys. Res.*, *90*, 4099, 1985a.

Lockwood, M., M. O. Chandler, J. L. Horwitz, J. H. Waite Jr., T. E. Moore, and C. R. Chappell, The cleft ion fountain, *J. Geophys. Res.*, *90*, 9736, 1985b.

Lundin, R., L. R. Lyons, and N. Pissarenko, Observations of the ring current composition at L = 4, *Geophys. Res., Lett.*, *7*, 425, 1980.

Lundin, R., B. Hultqvist, N. Pissarenko, and A. Zackarov, The plasma mantle: Composition and the characteristics observed by means of the Prognoz-7 satellite, *Space Sci. Rev.*, *31*, 2267, 1982a.

Lundin, R. B., Hultqvist, E. Dubinin, A. Zackarov, and N. Pissarenko, Observations of outflowing ion beams on auroral field lines at altitudes of many Earth radii, *Planet Space Sci.*, *30*, 715, 1982b.

Moore, T. E., Origins of magnetospheric plasma, *Revs. Geophys. Suppl.*, 1039, 1991.

Moore, T. E., M. O. Chandler, C. R. Chappell, C. J. Pollock, J. H. Waite Jr., J. L. Horwitz, and C. R. Wilson, Features of terrestrial plasma transport, *Philos. Trans. R. Soc. London Ser. A.*, *328*, 235, 1989.

Moore, T. E., C. R. Chappell, M. Lockwood, and J. H. Waite Jr., Superthermal ion signatures of auroral acceleration processes, *J. Geophys. Res.*, *90*, 1611, 1985.

Moore, T. E., M. Lockwood, M. O. Chandler, J. H. Waite Jr., C. R. Chappell, A. Persoon, and M. Sugiura, Upwelling O^+ ion source characteristics, *J. Geophys. Res.*, *91*, 7019, 1986.

Nagai, T., J. F. E. Johnson, and C. R. Chappell, Low-energy (<100 eV) ion pitch angle distributions in the magnetosphere by ISEE 1, *J. Geophys. Res.*, *88*, 6944, 1983.

Nagai, T., J. H. Waite Jr., J. L. Green, C. R. Chappell, R. C. Olsen, and R. H. Comfort, First measurements of supersonic polar wind in the polar magnetosphere, *Geophys. Res. Lett.*, *11*, 669, 1984.

Olsen, R. C., Charging characteristics of Dynamics Explorer I retarding ion mass spectrometer and the consequence for core plasma measurements, *Tech. Rep. NPS-61-89-014*, Nav. Postgrad. Sch., Monterey, Calif., 1989.

Olsen, R. C., R. H. Comfort, M. O. Chandler, T. E. Moore, J. H. Waite Jr., D. L. Reasoner, and A. P. Biddle, DE 1 RIMS operational characteristics, *NASA Tech. Mem. 86527*, 1985.

Peterson, W. K., R. D. Sharp, E. G. Shelley, and R. G. Johnson, Energetic ion composition of the plasma sheet, *J. Geophys. Res.*, *86*, 761, 1981.

Peterson, W. K. E. G. Shelley, G. Haerendel, and G. Paschmann, Energetic ion composition in the subsolar magnetopause and boundary layer, *J. Geophys. Res.*, *87*, 2139, 1982.

Pollock, C. J., M. O. Chandler, T.E. Moore, J. H. Waite Jr., C. R. Chappell, and D. A. Gurnett, A survey of upwelling ion event characteristics, *J. Geophys. Res.*, *95*, 18,969, 1990.

Sharp, R. D., R. G. Johnson, and E. G. Shelley, Observations of an ionospheric acceleration mechanism producing energetic (keV) ions primarily normal to the geomagnetic field direction, *J. Geophys. Res.*, *82*, 3324, 1977.

Sharp, R. D., R. G. Johnson, and E. G. Shelley, Energetic particle measurements from within ionospheric structures responsible for auroral acceleration processes, *J. Geophys. Res.*, *84*, 480, 1979.

Sharp, R. D., D. L. Carr, W. K. Peterson, and E. G. Shelley, Ion streams in the magnetotail, *J. Geophys. Res.*, *86*, 4639, 1981.

Sharp, R. D., W. Lennartsson, W. K. Peterson, and E. G. Shelley, The origins of the plasma in the distant plasma sheet, *J. Geophys. Res.*, *87*, 10,420, 1982.

Shelley, E. G., R. G. Johnson, and R. D. Sharp, Satellite observations of energetic heavy ions during a geomagnetic storm, *J. Geophys. Res.*, *77*, 6104, 1972.

Tsunoda, R. T., R. C. Livingston, J. F. Vickley, R. A. Heelis, W. B. Hanson, F. J. Rich, and P. F. Bythrow, Dayside observations of thermal ion upwellings at 800-km altitude: An ionospheric signature of the cleft ion fountain, *J. Geophys. Res.*, *84*, 15,277, 1989.

Waite, J. H., Jr., T. Nagai, J. F. E. Johnson, C. R. Chappell, J. L. Burch, T. L. Killeen, P. B. Hays, G. R. Carignan, W. K. Peterson, and E. G. Shelley, Escape of suprathermal O^+ ions in the polar cap, *J. Geophys. Res.*, *90*, 1619, 1985.

Waite, J. H., Jr., T. E. Moore, M. O. Chandler, M. Lockwood, A. Persoon, and M. Sugiura, Ion energization in upwelling ion events, in *Ion Acceleration in the Magnetosphere and Ionosphere*, *Geophys. Monogr. Ser.*, vol. 38, edited by T. Chang, p. 61, AGU, Washington, D. C., 1986.

Yau, A. W., B. A. Whalen, W. K. Peterson, and E. G. Shelley, Distribution of upflowing ionospheric ions in the high-altitude polar cap and auroral ionosphere, *J. Geophys. Res.*, *89*, 5507, 1984.

Yau, A. W., E. G. Shelley, W. K. Peterson, and L. Lenchyshyn, Energetic auroral and polar ion outflow at DE 1 altitudes: Magnitude, composition, magnetic activity dependence, and long-term variations, *J. Geophys. Res.*, *90*, 8417, 1985.

Young, D. T., J. Geiss, H. Balsiger, P. Eberhardt, A. Ghielmetti, and H. Rosenbauer, Discovery of He^{++} and O^{++} ions of terrestrial origin in the outer magnetosphere, *Geophys. Res. Lett.*, *4*, 561, 1977.

Young, D. T., H. Balsiger, and J. Geiss, Correlations of magnetospheric ion composition with geomagnetic and solar activity, *J. Geophys. Res.*, *87*, 9077, 1982.

C. R. Chappell, NASA Marshall Space Flight Center, Huntsville, AL 35812.

R. H. Comfort, Department of Physics and Center for Space Plasma and Aeronomic Research, University of Alabama in Huntsville, Huntsville, AL 35899. (e-mail: SPAN cspara::comfort)

B. L. Giles and T. E. Moore, Space Sciences Laboratory, NASA Marshall Space Flight Center, Huntsville, AL 35812. (e-mail: Internet giles@ssl.msfc.nasa.gov; Internet mooret@mpb.msfc.nasa.gov)

J. H. Waite Jr., Southwest Research Institute, San Antonio, TX 78284. (e-mail: SPAN swri::hunter)

(Received July 14, 1993; revised March 23, 1994; accepted March 30, 1994.)

Appendix C

Chandler et al reprint
Polar Wind notes

JOURNAL OF GEOPHYSICAL RESEARCH, VOL. 96, NO. A2, PAGES 1421–1428, FEBRUARY 1, 1991

Observations of Polar Ion Outflows

M. O. CHANDLER

Space Science Laboratory, NASA George C. Marshall Space Flight Center, Huntsville, Alabama

J. H. WAITE, JR.

Department of Space Sciences, Southwest Research Institute, San Antonio, Texas

T. E. MOORE

Space Science Laboratory, NASA George C. Marshall Space Flight Center, Huntsville, Alabama

The characteristics of the polar ion outflows as observed in the topside polar ionosphere by the Dynamics Explorer Retarding Ion Mass Spectrometer are reported in this study. The study is restricted to altitudes between 1000 and 4000 km in order to focus on the phenomenon of the "classical polar wind." Except insofar as they convect into the polar cap at these altitudes, auroral and cusp/cleft outflows are specifically excluded from this study. Using a method based on the "relative wind" of ions as seen from the moving spacecraft, averages and variances of the magnetic field-aligned ion flux and velocity, and the species densities, are derived and binned for examination of their altitudinal, seasonal, and magnetic activity dependencies. The data set used encompasses the period from autumn 1981 through 1983, the altitude range from 1000 to 4000 km, and invariant latitudes greater than 70°. Observations of H^+, He^+, and O^+ with energies down to spacecraft potential are reported. It is found that the polar outflows are not well correlated with common indicators of solar or geomagnetic activity. The average parameters of the outflows exhibit a winter enhancement of He^+ flux, a winter decrease in H^+ flux, and a summer enhancement of the asymptotic outflow speeds of all species. The solar $F_{10.7}$ (and hence EUV) flux is correlated with the acceleration profile of the flows, with slower flow velocities at 2500 km altitude for active solar conditions. Evidence is found that the H^+ flows are, at times, subsonic in the altitude range studied, in contrast to cold polar wind models.

INTRODUCTION

The upward flow of ionospheric ions from Earth's polar region has been studied extensively over the past two decades with the bulk of the work being theoretical. The earliest suggestions regarding this phenomenon were based on the then new idea of open magnetic field lines connecting the polar ionosphere to the distant magnetotail and the solar wind magnetic field which would provide a means of escape for ions energetic enough to overcome Earth's gravitational pull. *Dungey* [1961] noted that open magnetic field lines should upset the plasma equilibrium along those field lines. *Dessler and Michel* [1966] and *Nishida* [1966] pointed out that at sufficiently high temperatures H^+ would "evaporate" from the ionosphere and escape into the tail. Numerical studies involving solutions to the steady state hydrodynamic equations showed that when the dominant species in the ionosphere is O^+ these heavier ions and electrons play a role in the ion outflow process by creating an ambipolar electric field through which the lighter H^+ and He^+ are accelerated [*Banks and Holzer*, 1968, 1969*a*,*b*]. *Axford* [1968] invoked this "polar wind" flow to provide a nonthermal escape mechanism for He from the terrestrial atmosphere. Following these initial modeling efforts, discussions of the outflow under collisionless conditions spawned several kinetic models [*Dessler and Cloutier*, 1969; *Lemaire and Scherer*, 1970, 1971, 1972] which were later shown to be in agreement with the hydrodynamic formulations [*Banks et al.*, 1971].

Increasingly, more detailed models have been developed to study the dynamics and energetics of the outflow of H^+, He^+, and O^+ from the polar region [*Marubashi*, 1970; *Holzer et al.*, 1971; *Lemaire*, 1972; *Banks*, 1973; *Bailey and Moffett*, 1974; *Banks et al.*, 1974, 1976; *Strobel and Weber*, 1972; *Raitt et al.*, 1975, 1977, 1978*a*,*b*; *Schunk et al.*, 1978; *Schunk and Watkins*, 1979, 1981, 1982; *Ottley and Schunk*, 1980; *Gombosi et al.*, 1985; *Barakat et al.*, 1987; *Schunk and Sojka*, 1989]. All but the most recent of these have been reviewed by *Raitt and Schunk* [1983]. The basic predictions for ion outflow have remained roughly the same over two decades at $\sim 10^8$ and $\sim 10^7$ ions cm^{-2} s^{-1} (at 1000 km altitude) for H^+ and He^+, respectively.

Raitt and Schunk [1983] have pointed out the lack of experimental observations of the polar cap outflows. To date, the results include initial observations of the nondiffusive density profiles and upward H^+ flow by *Hoffman* [1970] from Explorer 31 and measurements of the outflow of H^+ and He^+ from ISIS 2 by *Hoffman et al.* [1974] and *Hoffman and Dodson* [1980]. This latter study included data from a 4-week period centered on the winter and summer solstices and the spring and autumn equinoxes of 1971 and 1972 with approximately 50 orbits of data for each season at an altitude of 1400 km. The basic results include H^+ fluxes of the order of 10^8 cm^{-2} s^{-1} and He^+ fluxes of the order of 10^7 cm^{-2} s^{-1} (at 1000 km altitude) with strong seasonal dependence.

Case studies of polar outflow have recently been carried out using data from the Dynamics Explorer (DE) mission [*Gurgiolo and Burch*, 1982; *Sojka et al.*, 1983; *Nagai et al.*, 1984]. These studies concentrated on the ion velocity distributions of polar wind outflows demonstrating the supersonic behavior of the H^+ ion outflow at high altitudes. *Biddle et al.* [1985] also used DE data to determine the ion heat flux in polar wind outflows and found at least one case to be in agreement with theoretical predictions that the sense of the heat flux should reverse as the plasma flow becomes supersonic. In addition, results of statistical studies of upflowing ions with energies greater than 10 eV have been presented by *Yau et al.* [1985*a*,*b*].

Paper number 90JA02180.
0148-0227/91/90JA-02180$05.00

The following results are based on observations of polar cap ion outflows using the retarding ion mass spectrometer (RIMS) on DE 1 [*Chappell et al.*, 1981]. The purpose is to show average values of ion flux, velocity, and density as well as altitudinal, seasonal, and magnetic activity-related variations in the polar outflows for energies down to ionospheric values (<1 eV). The addition of these results to those already published will provide a more complete picture of the phenomena of ion outflow from the polar region.

DATA AND TECHNIQUES

The data for this study were taken during the period from October 1981 through April 1983 and cover the altitude range from 1000 to 4000 km. All observations are from the RIMS radial detector which samples ions in the satellite spin plane. The spin plane contains the satellite velocity vector and is parallel to the orbit plane. The ion velocity and flux measurements are obtained by integrating the observed flux over the spin cycle of the satellite for a zero retarding potential analyzer (RPA) voltage. A full description of the technique with error analysis can be found in the work by *Chandler and Chappell* [1986].

It should be noted that using the zero RPA setting implies that any superthermal population which may be present in the high-latitude ionosphere will also be included in this analysis. This is unavoidable since these data are taken from the period when the RPA was not functioning. An attempt has been made to minimize the possibility of "contamination" by superthermal populations of either auroral or cusp origin by restricting the observations to invariant latitudes greater than 70° and altitudes below 4000 km.

The velocity measurements were made under the assumption of zero convective plasma motion in the satellite spin plane. Error analysis shows that this assumption results in errors of less than 50% in the resulting velocities for convective electric fields, at ionospheric altitudes, of less than 100 mV m^{-1}. To minimize the effects of convective electric fields the data have been restricted to invariant latitudes greater than 70°.

For the average flux and velocity values the statistical standard deviation is typically of the order of the average value of the quantity. Thus all error bars shown in this paper are the statistical values for one standard deviation. *Chandler and Chappell* [1986] concluded that the error in determining the ion velocity was of the order of 100 m s^{-1}. In the present study the data have been averaged into 2°-wide bins in spin-phase angle. This ±1° uncertainty in the angles yields errors of the order of 20% following the error analysis of *Chandler and Chappell* [1986]. However, it also yields a lower limit on the measurable velocity of ~150 m s^{-1} (under the assumption that the satellite velocity is 8 km s^{-1} and perpendicular to the magnetic field). Given the high outflow velocities for H^+ and He^+ the 20% error is the more useful number. For O^+, however, this lower limit results in some ambiguity for the lowest measured values.

The calculation of ion densities in this study assumes zero spacecraft potential. Because of the large spacecraft velocity the O^+ ram energy was >4.5 eV in all cases. Thus the O^+ Mach number, relative to the spacecraft, was >2 (assuming an O^+ thermal energy less than 1 eV) and only small errors (<20%) in the O^+ density calculations are expected due to spacecraft potential. Likewise, the He^+ Mach number was likely to be >1 resulting in errors less than a factor of 2 for potentials less than 2 V. On the other hand, the H^+ Mach number could range from 1 down to 0.5 for a 1 eV thermal energy resulting in density estimates too low by up to a factor of 4 for potentials up to 2 V. However, the average O^+ density in this data set is >500 cm^{-3} at all altitudes which, based on the results of *Olsen* [1989], gives an estimated spacecraft potential of less than 1 V. For a 1 V potential the maximum errors for He^+ and H^+ densities become factors of 1.3 and 2.0, respectively. These estimates of the reduction of flux due to positive spacecraft potential are derived from simulations of the RIMS instrument using the equations of *Parker and Whipple* [1970].

Approximately 2000 1-min-duration observations were analyzed for each ion. After restricting the data to high latitudes the total number of observations is 914 for each ion species. The distribution of data samples with respect to season was 61 samples in spring, 205 samples in summer, 521 samples in autumn, and 127 samples in winter.

OBSERVATIONAL RESULTS

Average Flux

Variability with geophysical parameters. It is expected that the outflow of ions from the polar regions will vary in its magnitude with variations in geophysical parameters. The RIMS polar wind data have been studied in an attempt to show the magnitude of such variations in velocity and flux. The polar wind outflow should vary with season as a result of changes in the solar EUV input as well as from known seasonal variations in the neutral atmosphere composition (e.g., winter enhancements in [H] and [He]). Table 1 shows the average flux of H^+ and He^+ for four seasons defined by contiguous periods centered on the equinoxes and the solstices. The H^+ flux exhibited a factor of 3 variation over the seasons, being largest (1.5×10^8 cm^{-2} s^{-1}) in spring and smallest (5×10^7 cm^{-2} s^{-1}) in the winter. In contrast, the He^+ flux was observed to reach its maximum value in the winter (2×10^7 cm^{-2} s^{-1}) and its minimum value in the summer (1×10^6 cm^{-2} s^{-1}). In addition, the He^+ winter value was larger than that observed in spring by a factor of 2.

TABLE 1. Seasonal Variation of the Polar Wind Flux

Season	Flux, cm^{-2} s^{-1}	
	H^+	He^+
Winter	6×10^7	2×10^7
Spring	1.5×10^8	1×10^7
Summer	5×10^7	1×10^6
Autumn	8×10^7	6×10^6

Solar cycle variations. The RIMS data in this study come from a period of declining solar activity. However, because of the relatively short time period spanned by the observations, the variation in the solar 10.7 cm flux was not large. There are few observations from periods of $F_{10.7} > 200$ (10^{-22} W m^{-2} Hz^{-1}) and fewer still for $F_{10.7} < 100$ (10^{-22} W m^{-2} Hz^{-1}). Also, for the winter portion of the year there was insufficient spread in the $F_{10.7}$ values to make meaningful correlations with the magnitude of the flux. For the summer season the spread was large enough to provide results; however, there is no indication of a significant trend in the data with respect to $F_{10.7}$.

Variation with magnetic activity. To determine the effects of geomagnetic activity on the ion flux in the polar region, two indices were chosen, *Kp* and *Ap*. In the correlations of flux with the *Kp* index it was found that using the index from the 3-hour period previous to the time of a given observation resulted in aver-

ages with smaller standard deviations. While there exist some variations in the observed outflow with the *Kp* index, the variation is only a factor of 3 over the entire range of values observed (0 to 7–). Similarly, the variations in H^+ with the daily-averaged *Ap* also show about a factor of 3 variation. Neither of these variatiions is considered significant when compared to the standard deviations about the means.

Average Velocity

The average H^+ upward velocity, from all data at invariant latitudes greater than 70°, is shown in Figure 1. At altitudes below ~2000 km the average speed is near constant at 3–4 km s^{-1}. In the region between 2000 and 3000 km the speed increases to ~10 km s^{-1} and remains nearly constant, albeit with an increased standard deviation, above 3000 km. In order to illustrate the effects of different geophysical parameters on the ion speed, the data was binned according to the day of the year and by the value of the 10.7-cm solar flux. Figure 2 shows the H^+ velocity averaged over day-of-year for values of the 10.7 cm flux <140 (10^{-22} W m^{-2} Hz^{-1}) and >190 (10^{-22} W m^{-2} Hz^{-1}). While this binning excludes a significant number of observations which fall in the range from 140 (10^{-22} W m^{-2} Hz^{-1}) to 190 (10^{-22} W m^{-2} Hz^{-1}), the separation between the bins accentuates the differences. The difference between these two profiles appears in the midaltitude region where for low $F_{10.7}$ the speeds in this region are ~50% higher than for high $F_{10.7}$ flux. In addition, in the high $F_{10.7}$ flux case the acceleration occurs above 2000 km whereas for the low $F_{10.7}$ flux case the increase in speed begins below 2000 km. While this effect is small and is within the standard deviations, the fact that it is seen in all the averages between 1500 and 4000 km suggests that it is indeed a real effect.

For averages over all $F_{10.7}$ values but at different seasons of the year the profiles again exhibit significant differences. In Figure 3 the speeds are shown for the summer season (May 6–August 4 in the northern hemisphere and November 4–February 3 in the southern hemisphere) and the winter season (November 4–February 3 in the northern hemisphere and May 6–August 4 in the southern hemisphere). There are no significant differences in the average speeds in the altitude range below 2000 km. However, at altitudes above 2500 km the average speed for summer is ~25–70% higher than the winter average. Again, as in the case of the results in Figure 2, the deviation about the mean is large in the high-altitude region, suggesting additional influences controlling the maximum speed.

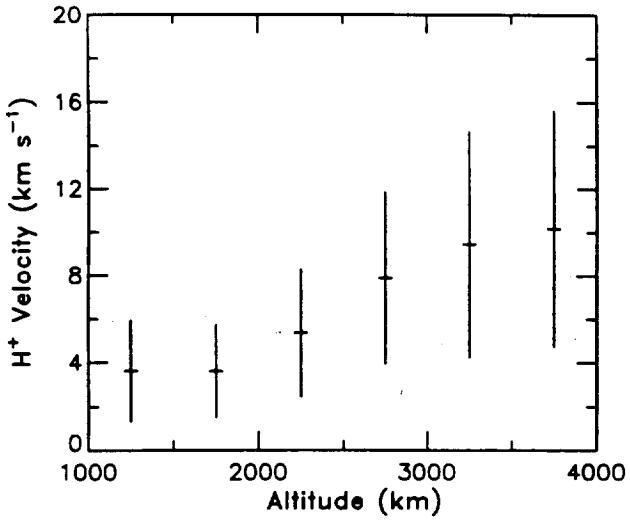

Fig. 1. The average velocity of H^+ as a function of altitude for all data.

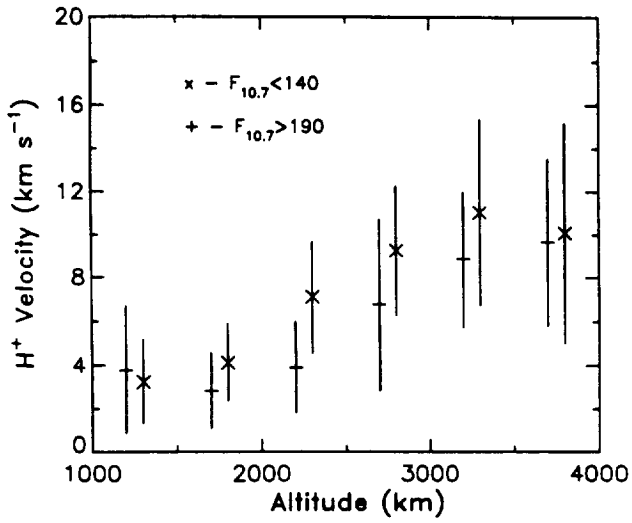

Fig. 2. The average velocity of H^+ as a function of altitude for $F_{10.7} < 140$ (10^{-22} W m^{-2} Hz^{-1}) and $F_{10.7} > 190$ (10^{-22} W m^{-2} Hz^{-1}).

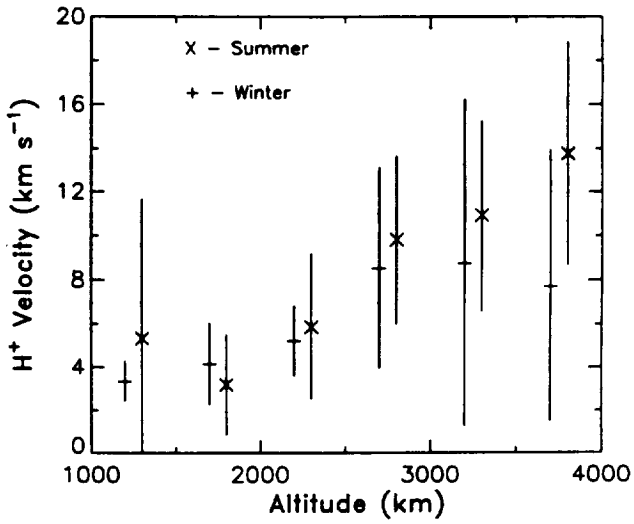

Fig. 3. The average velocity of H^+ as a function of altitude for the summer season and the winter season.

The two-season binning is not entirely satisfactory for showing the real seasonal variation. Unfortunately, there are insufficient data to allow meaningful results as a function of altitude to be obtained for all seasons. There are sufficient data to produce good statistics for the autumnal equinox case. As might be expected the maximum average speeds fall between those for summer and winter.

The outflow speeds for He^+ are about a factor of 3–4 less than the H^+ values on average, although the deviations about the mean values are similar. While the altitude profiles are similar to those of H^+, there exist some noticeable differences. Figure 4 shows the He^+ speeds for high and low $F_{10.7}$ flux. Due to the larger variations about the mean values these results are not as clean as those for H^+. The results are, however, similar to those for H^+ with regard

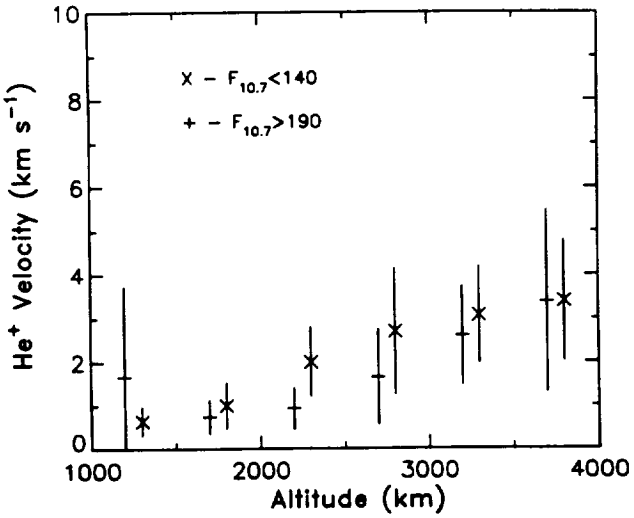

Fig. 4. The average velocity of He^+ as a function of altitude for $F_{10.7} < 140$ (10^{-22} W m^{-2} Hz^{-1}) and $F_{10.7} > 190$ (10^{-22} W m^{-2} Hz^{-1}).

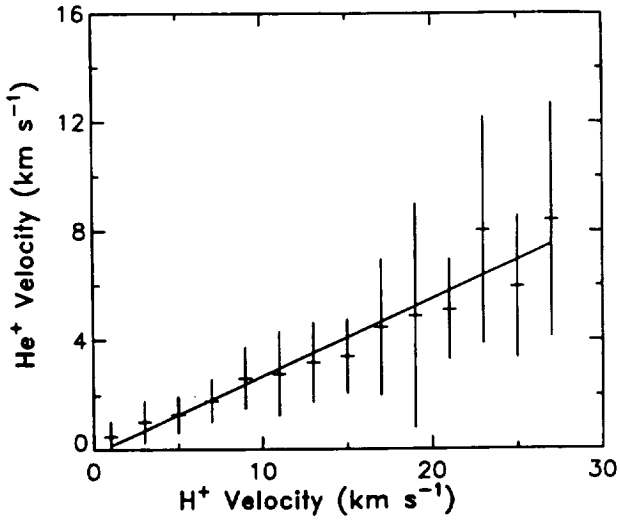

Fig. 6. The average velocity of He^+ as a function of the H^+ velocity.

to the $F_{10.7}$ variation. As for the seasonal variation (Figure 5) the difference between summer and winter is less than 20% (with the summer velocities lower than the winter velocities) which is much less than the standard deviations.

In the majority of the observations the O^+ outflow speed was less than 2 km s^{-1} so that experimental uncertainties make a comparatively larger contribution to the standard deviations. Thus the statistical significance is less than for H^+ or He^+.

Velocity correlations. Over the range of altitudes covered by this study, O^+ was the dominant ion. Therefore it is expected that both H^+ and He^+ would behave as minor ions. As the previous figures have shown there are similarities in the speed-vs-altitude profiles for the two minor species. To investigate the degree of correlation between the velocities for the two species, the H^+ speeds for altitudes between 2000 and 4000 km have been sorted into bins with 2 km s^{-1} widths and averages have been computed for the corresponding He^+ speeds. Figure 6 shows the results along with a linear fit to the data. The resulting parameters are given in the figure.

The results in Figure 7 show H^+ velocity vs. O^+ velocity for altitudes greater than 2000 km. While there is a systematic increase in the average H^+ speed with the change in O^+ velocity from −2 km s^{-1} (i.e., downward) to +2 km s^{-1} (upward) the effect is not striking. However, the range of observed H^+ speeds, as evidenced by the bars corresponding to the standard deviation about the mean value, also increases as the O^+ speed increases from −2 to 2 km s^{-1}. To more clearly illustrate this point, the maximum and minimum values of the H^+ velocity in each bin are shown. Note that while the minimum values are about the same for all values of the O^+ velocity, the maximum H^+ speed increases dramatically as the O^+ velocity increases. At altitudes above 2000 km it is expected that the plasma is collisionless. Thus the processes which are responsible for the correlations seen in Figure 7 must either be taking place lower in the ionosphere or are affecting the accelerating, ambipolar electric field.

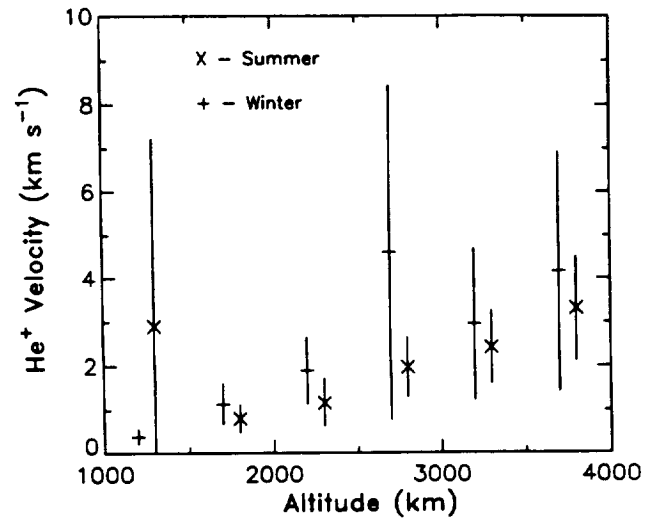

Fig. 5. The average velocity of He^+ as a function of altitude for the summer season and the winter season.

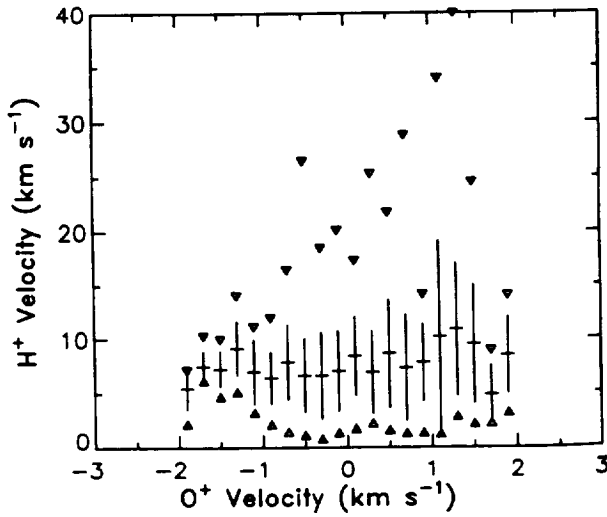

Fig. 7. The average velocity of H^+ as a function of the O^+ velocity for all data from altitudes greater than 2000 km. The inverted triangles above the averages are the maximum H^+ velocity values in each O^+ velocity bin. The triangles below the averages are the minimum H^+ velocity values in each O^+ velocity bin.

Velocity theory comparison. The average ion velocities discussed and shown above exhibit large statistical variations. It is important to understand whether these variations are indicative of experimental uncertainty or actual geophysical fluctuations. Figure 8 is a scatterplot of all the H^+ velocities used in this study as a function of altitude. Two points should be noted regarding these results. First, the values tend toward zero as the altitude decreases and the width of the spread in velocity increases with altitude. Theoretical results suggest this type of trend. For example, the results of *Raitt et al.* [1975] show the upward H^+ velocity increasing from a value near zero at ~800 km up to a maximum value, in the altitude range between 1000 and 2000 km, which depends on the boundary condition imposed at 3000 km. The solid curve in Figure 8 is their result for an upper boundary velocity of 20 km s^{-1}. This curve encompasses the RIMS results and follows closely the altitudinal profile suggesting that the fluctuations are mainly geophysical in nature.

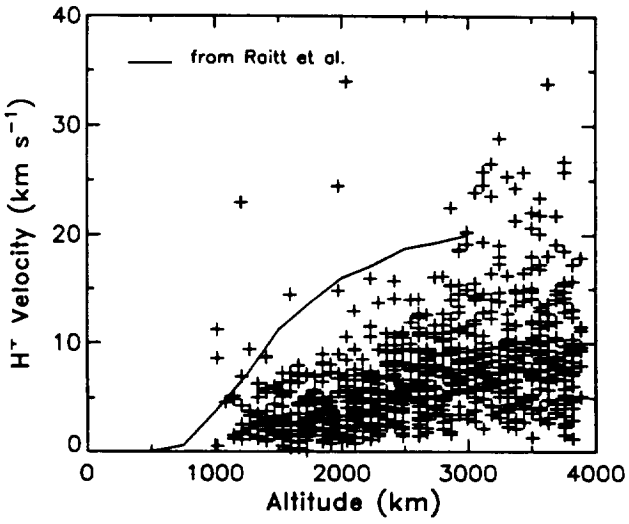

Fig. 8. Velocity of H^+ as a function of altitude for all data.

Average Density

The average density as a function of altitude (for altitude intervals of 500 km) is shown in Figure 9. In this altitude range O^+ is always the dominant ion being of the order of 10^3 cm^{-3}, while H^+ is ~100 cm^{-3} and He^+ is ~10 cm^{-3}. According to polar wind theory the major ion, O^+, will establish the polarization electric field and the minor ions, H^+ and He^+, should have the same altitude dependence as the dominant ion. This is indeed the case in the observations. When normalized to the O^+ density, the H^+ and He^+ densities at the higher three altitudes agree with each other and with the O^+ to within 10%. The ions have different altitude variations at lower altitudes because of differences in their ion chemistry.

As with the average velocities, the densities have been averaged for the cases of high and low $F_{10.7}$ flux and summer and winter season. In the case of O^+ (Figure 10) the density increased with increased $F_{10.7}$ flux at all altitudes. This increase (by approximately a factor of 2) is consistent with an increase in the solar EUV flux which is assumed to accompany a long-term increase in the $F_{10.7}$ flux. Conversely, there was no significant change in either the H^+ density (Figure 11) or the He^+ density (Figure 12). In the case of H^+, while the O^+ density increases from solar mini-

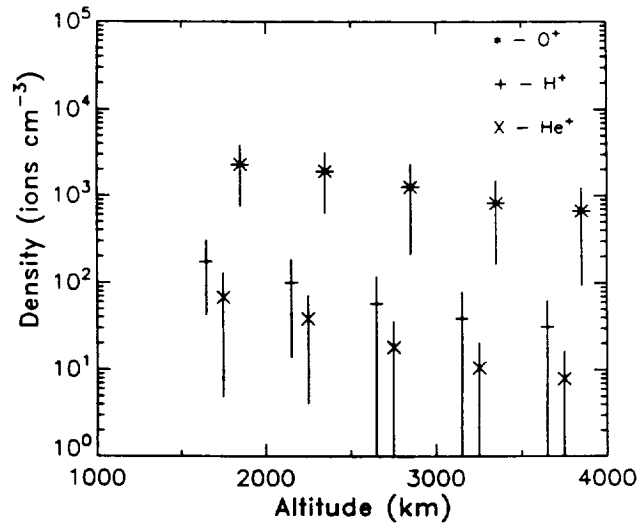

Fig. 9. The average density of each ion species as a function of altitude for all data samples.

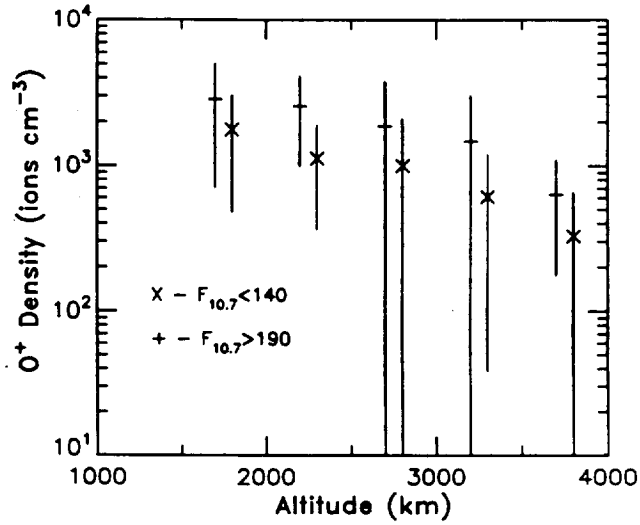

Fig. 10. The average density of O^+ as a function of altitude for $F_{10.7} < 140$ (10^{-22} W m^{-2} Hz^{-1}) and $F_{10.7} > 190$ (10^{-22} W m^{-2} Hz^{-1}).

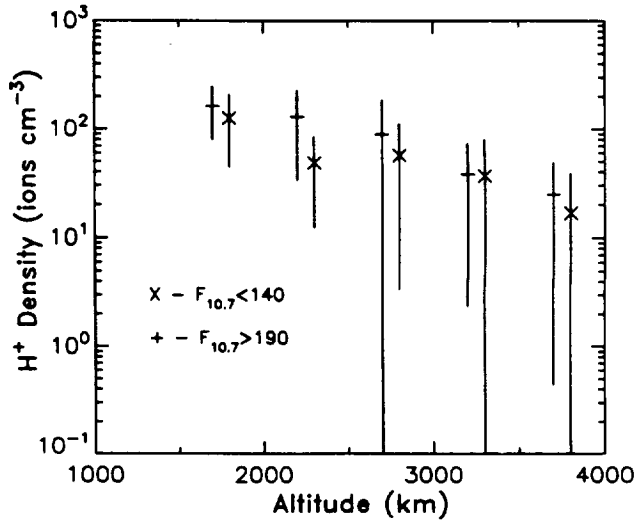

Fig. 11. The average density of H^+ as a function of altitude for $F_{10.7} < 140$ (10^{-22} W m^{-2} Hz^{-1}) and $F_{10.7} > 190$ (10^{-22} W m^{-2} Hz^{-1}).

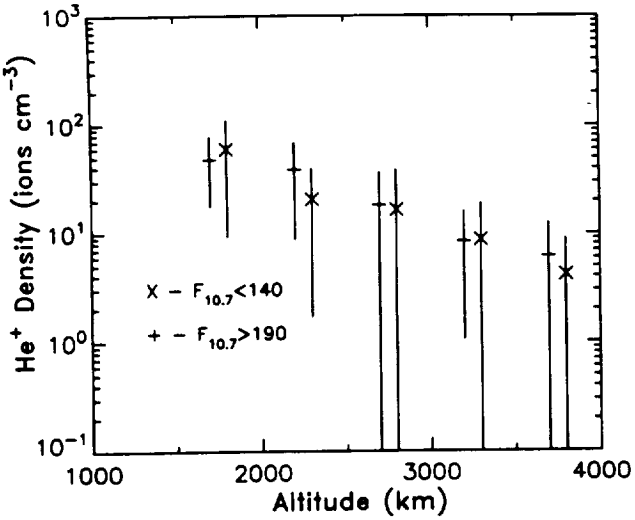

Fig. 12. The average density of He^+ as a function of altitude for $F_{10.7}$ < 140 (10^{-22} W m^{-2} Hz^{-1}) and $F_{10.7}$ > 190 (10^{-22} W m^{-2} Hz^{-1}).

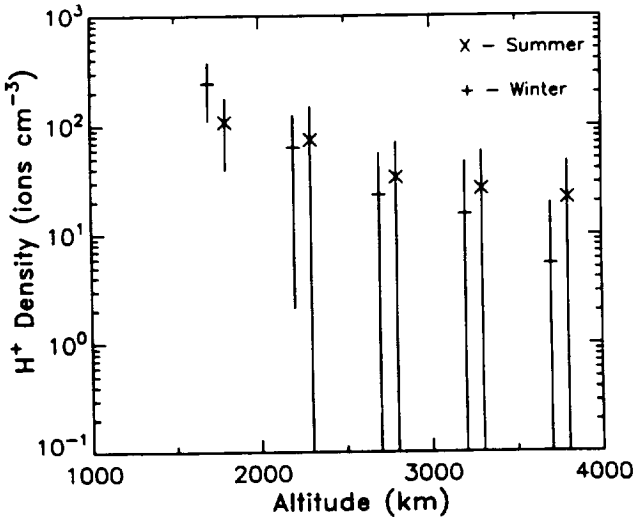

Fig. 14. The average density of H^+ as a function of altitude for the summer season and the winter season.

mum to solar maximum conditions, the [H] decreases and the results is little variation in H^+ density. Likewise, *Raitt et al.* [1978*b*] found no significant solar cycle effect in the He^+ density.

The seasonal variations are shown in Figures 13, 14, and 15. The O^+ observations revealed a decrease in overall density from summer to winter of about a factor of 3. The winter density at the highest altitudes observed dropped to <200 cm^{-3} which had significant impact on the ability of RIMS to accurately measure the H^+ density. This is evidenced in Figure 14 which shows a large difference in the observed H^+ density near 4000 km. In this altitude bin the summer density is a factor of 4 higher than the winter value. Conversely, at altitudes near 2000 km the densities were either nearly equal or higher in the winter. A positive electrical potential on the spacecraft resulting from the relatively low electron density at 4000 km in the winter has screened out a portion of the H^+. Thus these observations represent a lower limit for the actual values. Note that at the lowest altitudes the winter H^+ density is higher than the summer value. This is consistent with a

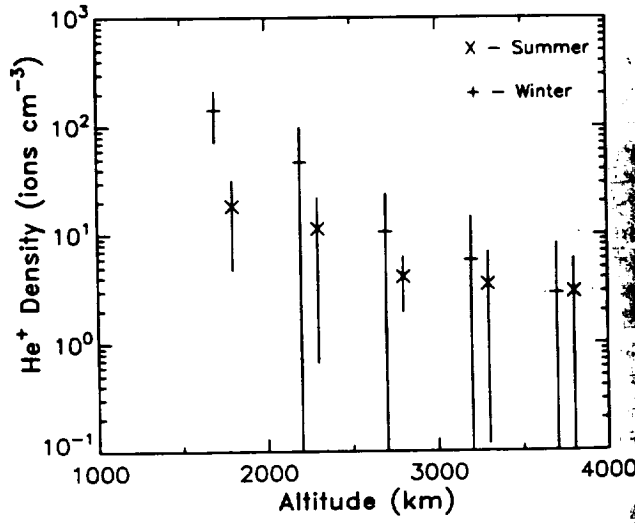

Fig. 15. The average density of He^+ as a function of altitude for the summer season and the winter season.

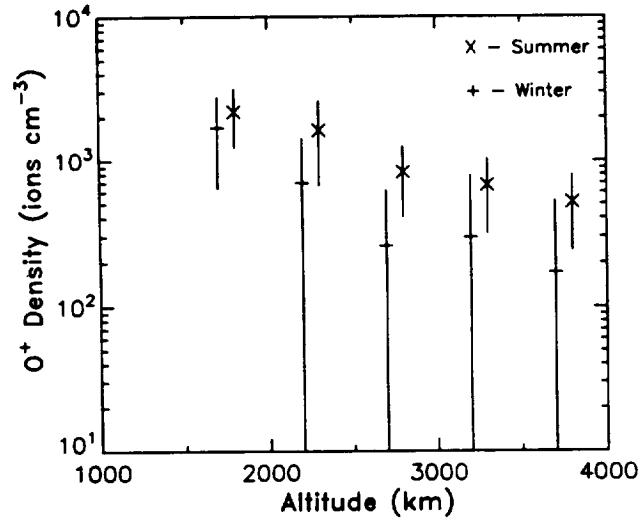

Fig. 13. The average density of O^+ as a function of altitude for the summer season and the winter season.

winter enhancement in the neutral hydrogen density. Similarly for He^+, at the lowest altitudes the winter density is significantly higher than the summer density, indicative of the winter neutral helium bulge. But, as with the H^+, the observed He^+ winter density at higher altitudes falls to the level of the summer observations due to the positive potential.

SUMMARY

The classical polar wind picture is one of steady outflow of light ions through a stationary background of O^+. Results of this study show that when the real outflows are averaged over periods of months such steady pictures do emerge. On the other hand, the lack of correlation between various geophysical parameters, which vary over different time scales ranging from hours to months, suggests that much of the variability in the polar cap outflows is a result of short time scale (<hours) phenomena. Nevertheless, there do exist some interesting aspects of these long-time averages. Seasonal variations in the light ion outflows follow the

trend expected from known variations in the neutral atmosphere Namely, the flux of He^+ increased by a factor of 10 from summer to winter. As evidenced in the observations of the density and velocity this increase was primarily due to increased density in winter, a direct result of the winter [He] enhancement. The neutral hydrogen density is likewise known to maximize during winter. However, the H^+ flux had a maximum value in the spring. This is probably the result of the interplay between the seasonal variation of [H] and that of O^+ which exhibits a summer maximum. Combining these two cycles can yield a spring maximum for the product of [H] and n_{o^+}.

Correlations with geophysical parameters revealed some variations though most were small. Variations in the flux with changes in the solar $F_{10.7}$ cm flux were less than a factor of 3 for H^+. However, changes in the velocity were evident at middle altitudes (i.e., 2000–3000 km) where the light ions were observed to undergo the largest net acceleration. The solar output, as characterized by the $F_{10.7}$ value, influenced the altitude at which this acceleration began, the altitude being ~500 km higher at high $F_{10.7}$ compared to low $F_{10.7}$. This effect is a result of the higher neutral temperatures in the exosphere due to the increased solar output. These higher temperatures increase [O] and decrease [H] [cf. *Richards and Torr*, 1985]. The increased [O] and higher photoionization rate result in more O^+ as observed (see Figure 10). As a result H^+–O^+ friction, which restricts the H^+ upward speed, becomes important at higher altitudes.

Conversely the maximum speed for the light ions is observed to be more sensitive to the season than the $F_{10.7}$ flux. The season, or more importantly, the solar zenith angle, is important in determining the ionization rate and hence the photoelectron escape rate and the magnitude of the polarization electric field. Higher ion and electron temperatures during summer may also play a role depending on whether or not the H^+ flow is supersonic.

The ion outflow velocities revealed the influence of solar input as discussed previously. There was also observed a high degree of correlation between the velocities of the different ions. As expected the light ions were well correlated in the magnitude of their upward speed. The ratio of the He^+ velocity to that of H^+ was 0.28 (with a correlation coefficient of 0.71). If both ions were energized in the ambipolar field under conditions of zero collisions and no gravity, this ratio should be 0.5. However, because of the mass dependence of the energy loss to gravity the net energy gain for He^+ is less and the ratio is lower.

The upward speed of H^+ was also observed to be correlated with the direction of O^+ flow. While the average H^+ velocity did not show substantial variation with O^+ velocity, the range of H^+ velocities increased as the O^+ velocity changed from downward to upward. That is, higher upward H^+ speeds occurred at times when O^+ was also moving upward. These relationships are indicative of the interplay, by means of the polarization field and collisions, among the ions which participate in the polar wind flow. For example, downgoing O^+ may occur in regions where there exists a time-dependent decrease in the electron and/or ion temperature of sufficient magnitude to affect the polarization field. Thus while the partial pressure of H^+ in the ionosphere might be sufficient to cause outflow the reduced ambipolar field would restrict the magnitude of that outflow. Such a case has been modeled by *Schunk and Sojka* [1989] where they found O^+/H^+ counterstreaming in regions of decreasing temperature.

The question of subsonic versus supersonic flow is beyond the scope of the current work, depending on a thermal analysis of the outflows. Some inferences can be made, however, by comparing the observations of the H^+ velocity as a function of altitude to theoretical results [e.g., *Banks and Holzer*, 1968]. Solutions to the equations for the H^+ Mach number show profiles, corresponding to subsonic solutions, which reach a maximum at some altitude and either decrease or remain constant above that altitude. If the results in Figure 3 are taken as representative of such a situation then the implication is that on average the maximum flow speed during winter was less than the sound speed. The conclusion may then be drawn that at times during the period of the observations the plasma pressure remained finite along these polar cap field lines. Indeed, several of the velocity profiles from individual orbital passes through the polar cap show a similar structure. Attempts to correlate this effect with geophysical and solar parameters have, to this point, been unsuccessful. To date, no theoretical work has addressed this issue through systematic investigation of outflow characteristics as a function of the pressure at the "far" end of the flux tube.

There remains much to learn regarding the nature of the polar wind. The question of the polar wind Mach number is left unanswered by this study due to the lack of knowledge of the ion temperature. Techniques for the determination of ion temperature from all available RIMS polar ionosphere observations are being developed. However, the implication of a subsonic polar wind (e.g., nonzero "backpressure" along polar cap field lines) should provide impetus for a detailed parametric study of the character of the polar wind velocity under such conditions using the currently available theoretical models. Future observations should shed more light on this topic. Likewise, observations made on shorter timescales will aid investigators in addressing the influences of rapidly varying geophysical parameters. Such measurements will be available from instruments such as TIDE on the ISTP/POLAR mission.

Acknowledgments. The authors are indebted to Rita Reynolds for her efforts during the processing and analysis of the data included in this study. The authors wish to thank C. R. Chappell for discussions related to this research and critique of this manuscript. We are grateful to the staff of Boeing Computer Services for programming support and to the engineering and science staff at The University of Texas at Dallas and to the RIMS team at MSFC. This research was supported by the Dynamics Explorer Program at Goddard Space Flight Center. The research at Southwest Research Institute was supported by SwRI Internal Research project #15-9557 and NASA Space Physics grant NAGW-1657. The authors acknowledge the constructive comments of the referees and thank them for their efforts.

The Editor thanks R. C. Olsen and A. W. Yau for their assistance in evaluating this paper.

REFERENCES

Axford, W. I., The polar wind and the terrestrial helium budget, *J. Geophys. Res.*, *73*, 6855, 1968.

Bailey, G. J., and R. J. Moffett, Temperatures in the polar wind, *Planet. Space Sci.*, *22*, 1193, 1974.

Banks, P. M., Ion heating in thermal plasma flows, *J. Geophys. Res.*, *78*, 3186, 1973.

Banks, P. M., and T. E. Holzer, The polar wind, *J. Geophys. Res.*, *73*, 6846, 1968.

Banks, P. M., and T. E. Holzer, Features of plasma transport in the upper atmosphere, *J. Geophys. Res.*, *74*, 6304, 1969*a*.

Banks, P. M., and T. E. Holzer, High latitude plasma transport: The polar wind, *J. Geophys Res.*, *74*, 6317, 1969*b*.

Banks, P. M., A. F. Nagy, and W. I. Axford, Dynamical behavior of thermal protons in the mid-latitude ionosphere and magnetosphere, *Planet. Space Sci.*, *19*, 1053, 1971.

Banks, P. M., R. W. Schunk, and W. J. Raitt, Temperature and density structure of thermal proton flows, *J. Geophys. Res.*, *79*, 4691, 1974.

Banks, P. M., R. W. Schunk, and W. J. Raitt, The topside ionosphere: A region of dynamic transition, *Ann. Rev. Earth Planet. Sci.*, *4*, 381, 1976.

Barakat, A. R., R. W. Schunk, T. E. Moore, and J. H. Waite, Jr., Ion escape fluxes from the terrestrial high-latitude ionosphere, *J. Geophys. Res.*, *92*, 12,255, 1987.

Biddle, A. P., T. E. Moore, and C. R. Chappell, Evidence for ion heat flux in the light ion polar wind, *J. Geophys. Res.*, *90*, 8552, 1985.

Chandler, M. O., and C. R. Chappell, Observations of the flow of H^+ and He^+ along magnetic field lines in the plasmasphere, *J. Geophys. Res.*, *91*, 8847, 1986.

Chappell, C. R., S. A. Fields, C. R. Baugher, J. H. Hoffman, W. B. Hanson, W. W. Wright, H. D. Hammack, C. R. Carignan, and A. F. Nagy, The retarding ion mass spectrometer on Dynamics Explorer-A, *Space Sci. Instrum.*, *5*, 477, 1981.

Dessler, A. J., and P. A. Cloutier, Discussion of the letter of Peter M. Banks and Thomas E. Holzer, The polar wind, *J. Geophys. Res.*, *74*, 3730, 1969.

Dessler, A. J., and F. C. Michel, Plasma in the geomagnetic tail, *J. Geophys. Res.*, *71*, 1421, 1966.

Dungey, J. W., Interplanetary magnetic and the auroral zones, *Phys. Rev. Lett.*, *6*, 47, 1961.

Gombosi, T. I., T. E. Cravens, and A. F. Nagy, A time-dependent model of the polar wind: Preliminary results, *Geophys. Res. Lett.*, *12*, 167, 1985.

Gurgiolo, C., and J. L. Burch, DE-1 observations of the polar wind – A heated and an unheated component, *Geophys. Res. Lett.*, *9*, 945, 1982.

Hoffman, J. H., Studies of the composition of the ionosphere with a magnetic deflection mass spectrometer, *Int. J. Mass Spectrom. Ion Physics*, *4*, 315, 1970.

Hoffman, J. H., and W. H. Dodson, Light ion concentrations and fluxes in the polar regions during magnetically quiet times, *J. Geophys. Res.*, *85*, 626, 1980.

Hoffman, J. H., W. H. Dodson, C. R. Lippincott, and H. D. Hammack, Initial ion composition results from the Isis 2 satellite, *J. Geophys. Res.*, *79*, 4246, 1974.

Holzer, T. E., J. A. Fedder, and P. M. Banks, A comparison of kinetic and hydrodynamic models of an expanding ion-exosphere, *J. Geophys. Res.*, *76*, 2453, 1971.

Lemaire, J., O^+, H^+, and He ion distributions in a new polar wind model, *J. Atmos. Terr. Phys.*, *34*, 1647, 1972.

Lemaire, J., and M. Scherer, Model of the polar ion-exosphere, *Planet. Space Sci.*, *18*, 103, 1970.

Lemaire, J., and M. Scherer, Simple model for an ion-exosphere in an open magnetic field, *Phys. Fluids*, *14*, 1683, 1971.

Lemaire, J., and M. Scherer, Ion-exosphere with asymmetric velocity distribution, *Phys. Fluids*, *15*, 760, 1972.

Marubashi, K., Escape of the polar-ionosphere plasma into the magnetospheric tail, *Rep. Ionos. Space Res., Jpn.*, *24*, 322, 1970.

Nagai, T., J. H. Waite, J. L. Green, C. R. Chappell, R. C. Olsen, and R. H. Comfort, First measurements of supersonic polar wind in the polar magnetosphere, *Geophys. Res. Lett.*, *11*, 669, 1984.

Nishida, A., Formation of a plasmapause or magnetospheric plasma knee by combined action of magnetospheric convection and plasma escape from the tail, *J. Geophys. Res.*, *71*, 5669, 1966.

Olsen, R. C., Charging characteristics of Dynamics Explorer I Ion Mass Spectrometer and consequences of core plasma measurements, *Tech. Rep. NPS-61-89-014*, Nav. Postgrad. Sch., Monterey, Calif., Sept. 1989.

Ottley, J. A., and R. W. Schunk, Density and temperature structure of helium ions in the topside polar ionosphere for subsonic outflows, *J. Geophys. Res.*, *85*, 4177, 1980.

Parker, L. W., and E. C. Whipple, Jr., Theory of spacecraft sheath structure, potential, and velocity effects on ion measurements by traps and mass spectrometers, *J. Geophys. Res.*, *75*, 4720, 1970.

Raitt, W. J., and R. W. Schunk, Composition and characteristics of the polar wind, in *Energetic Ion Composition in the Earth's Magnetosphere*, edited by R. J. Johnson, p. 99, Terra Scientific, Tokyo, 1983.

Raitt, W. J., R. W. Schunk, and P. M. Banks, A comparison of the temperature and density structure in high and low speed thermal proton flows, *Planet. Space Sci.*, *23*, 1103, 1975.

Raitt, W. J., R. W. Schunk, and P. M. Banks, The influence of convection electric fields on the thermal proton outflow from the ionosphere, *Planet. Space Sci.*, *25*, 291, 1977.

Raitt, W. J., R. W. Schunk, and P. M. Banks, Helium ion outflow from the terrestrial ionosphere, *Planet. Space Sci.*, *26*, 255, 1978*a*.

Raitt, W. J., R. W. Schunk, and P. M. Banks, Quantitative calculations of helium ion escape fluxes from the polar ionosphere, *J. Geophys. Res.*, *83*, 5617, 1978*b*.

Richards, P. G., and D. G. Torr, Seasonal, diurnal, and solar cycle variations of the limiting H^+ flux in the Earth's topside ionsophere, *J. Geophys. Res.*, *90*, 5261, 1985.

Schunk, R. W., and J. J. Sojka, A three-dimensional model of the polar wind, *J. Geophys. Res.*, *94*, 8973, 1989.

Schunk, R. W., and D. S. Watkins, Comparison of solutions to the thirteen-moment and standard transport equations for low speed thermal proton flows, *Planet. Space Sci.*, *27*, 433, 1979.

Schunk, R. W., and D. S. Watkins, Electron temperature anisotropy in the polar wind, *J. Geophys. Res.*, *86*, 91, 1981.

Schunk, R. W., and D. S. Watkins, Proton temperature anisotropy in the polar wind, *J. Geophys. Res.*, *87*, 171, 1982.

Schunk, R. W., W. J. Raitt, and A. F. Nagy, Effect of diffusion-thermal processes on the high-latitude topside ionosphere, *Planet. Space Sci.*, *26*, 189, 1978.

Sojka, J. J., R. W. Schunk, J. F. E. Johnson, J. H. Waite, and C. R. Chappell, Characteristics of thermal and suprathermal ions associated with the dayside plasma trough as measured by the Dynamics Explorer retarding ion mass spectrometer, *J. Geophys. Res.*, *88*, 7895, 1983.

Strobel, D. F., and E. J. Weber, Mathematical model of the polar wind, *J. Geophys. Res.*, *77*, 6864, 1972.

Yau, A. W., P. H. Beckwith, W. K. Peterson, and E. G. Shelley, Long-term (solar cycle) and seasonal variations of upflowing ionospheric ion events at DE-1 altitudes, *J. Geophys. Res.*, *90*, 6395, 1985*a*.

Yau, A. W., E. G. Shelley, W. K. Peterson, and L. Lenchyshyn, Energetic auroral and polar ion outflow at DE-1 altitudes: Magnitude, composition, magnetic activity dependence, and long-term variations, *J. Geophys. Res.*, *90*, 8417, 1985*b*.

M. O. Chandler and T. E. Moore, Space Science Laboratory, NASA George C. Marshall Space Flight Center, Huntsville, AL 35812.

J. H. Waite, Jr., Department of Space Sciences, Southwest Research Institute, San Antonio, TX 78288.

(Received December 20, 1989;
revised September 28, 1990;
accepted September 28, 1990.)

Update on polar wind thermal characterization scheme

The application of thermal analysis techniques to the DE 1/RIMS polar wind dataset is an interesting challenge. While the RIMS design was a significant improvement to previous Retarding Potential Analyzer (RPA) instruments, its mass-resolving capabilities introduced additional complexities in the form of an energy-dependent solid angle aperture and a finite energy bandwidth beyond the RPA setting. In addition, in-flight anomalies produced significant difficulties in comparison to the analysis of conventional RPA datasets. Particularly relevant to the RIMS polar wind dataset is that the radial head RPA mechanism failed to operate properly early in the mission lifetime.

Fortunately though, by adopting a numerical quadrature approach to the solution of the response integral, using sums over the aperture area, solid angle, and energy limits, energy-dependent complications may be sufficiently simulated. And, because separate spin and RPA profiles are available for each of the three instrument heads, the radial head spin curve and the end head RPA curves are usable for temperature analysis even in the absence of the radial head RPA information. Since the effect of the radial RPA failure is as if the retarding voltage was constantly zero, the total counts measurement remains accurate. Numerical algorithms of this type tend to be computationally intensive, but have the advantage of being applicable to a variety of plasma distribution functions.

In the case of the polar wind dataset, further considerations on the data analysis technique are necessary. Strictly speaking, spacecraft spin angle distributions observed in situ are not true pitch angle distributions. The measured spin angle is defined in the reference frame of the spacecraft, which is different from the plasma rest frame due to spacecraft motion (2 to 8 kilometers per second, depending on spacecraft altitude). This difference in reference frame would be of little consequence provided the thermal speed of the plasma is large compared to the spacecraft "ram" speed. For a spacecraft median speed of 5 km/s, a factor-of-five ratio of thermal speed to spacecraft speed implies 3.5 eV for H^+, 13 eV for He^+ and 52 eV for O^+. Because polar wind energies are considerably below this

threshold, the RIMS spin angle data contain information about both the angular distribution of the plasma in its own frame of reference (the conventional pitch angle distribution) and the drift motion of the plasma relative to the spacecraft. These two aspects of instrument response tend to dominate independently – one at times obscuring the other – depending on the plasma's thermal speed and its relation to the spacecraft and plasma drift speed.

Roughly speaking, it is for subsonic (thermal speed greater than drift speed) ion Mach numbers that the angular characteristics of the distribution are best resolved and for supersonic Mach numbers that drift motion is most easily resolvable. Note that in the case of H+, flow will be subsonic for thermal components as low as 1 eV when drift velocities are less than 15 km/s. The bottom line, for RIMS polar wind data, is that the relative drift motion will dominate the spin angle response, leading to a "rammed" flux peak in the direction of relative wind as seen in the spacecraft frame. The angular (and hence, temperature) information will be apparent only in the detailed shape of the rammed peak and may, at times, become indeterminate. The end-head RPA profiles then, become increasingly important to the accurate determination of our polar wind thermal properties.

With all these cautions in mind, a numerical simulation model of the RIMS response to a flowing plasma distribution was written [*Giles et al.*, 1993]. The simulation technique improves on previous work by realistically modeling the interaction of a moving spacecraft with a drifting plasma and by allowing insertion of a variety of distribution functions (for example, bi-Maxwellian, generalized Lorentz (Kappa), and *Spitzer-Härm* [1953]), the three-component drift velocity, and a variable spacecraft potential. For the polar wind study, the distribution function is assumed to be a flowing bi-Maxwellian which is accelerated through the potential difference between the spacecraft and the plasma. The potential drop is assumed to occur in an infinitesimally thin sheath about the spacecraft and the detector, rendering the detail of sheath structure unimportant. The implementation allows simultaneous fitting of the radial sector spin curve data and the end sector RPA (energy) curves.

Figure 1 shows simulated RIMS spin-angle and RPA responses to a bi-Maxwellian plasma distribution (solid lines) and the RIMS polar wind data (crosses) for 1982/106 22:17 UT. Note that the instrument response, for a given detector look direction, is to ions with velocities *anti-parallel to the detector look direction*. Plasma distribution parameters for this fit are:

density	224 cm^{-3}
$T_{\|}$	0.36 eV
$T_{\perp}$	0.28 eV
field-aligned velocity	4.14 km/s
anti-sunward convection velocity	2 km/s

Note that these parameters correspond to a cold subsonic outward flow (ion Mach number ~0.49). Early predictions indicated that the H^+ polar wind thermal distributions should be anisotropic, with $T_{\|}>T_{\perp}$ for supersonic outflows and $T_{\|}<T_{\perp}$ for subsonic flows. The present example however, fits in with work by *Wu and Taieb* [1993] showing that an upward heat flux may exist even for subsonic flow at low altitude in the high-latitude ionosphere.

Processing of the RIMS polar wind dataset using the RIMS simulation code continues as of April, 1995. Several studies have been completed which relieve difficulties associated with fitting multivariate functions. Frequently it is a matter of art to decide which variables in a model should be fit from the dataset, and which should be held constant at fixed values, for example values predicted by theory or derived in previous analysis. In the case of the polar wind data set, variables potentially free for fitting to the data are the spacecraft potential, plasma density, the two-component plasma temperature, and the three-component plasma bulk flow velocity. In the present implementation, the ion field-aligned velocity component and flux measurements (and so, the density value) are held fixed. Their values were obtained [*Chandler et al.*, 1991] by integrating the observed flux over the spin cycle of the satellite for a zero RPA voltage. Also, the spacecraft potential value is held fixed during the first stage of the fitting process, an initial value being derived from an empirical relationship between the plasma density and spacecraft

potential [*Comfort et al.*, 1988]. Values fit from the data set then are the two-component temperature and the remaining two components of the bulk flow velocity. The perpendicular temperature is fit by chi-square minimization to the end-head RPA profiles. The parallel temperature is similarly fit to the radial head spin angle profile. The orientation of the spacecraft for the polar wind data set is such that the expected anti-sunward convection velocity is almost completely described by the y component of the bulk flow velocity vector. This is fit first by minimization to the radial head spin angle profile and then refined through minimization to the end-head profiles. Last, the spacecraft potential value is fit in the same order, to the same three profiles. The fit in figure 1 was obtained by this method.

Chandler, M. O., J. H. Waite, Jr., and T. E. Moore, Observations of polar ion outflows, *J. Geophys. Res.*, *96*, 1421-1428, 1991.

Comfort, R. H., P. D. Craven, D. L. Gallagher, R. L. West, and C. R. Chappell, Spacecraft potential dependence on plasma density from GEOS-2 and DE-1 measurements, Spring AGU Meeting, Baltimore, MD, May 16-20, 1988; abstract: *Eos. 69(16)*, 448 1988.

Giles, B. L., Inner magnetosphere circulation of thermal ions inferred from observed pitch angle distributions, Ph.D. thesis, University of Alabama in Huntsville. 1993.

Spitzer, L., and R. Härm. Transport phenomena in a completely ionized gas, *Phys Rev.* *89*, 977, 1953.

Wu, J., and C. Taieb, Heat flux solutions of the 13-moment approximation transport equations in a multispecies gas, *J. Geophys. Res.*, *98*, 15,613-15,619, 1993.

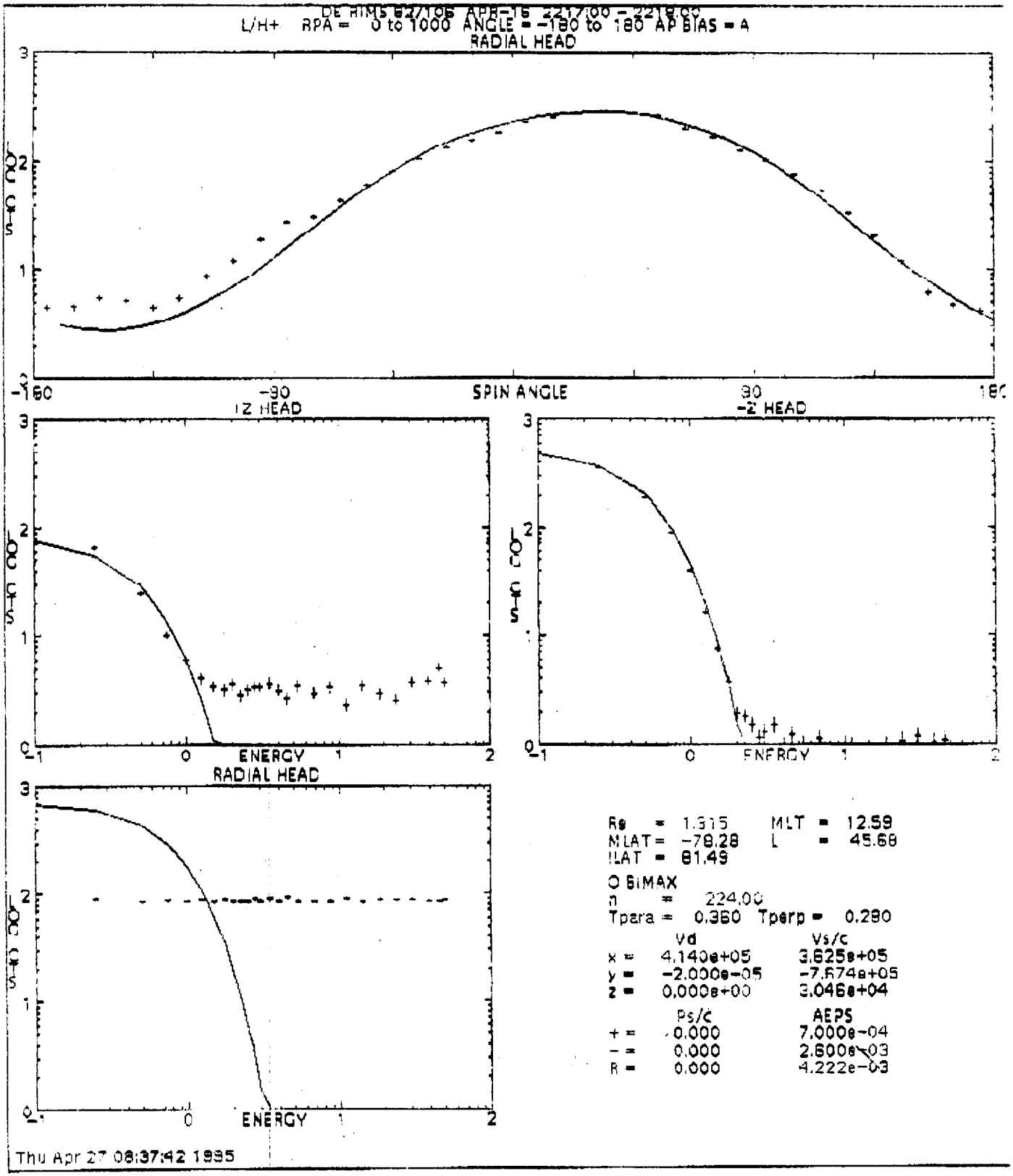
DE HIMS 82/106 APR-16 2217:00 - 2218:00
L/H+ RPA = 0 to 1000 ANGLE = -180 to 180 AP BIAS = A
RADIAL HEAD
SPIN ANGLE
+Z HEAD
-Z HEAD
ENERGY
RADIAL HEAD
ENERGY
Rs = 1.315 MLT = 12.59
MLAT = -78.28 L = 45.68
ILAT = 81.49
O BiMAX
n = 224.00
Tpara = 0.360 Tperp = 0.280
Vd Vs/c
x = 4.140e+05 3.625e+05
y = -2.000e-05 -7.674e+05
z = 0.000e+00 3.046e+04
Ps/c AEPS
+ = 0.000 7.000e-04
- = 0.000 2.600e-03
R = 0.000 4.222e-03
Thu Apr 27 08:37:42 1995